Ultrahigh-Q Microtoroid On-Chip Resonators for Low Threshold Microlasers

Thesis by

Bumki Min

In Partial Fulfillment of the Requirements

for the Degree of

Doctor of Philosophy

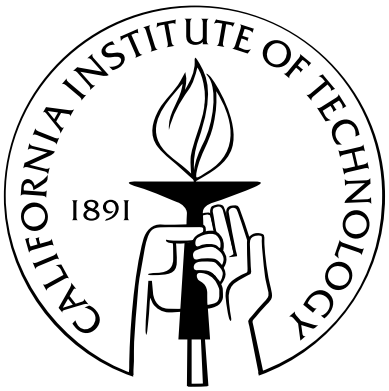

California Institute of Technology

Pasadena, California

2006

(Defended May 26, 2006)

To my parents and my wife

Acknowledgements

I would first like to express my sincere gratitude to my advisor, Prof. Kerry Vahala, for giving me a wonderful research opportunity and supporting me throughout my work at Caltech. He was a true architect of my research during the last five years: sometimes as a great academic adviser, and sometimes even as a mentor when I was in trouble. His insightful suggestions and zealous guidance always kept me from falling and his higher and noble goals in research encouraged me to achieve beyond my ability.

I am deeply indebted to my former advisor, Prof. Namkyoo Park, for supporting and encouraging me to find and pursue the right path since my undergraduate years at Seoul National University. He was the one who first infused a passion for research: he taught and trained me from the very beginning. I cannot thank him enough for his devotion and for guiding me so far.

I was truly fortunate to collaborate with wonderful coworkers who profoundly influenced and contributed to my work at Caltech. Prof. Sungjee Kim introduced me to the topic of nanocrystal quantum dots. His wide range of knowledge and enthusiastic attitude stimulated me to go a step further. Many thanks to Dr. Koichi Okamoto who gave me a generous and kind collaboration: it was unbelievably helpful and pleasant to work with him. Dr. Young-Bae Park encouraged me to do research in a new field and helped me with appropriate solutions when I encountered material-related problems. I also thank him for his sincere and warm praise for even very small achievements. It was my great pleasure to work with Prof. Albert Polman and Dr. Jeroen Kalkman.

This journey would have been less delightful and fruitful without my former and present lab members: Dr. Lan Yang, Dr. Deniz Armani, Andrea Martin, Dr. Tobias Kippenberg, Dr. Sean Spillane, Sameer Walavalkar, Dr. Hossein Rokhsari, Dr. Tal Carmon, and Dr. Mani Hossein-Zadeh. Especially, Dr. Lan Yang was the first one who greeted me upon my

arrival to Caltech. I thank her for every kindness she has shown me and discussions we shared from the bottom of my heart. Dr. Deniz Armani taught me device fabrication and gave me lots of laughs: even arduous experiments became enjoyable with him. I respect Andrea Martin's hard work, discipline, and endlessly energetic efforts. A special thanks to Dr. Tobias Kippenberg and Dr. Sean Spillane who had set up all the basic stuff for the lab. It was my honor to have the world's most eminent scholars as my thesis and candidacy committee members: Prof. Harry Atwater, Prof. Oskar Painter, Prof. Bruno Crosignani, Prof. Axel Scherer, and Prof. Changhuei Yang. I especially thank Prof. Harry Atwater for his concern and support on my research with invaluable advice.

Also, I owe many thanks to my precious friends whom I met at Caltech for their sincere friendship and support, especially Prof. Donhee Ham and Dr. Junryul Huh. I thank Prof. Donhee Ham very much for our endless and enthusiastic discussions on long distant calls: he extended my knowledge beyond my topic. Dr. Junryul Huh was one of the first men I met at Caltech and he touched me with his enormously favorable manner since then.

Last but not least, I give my deepest gratitude to my parents and my wife. My mother, Insuk Lee, and father, Changhwan Min, have all been so supportive throughout my entire life. My wife, Munjung, has been always on my side over the last five years. They provided the most encouragement and endless devotion, and this thesis is dedicated to them with my deepest gratitude and respect because without their love and support, this would not have been possible.

Abstract

Recently demonstrated silica toroidal microcavities, as on-chip resonant cavities, become one of the most promising laser resonators due to their exceptional ability to confine optical energy temporarily and spatially (high Q-factor and small mode volume) while being integrated on a silicon substrate. In the first part of this thesis, semianalytic theory is presented for an in-depth understanding of the high-Q toroidal microcavity coupled to a tapered fiber waveguide. Basic properties of toroidal microcavities such as cavity mode field, resonance wavelength, cavity mode volume, radiative Q-factor, and phase-matching condition are described within the limit of an iterative perturbation expansion method. With this theoretical background, various laser systems with different gain media, utilizing the high-Q toroidal microcavity as a laser resonator, are demonstrated in the latter parts.

As a first example, II-VI semiconductor nanocrystal, CdSe/ZnS (core/shell), quantum dots are coated on the surface of ultrahigh-Q toroidal microcavities. By pulsed excitation of quantum dots on the surface, either through tapered fiber waveguides or free-space, lasing is observed at both room and liquid nitrogen temperature. Use of a tapered fiber coupling substantially lowered the threshold energy when compared to the case of free-space excitation. Further threshold reduction down to 9.9 fJ was made possible by quantum dot density control.

Lasing from an erbium-implanted high-Q silica toroidal microcavity is demonstrated and analyzed in the next chapter. A minimum threshold power as low as 4.5 μW and a maximum output lasing power as high as 39.4 μW are obtained. Control of lasing wavelength is demonstrated by changing the cavity loading. Analytic formulas predicting threshold power, differential slope efficiency are derived and their dependence on cavity loading, erbium ion concentration and Q-factor is found and compared with the experimental results.

The nonlinear oscillation in an ultrahigh-Q silica toroidal microcavity is investigated in

the last chapter. A controllable and reversible transition between parametric and Raman oscillation is experimentally demonstrated and theoretically analyzed. By direct change of cavity loading and indirect adjustment of frequency detuning, parametric and/or Raman oscillation can be accessed selectively without modification of cavity geometry in a toroidal microcavity with large enough aspect ratio. Based on an effective cavity gain theory, this transition is analyzed in terms of cavity loading and frequency detuning leading to a better understanding of the combined effects of parametric and Raman processes in silica microcavities.

Contents

List of Figures

Chapter 1

Introduction

1.1 Surface-tension-induced optical microcavities

Whispering-gallery modes (WGMs) in surface-tension-induced optical microcavities have distinct features when compared to the confined modes of a Fabry-Pérot or a distributed feedback resonator. In a surface-tension-induced microcavity, the light is consistently bounced back from a dielectric curved cavity boundary by (almost) total internal reflection. Consequent resonance conditions are then achieved by the round-trip phase shift matching of the whispering-gallery mode. The surface-tension-induced microcavity structures (especially made from silica) have attracted considerable attentions due to their inherent low intrinsic loss that can be partly attributed to near-atomic smoothness of the surface quality as well as low material loss window of silica.[1] Furthermore, the ease of fabrication at lower costs makes it a strong candidate for scientific researches and engineering applications.

The concept of the WGM originated in the curved gallery surfaces of the St Paul's Cathedral in London and was first theorized in the form of an acoustical wave by Rayleigh [3, 4]. After the founding works of Mie and Debye [1, 5, 6], Richtmyer proposed the use of an axially-symmetric (spherical and toroidal) dielectric cavity as a high-Q electromagnetic resonator in 1939 [7]. Actual observation of the WGMs in these surface-tension-induced *micron-sized* cavities in the optical frequency domain dated back to the series of researches on the liquid droplets that are formed naturally in a near-spherical shape by the surface tension [8, 9]. However, micro-droplets were inherently transient and the free-space exci-

[1] From UV to $\sim$1.5 μm, the loss of fused silica is mainly limited by Rayleigh scattering induced by density fluctuations while from $\sim$1.5 μm to longer wavelengths, it is dominated by lattice absorption [1]. Still in the telecommunication band, other loss mechanisms such as adsorption/chemoposition of OH^- or water can limit the quality factor significantly [2].

tation of resonances was inefficient due to the nature of the coupling. After a decade of research on the transient liquid droplets, a solid-state version of the spherically shaped cavity was first made by melting the tip of a fiber to create a silica microsphere resonator [10]. These solid-phase microspheres, like their liquid counterparts, rely upon surface tension to create an exquisitely smooth dielectric boundary [2] in which the whispering-gallery modes are confined. Cavity quality factors (Q-factors) as high as 8×10^9 have been demonstrated along with relatively small mode volumes.[2] These quality factors have been the essential driving force in fundamental research areas such as cavity quantum electrodynamics [12–14], nonlinear optics [15–17], biosensing [18, 19], and micro-scale lasers [20–22].

More recently, a method of fabricating arrays of ultrahigh-Q microcavities has been developed, by combining surface-tension-induced reflow with modern lithographic techniques [23]. This synergistic approach allows creating dense arrays of ultrahigh-Q silica microcavity structures in parallel on a silicon wafer (Figure 1.1), allowing the integration with complementary electrical, optical or mechanical functionality. In addition to the capability of achieving ultrahigh Q-factors, toroidal microcavities have a flexibility in mode volume design/optimization and possess a simpler resonance spectrum when compared to the spherical microcavities due to additional confinements provided by the toroidal geometry.[3]

The coupling schemes to surface-tension-induced microcavities have been improved in order to achieve phase-matching, criticality, selectivity, and ideality [1]. With the ultrahigh-Q microcavity, it is necessary to have a high-efficiency coupler to couple input photons into and to extract cavity photons from the cavity. Free-space excitation was typically used to study the resonance characteristics of liquid droplets in the early stage. However, the coupling efficiency with this scheme was inherently low and limited by the radiative characteristics of the cavity [1]. Therefore, various coupling devices have been developed during the last decade and the most successful ones were the evanescent wave couplers such as prism couplers, side polished fiber couplers, angle polished fiber tips, pedestal antiresonant reflecting waveguides, and tapered fiber couplers. Among these, tapered fiber

[2] In a recent experiment on a *crystalline* CaF_2 millimeter-sized polished spheroidal cavity, Q-factor as high as 2×10^{10} has been demonstrated [11].

[3] For the spherical microcavity, main factors determining the cavity mode volume are the radius (or equivalently, the diameter) and the refractive index of the sphere. However, the modification of the minor diameter can also increase/decrease the cavity mode volume for the toroidal microcavity.

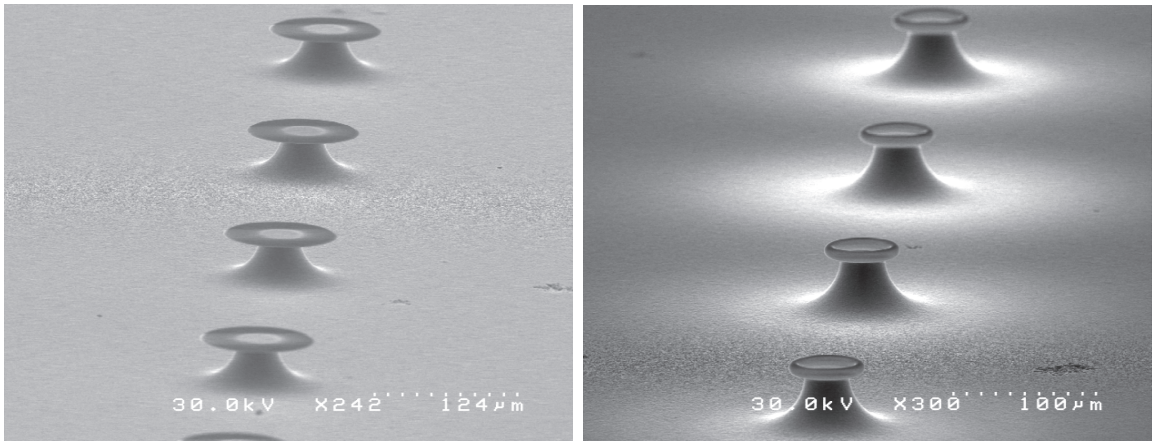

Figure 1.1: Arrays of silica microdisk before CO_2 laser reflow and microtoroid on a silicon substrate after the reflow.

couplers have been extremely successful in realizing near-ideal coupling to a high-Q surface-tension-induced microcavity.[4] These tapered fiber couplers have been shown to have a high ideality (minimized parasitic coupling to higher-order fiber modes) and a criticality ($< 0.02\%$ transmission) with low insertion/junction loss [25, 26]. More detailed reviews on the surface-tension-induced microcavity can be found in [1, 14, 27–29] and the references therein.

1.2 Organization of the thesis

This thesis will be organized as follows: In chapter 2, as an introduction to the surface-tension-induced microcavity, two simple modeling approaches will be presented. Basic concepts and properties of the optical microcavity will be defined and summarized to make this thesis self-contained. In chapter 3, characteristics of the toroidal microcavities will be theoretically analyzed using an iterative perturbation expansion method. By this theoretical approach, cavity mode field, cavity mode volume, resonance wavelength, phase-matching condition, and radiative quality factor will be derived semianalytically within the limit of perturbation expansion. With this theoretical background on hand, various laser systems with different gain media, utilizing the high-Q toroidal microcavity as a laser resonator, will be investigated in detail in the subsequent chapters. In chapter 4, II-VI chemically

[4] Tapered fiber coupling has also been used to couple light not only into surface-tension-induced microcavity but also to the planar photonic crystal microcavity [24].

synthesized semiconductor nanocrystals, specifically CdSe/ZnS (core/shell) nanocrystals with high quantum yield and narrow size distribution, will be coated on the surface of the toroidal microcavity and the lasing at both room and liquid nitrogen temperature will be investigated via free-space or tapered-fiber excitation. Extremely low threshold down to 9.9 fJ is demonstrated, proving the high efficiency of the tapered fiber coupling scheme and the feasibility of the quantum dot density control. In chapter 5, erbium-implanted microcavity lasers are demonstrated experimentally and theoretically. After a simple analytic modeling of the erbium-implanted toroidal microcavity laser using a coupling-of-mode formalism, experimental characterization will follow in close relation with the developed analytic model. Low threshold operation down to $\sim$4.5 μW and lasing wavelength control by changing the cavity loading condition is demonstrated. In chapter 6, laser oscillation utilizing nonlinear optical effects in silica is investigated. Especially, Raman and parametric oscillations are demonstrated in the ultrahigh-Q silica toroidal microcavity and it is shown that both oscillation regimes can be accessed by a change of coupling condition in addition to the geometrical cavity aspect ratio control. Detailed modeling will be briefly summarized and the qualitative reasoning for this observation will be given. In the last chapter, I will present a brief summary.

Chapter 2

Basic Properties of Optical Microcavities

In this chapter, basic properties of optical microcavities will be summarized to provide a fundamental insight into the optical microcavity. This will be accomplished by introducing two well-defined modeling approaches that are applicable to different regimes of interest. The first one is a coupling-of-modes formalism that is appropriate for modeling modes of an optical microcavity with input/output coupling [30]. The second one is a well-known exact/approximate analytic solution to the Helmholtz equation for dielectric open spherical microcavities from which various characteristics can be derived [29, 31–35].

2.1 Coupling-of-modes formalism

For a detailed description of high-Q optical microcavities, the coupling-of-modes formalism paves a nice and simple way to understand the basic properties of surface-tension-induced optical microcavity especially with a tapered fiber coupling [26, 30, 36, 37].[1] A governing equation for a cavity field amplitude can be written as,[2]

$$\frac{da}{dt} = i\omega_0 a - \frac{1}{2}\left(\sigma_0^2 + \sum_{j=0} \kappa_j^2\right) a + i\kappa_0 s, \tag{2.1}$$

[1] This modeling with a positive-frequency component of the mode amplitude is only applicable to low loss resonators because the loss of a resonator will couple two separate first order differential equations for the positive- and the negative-frequency component. For further details, see [30].

[2] This equation can be derived from a second-order differential equation for a harmonic oscillator.

where a is the cavity field amplitude ($|a|^2$ is normalized to the cavity energy),[3] ω_0 is the resonant (angular) frequency, σ_0^2 is the rate of (energy) loss related to intrinsic cavity dissipations, κ_j^2 ($j > 0$) is the rate of loss to higher order modes of the tapered fiber, κ_0^2 is the coupling rate for the fundamental tapered fiber (power-normalized) mode to the cavity (energy-normalized) mode (and vice versa),[4] and s is the input field amplitude (normalized to the power) in the tapered fiber waveguide. To maintain the simplicity, a modal coupling by counter-propagating mode is assumed to be negligible. In addition, the governing equation (2.1) can be further simplified by assuming a negligible parasitic coupling to the higher order tapered fiber modes ($\sum_{j>0} \kappa_j^2 \ll \kappa_0^2$):

$$\frac{da}{dt} = i\omega_0 a - \frac{1}{2}\left(\sigma_0^2 + \kappa_0^2\right) a + i\kappa_0 s. \tag{2.2}$$

Now, let's assume that the input has an excitation frequency ω. Then, the input and the cavity field amplitude take the form: $s = \tilde{s}e^{i\omega t}$ and $a = \tilde{a}e^{i\omega t}$. The governing equation (2.2) can be written for a slowly varying field amplitude $\tilde{a}$:

$$\frac{d\tilde{a}}{dt} = i\left(\omega_0 - \omega\right)\tilde{a} - \frac{1}{2}\left(\sigma_0^2 + \kappa_0^2\right)\tilde{a} + i\kappa_0\tilde{s}. \tag{2.3}$$

This simplified governing equation will be investigated further in the subsequent sections.

2.1.1 Cavity Q-factors

Cavity Q-factor is one of the fundamental parameters characterizing the *quality* of a resonator. The concept of a Q-factor is universal and is applied to numerous resonating systems. The general definition of the Q-factor is given by,

$$Q \equiv \frac{2\pi(\text{stored energy})}{\text{energy loss per cycle}}. \tag{2.4}$$

The Q-factor of a microcavity can be expressed as a function of the parameters of coupling-of-modes formalism and this can be done by solving the equation (2.3) in time- or frequency-domain. If the input takes the form: $\tilde{s}(t) = \tilde{s}_0\left[1 - u(t)\right]$, where $u(t)$ is the unit step function,

[3] The cavity field amplitude a can also be associated with the annihilator operator $\hat{a}$.

[4] This symmetric coupling coefficient is a result of power conservation (lossless junction) and time-reversal symmetry [38].

then the decaying solution for $|a(\omega,t)|^2$ to the equation (2.3) can be written as (for $t \geq 0$),

$$|a(\omega,t)|^2 = |a(\omega,0)|^2 \exp\left[-\left(\sigma_0^2+\kappa_0^2\right)t\right], \tag{2.5}$$

where $|a(\omega,0)|^2$ is given by,[5]

$$|a(\omega,0)|^2 = \frac{\kappa_0^2|\tilde{s}_0|^2}{\left(\omega-\omega_0\right)^2+\left(\sigma_0^2+\kappa_0^2\right)^2/4}. \tag{2.6}$$

Using the definition (2.4), the Q-factor can be written as,

$$Q = \frac{2\pi|a(t_0)|^2}{-\frac{\lambda}{c}\frac{d|a(t)|^2}{dt}\Big|_{t=t_0>0}} = \frac{2\pi c}{\lambda\left(\sigma_0^2+\kappa_0^2\right)}. \tag{2.7}$$

As can be seen from the equation (2.7), the total (loaded) Q-factor of a surface-tension-induced microcavity depends on the constituting dissipation mechanisms and can be decomposed as,

$$\begin{aligned}\frac{1}{Q} &= \underbrace{\frac{1}{Q_{mat}}+\frac{1}{Q_{ss}}+\frac{1}{Q_{sc}}+\frac{1}{Q_{rad}}}_{\text{related to intrinsic loss}}+\frac{1}{Q_{ext}} \\ &= \frac{1}{Q_0}+\frac{1}{Q_{ext}},\end{aligned} \tag{2.8}$$

where Q is the total quality factor, Q_{rad} is the quality factor determined by the radiative loss of the cavity,[6] and Q_{ext} is the external quality factor due to a coupling to the output waveguide.[7] Several formulas for each of the Q-factors in equation (2.8) are known in closed form:

- Q_{mat} is the quality factor determined by the material loss of the cavity:

$$Q_{mat} = \frac{2\pi n}{\lambda\alpha_{mat}}, \tag{2.9}$$

[5]It should be noted that the frequency dependency of $|a(\omega,0)|^2$ is given by the Lorentzian lineshape. The Q-factor can also be evaluated from the Lorentzian linewidth $\Delta\omega = \sigma_0^2+\kappa_0^2$

[6]This loss is a result of the finite radius of curvature in an axisymmetric open microcavity. The subject of radiative Q-factor will be revisited in section 2.2.4.

[7]Intrinsic and external Q-factors can also be expressed in terms of rate of loss or lifetime; $Q_0 = 2\pi c/(\lambda\sigma_0^2) = \omega\tau_0$, $Q_{ext} = 2\pi c/(\lambda\kappa_0^2) = \omega\tau_{ext}$.

where α_{mat} is the linear loss of the cavity material. For fused silica with very low OH^- contents, linear loss of ~ 0.2 dB/km is routinely obtained from fiber transmission experiments. This corresponds to the material-loss limited Q-factor of $\sim 1.3\times 10^{11}$ at 1550 nm. This value is significantly higher than any Q-factor achieved experimentally. Other loss mechanisms such as surface-scattering and/or water-layer absorption should therefore have an effect on the observed lower Q-factors.

- Q_{ss} is the quality factor determined by surface scattering loss induced by the roughness of the cavity surface. For a spherical microcavity, it is given by,

$$Q_{ss} \sim \frac{3n^2(n^2+2)^2}{(4\pi)^3(n^2-1)^{5/2}} \frac{\lambda^{7/2} D^{1/2}}{\sigma^2 B^2}, \tag{2.10}$$

  where D is the diameter of the spherical microcavity, σ is the rms surface roughness, and B is the correlation length of the roughness [2].

- Q_{sc} is the quality factor determined by the surface contamination loss and is given specifically for a water layer:[8]

$$Q_{sc,w} \sim \sqrt{\frac{\pi}{8n^3}} \frac{D^{1/2}}{\delta \lambda^{1/2} \beta_w(\lambda)}, \tag{2.11}$$

  where δ is the water layer thickness and $\beta(\lambda)$ is the absorption coefficient of water [2]. However, this formula is shown to be valid only for relatively large microspheres, and underestimates Q-factor in the 1550 nm [33]. To model the water-absorption limited Q-factor more accurately, it is necessary to calculate the following expression numerically:

$$Q_{sc,w} = \frac{2\pi n}{\lambda \sigma_w(\lambda)} \frac{\int_0^{2\pi}\int_0^{\infty} I(r,\phi) r dr d\phi}{\int_0^{2\pi}\int_0^{\infty} I(r,\phi) n_w(r,\phi) r dr d\phi}, \tag{2.12}$$

  where $\sigma_w(\lambda)$ is the absorption cross section of the water molecule, I is the intensity, and $n_w(r,\phi)$ is the concentration profile of adsorbed water.

[8] For a silica cavity, most of the surface contamination comes from the adsorption of water molecules or the chemoposition of OH^-.

2.1.2 Transmission

Assuming a steady-state condition in the equation (2.3), the following equality holds for the cavity field amplitude:

$$\frac{a}{s} = \frac{i\kappa_0}{i\left(\omega - \omega_0\right) + \left(\sigma_0^2 + \kappa_0^2\right)/2}. \tag{2.13}$$

The transmission is then given by the following,[9]

$$T(\omega) = \left|\frac{t_0}{s} + i\kappa_0\frac{a}{s}\right|^2 \simeq \frac{\left(\omega - \omega_0\right)^2 + \left(\sigma_0^2 - \kappa_0^2\right)^2/4}{\left(\omega - \omega_0\right)^2 + \left(\sigma_0^2 + \kappa_0^2\right)^2/4}. \tag{2.14}$$

By introducing a normalized coupling parameter given by $K \equiv \kappa_0^2/\sigma_0^2$, the transmission for the case of resonant excitation ($\omega - \omega_0 = 0$) can be simply written as,[10]

$$T = \left(\frac{1-K}{1+K}\right)^2. \tag{2.15}$$

Three regimes of the coupling [25, 26, 38] can be defined based on the equation (2.15).

- Undercoupled regime ($K < 1$): Coupling rate into the resonator is smaller than the intrinsic energy loss rate of the cavity ($\kappa_0^2 < \sigma_0^2$). This corresponds to the regime where the external Q-factor is larger than the intrinsic Q-factor ($Q_{ext} > Q_0$).

- Critical coupling point ($K = 1$): Coupling rate is matched with the intrinsic energy loss rate of the cavity ($\kappa_0^2 = \sigma_0^2$). In this case, the transmission drops down to zero.

- Overcoupled regime ($K > 1$): Coupling rate into the resonator is larger than the intrinsic energy loss rate of the cavity ($\kappa_0^2 > \sigma_0^2$). This corresponds to the regime where the external Q-factor is smaller than the intrinsic Q-factor ($Q_{ext} < Q_0$).

Figure 2.1 shows the typical measured transmission of a microsphere-tapered fiber system with a fitting curve calculated by the equation (2.15). Three distinct regimes of the coupling

[9] For a high-Q optical microcavity, the coupling is very weak, i.e., $\kappa_0 \ll 1$ and the transmitted field amplitude is given approximately by $t_0 \simeq s$ [26].

[10] The coupling coefficient κ_0^2 is a function of a gap width between the cavity and the tapered fiber coupler whereas the intrinsic loss rate σ_0^2 is independent of the gap width. Therefore, the normalized coupling parameter K becomes a function of the gap width.

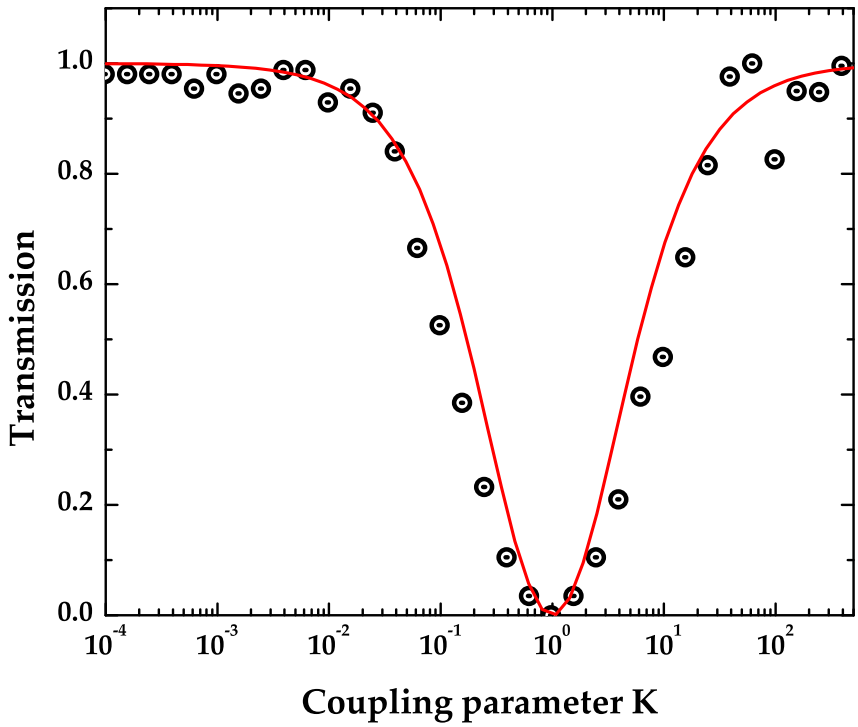

Figure 2.1: Measured transmission of a tapered fiber coupled toroidal microcavity. Red line is a best-fit to the measured data using the equation (2.15).

are clearly shown in this graph with near zero transmission at the critical coupling point ($K = 1$).

2.1.3 Cavity build-up factor

The presence of a high-Q cavity can dramatically increase the density of photonic states at the resonance and can result in a resonant build-up of the cavity field amplitude. Energy inside a microcavity can be expressed as a function of loss/coupling rates and input pump power from the equation (2.13):

$$|a|^2 = \frac{\kappa_0^2}{(\omega - \omega_0)^2 + \left(\sigma_0^2 + \kappa_0^2\right)^2 / 4} |s|^2. \tag{2.16}$$

By converting the intracavity energy into the cavity circulating power,[11] the cavity build-up factor can be expressed in terms of the normalized coupling parameter K, the intrinsic quality factor of the cavity Q_0, and the effective radius of the cavity R_e:

$$\frac{P_{cavity}}{P_{fiber}} = \frac{\omega_0 c}{2\pi n R_e} \frac{K/Q_0}{(\omega - \omega_0)^2 + (\omega_0/Q_0)^2 \left(\frac{1+K}{2}\right)^2} Q_0. \tag{2.17}$$

For the case of resonant excitation of the cavity, the above equation reduces to

$$\frac{P_{cavity}}{P_{fiber}} = \underbrace{\frac{\lambda}{\pi^2 n R_e} \frac{K}{(1+K)^2} Q_0}_{\text{Cavity build-up factor}}, \tag{2.18}$$

where P_{cavity} is the circulating power inside the cavity, P_{fiber} is the input power in the tapered fiber, λ is the resonance wavelength, n is the refractive index of the cavity material, and R_e is the effective radius of the cavity. The combined system of a high-Q cavity and an efficient tapered fiber coupler is attractive in various applications partly due to the above simple scaling rule (cavity build-up factor). For example, with typical resonator parameters of $R_e = 30$ μm, $n = 1.46$, $Q_0 = 10^8$, $K = 1$, and $\lambda = 1550$ nm, input power of 1 mW will be scaled up to a cavity circulating power of $\sim$90 W. This huge resonant energy buildup will decrease the "input" threshold power of a microcavity-based laser or a nonlinear wave

[11] This conversion is done by dividing both sides of the equation (2.16) by cavity round-trip time, $\tau_{rt} = 2\pi n R_e / c$.

generation in a microcavity. Latter parts of this thesis will provide a clear verification on the advantages provided by huge cavity build-up factors in real device applications.

2.2 Analytic theory of spherical microcavity

In this section, analytic theory of a high-Q dielectric *spherical* microcavity will be reviewed.[12] For a homogeneous spherical microcavity,[13] both exact and approximate analytic solutions for the cavity field have been known for some time and other characteristics of spherical microcavities have been derived automatically based on those analytic solutions [29, 31–34]. Using this analytic theory, a deeper understanding of the spherical microcavity can be obtained and this will be the starting point for the modeling of a high-Q dielectric *toroidal* microcavity in the next chapter.

2.2.1 Cavity mode field

The cavity mode field of a dielectric spherical microcavity can be obtained by solving the Helmholtz equation in spherical polar coordinates. Exact solutions are given in [29, 31, 33, 35]. These exact solutions can be approximated further by assuming a large polar mode number l and a constant direction of polarization.[14] Approximate bounded TE/TM modes with three mode numbers (q, l, m) can be expressed as follows,[15]

$$\vec{E}_{TE}(r,\theta,\phi) = \begin{cases} \hat{\theta} N_s \exp\left(\pm im\phi - \frac{m}{2}\theta^2\right) H_{l-m}(\sqrt{m}\theta) j_l(k n_s r) & (r \le R) \\ \hat{\theta} N_s \exp\left(\pm im\phi - \frac{m}{2}\theta^2\right) H_{l-m}(\sqrt{m}\theta) j_l(k n_s R) \exp[-\alpha_s (r-R)] & (r > R) \end{cases}$$

$$\vec{H}_{TE}(r,\theta,\phi) = i\frac{1}{\omega\mu}\nabla \times \vec{E}_{TE}(r,\theta,\phi), \tag{2.19}$$

[12] In this context, the word "analytic" is used for the solution of the Helmholtz equation. Still, other expressions can be transcendental or/and may not be solved analytically.

[13] For a homogeneous microsphere the relative permittivity takes the form: $\epsilon(\vec{r}) = n_s^2$ $(|\vec{r}| \le R_0)$, $\epsilon(\vec{r}) = n_0^2$ $(|\vec{r}| > R_0)$.

[14] This approximate solution is more accurate for a mode confined near the equatorial plane ($\theta \ll 1$), i.e., for a small $|l - m|$.

[15] Three indices (q, l, m) represent radial, polar, and azimuthal mode number, respectively. A mode number p can also be assigned to the polarization, which can be either TE ($p = 0$) or TM ($p = 1$).

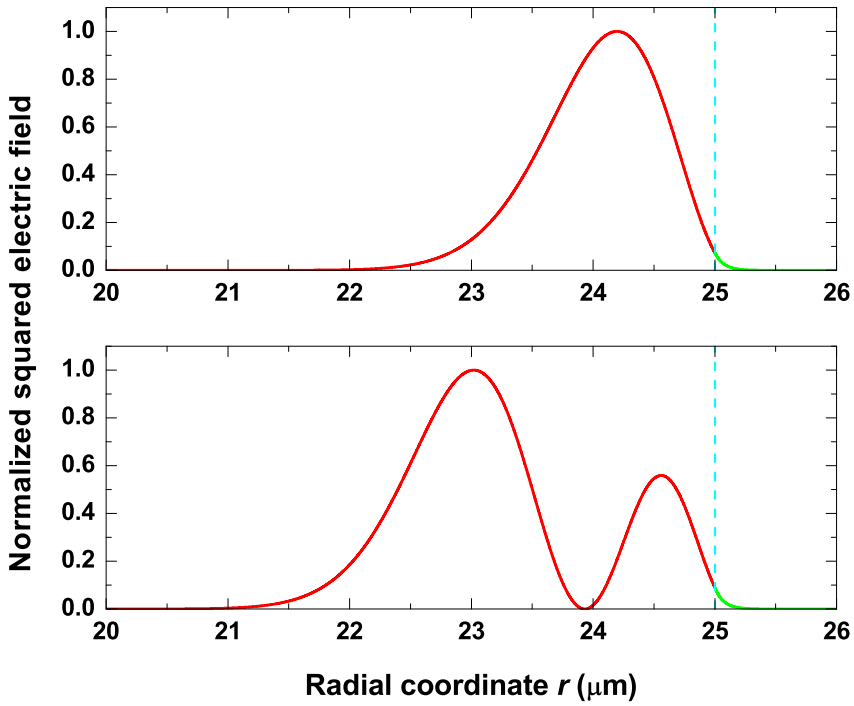

Figure 2.2: Normalized squared electric field, $|E_\theta|^2$, for the two lowest radial mode number $n = 1,\ 2$. The polar and the azimuthal mode number are $l = m = 139$. The microsphere boundary at $R = 25\ \mu$m is shown in the graph.

$$\vec{H}_{TM}(r,\theta,\phi) = \begin{cases} \hat{\theta} N_s \exp\left(\pm im\phi - \frac{m}{2}\theta^2\right) H_{l-m}(\sqrt{m}\theta) j_l(k n_s r) & (r \le R) \\ \hat{\theta} N_s \exp\left(\pm im\phi - \frac{m}{2}\theta^2\right) H_{l-m}(\sqrt{m}\theta) j_l(k n_s R) \exp[-\alpha_s (r-R)] & (r > R) \end{cases}$$

$$\vec{E}_{TM}(r,\theta,\phi) = -i\frac{1}{\omega\epsilon_0 n^2}\nabla \times \vec{H}_{TM}(r,\theta,\phi), \tag{2.20}$$

where n_s is the refractive index of the sphere, H_{l-m} is the Hermite polynomial of order $l-m$, j_l is the spherical Bessel function of the first kind and other related parameters are given in [34]. Figure 2.2 shows a normalized squared electric field $|E_\theta|^2$ for the two lowest radial mode numbers $n = 1,\ 2$. The polar and the azimuthal mode number are fixed to $l = m = 139$. The microsphere-air boundary at $R = 25\ \mu$m is shown in the graph. Figure 2.3 shows the normalized squared electric field $|E_\theta|^2$ in the polar direction. The polar and the azimuthal mode number are given by $l = m = 139$ (top) and $l = m+1 = 139$ (bottom).

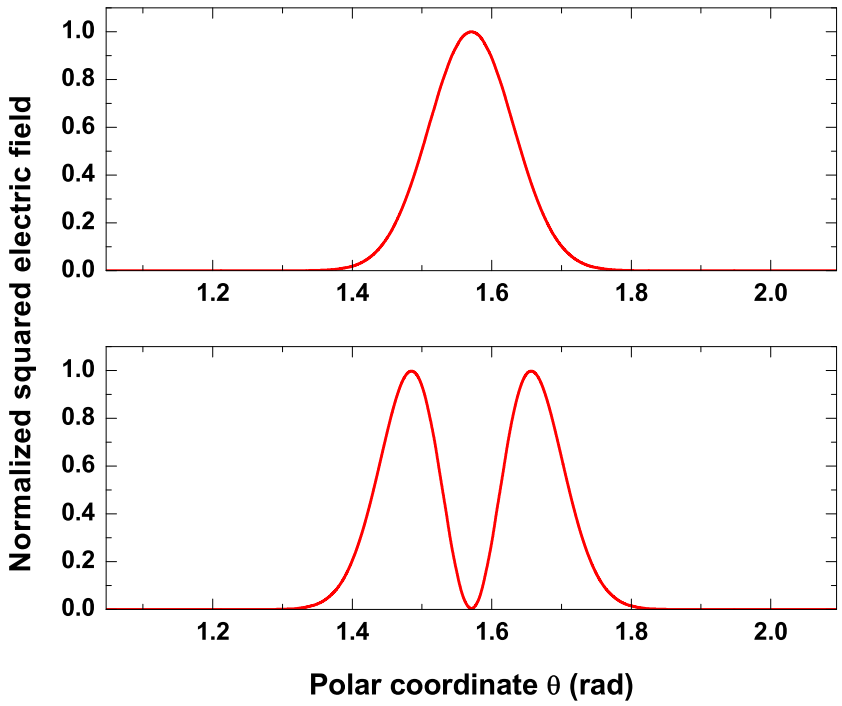

Figure 2.3: Normalized squared electric field, $|E_\theta|^2$, in the polar direction. The polar and the azimuthal mode number are $l = m = 139$ (top) and $l = m + 1 = 139$ (bottom).

2.2.2 Resonance wavelength

A characteristic equation can be obtained by matching tangential fields at the dielectric cavity boundary. The following characteristic equation is obtained from the approximate analytic solution (2.19) and (2.20):

$$\left(\eta_s \alpha_s + \frac{l}{R}\right) j_l(k n_s R) = k n_s j_{l+1}(k n_s R), \tag{2.21}$$

where $\eta_s = 1$ for TE modes and $\eta_s = n_s^2/n_0^2$ for TM modes.[16] A more accurate resonance wavelength can be calculated by the characteristic equation (obtained from the exact solutions). This characteristic equation is given by [12, 31–33],

$$n_s^{1-2p} \frac{[n_s k R j_l(n_s k R)]'}{n_s k R j_l(n_s k R)} = \frac{[k R h_l^{(1)}(k R)]'}{k R h_l^{(1)}(k R)}, \tag{2.22}$$

where p is the polarization mode number (0 for TE and 1 for TM), and the differentiation is with respect to the argument. By solving this transcendental equation for a complex-valued wavenumber $k = k_r + i k_i$, the resonance wavelength and width (caused by radiative tunneling) can be estimated as $\lambda = 2\pi/k_r$ and $\Delta\lambda = 4\pi k_i / k_r^2$. However, instead of numerically solving the transcendental equation (2.22), an asymptotic expansion for the resonance wavelength has been found [39, 40]:

$$\lambda_{q,l} = 2\pi R \left[\frac{\nu}{n_s} - \frac{\zeta_q}{n_s} \left(\frac{\nu}{2}\right)^{1/3} + \sum_{k=0}^{k_{max}} \frac{d_k(n_s, \zeta_q)}{\nu^{k/3} (n_s^2 - 1)^{(k+1)/2}} \right]^{-1}, \tag{2.23}$$

where ζ_q is the qth zero of the Airy function, $\nu = l + 1/2$, and coefficients d_k's are given in [40].

2.2.3 Cavity mode volume

Cavity mode volume V can be calculated once the cavity mode field is obtained. The definition of a cavity mode volume depends on the application. Among those, the following

[16] In this expression, all the modes ($|m| \leq l$) having the same polar mode number l are degenerate. However, a slight eccentricity will break this degeneracy. For further details, see [25, 29, 35].

definition of the mode volume will be used throughout this thesis if not stated explicitly:

$$V = \frac{\int_{V_Q} \epsilon(\vec{r})|\vec{E}(\vec{r})|^2 d^3\vec{r}}{|\vec{E}_{max}|^2}. \tag{2.24}$$

For a nonlinear process in the microcavity (See chapter 6 and Appendix B), a different definition is used to calculate (nonlinear) cavity mode volume:

$$V = \frac{\left(\int_{V_Q} |\vec{E}(\vec{r})|^2 d^3\vec{r}\right)^2}{\int_{V_Q} |\vec{E}(\vec{r})|^4 d^3\vec{r}}, \tag{2.25}$$

where V_Q denotes a quantization volume needed to calculate the mode volume. An approximate analytic formula for the nonlinear mode volume has been found by Braginsky et al. [10]:

$$\begin{aligned} V &\simeq 3.4\pi^{3/2}\left(\frac{\lambda}{2\pi n}\right)^3 l^{11/6}\sqrt{l-m+1} \\ &\propto D^{11/6}\left(\frac{\lambda}{n}\right)^{7/6} \qquad (\text{for } \ l=m). \end{aligned} \tag{2.26}$$

The scaling rule provided by this equation is quite useful for a rough estimate for the cavity mode volume.

2.2.4 Radiative Q-factor

Radiation from an open microcavity is a result of energy leaking into the universe and is mainly determined by the curvature of the microcavity. For the spherical microcavity, this radiative Q-factor can be computed numerically by solving the characteristic equation (2.22) for a complex eigenvalue $k = k_r + ik_i$. The radiative Q-factor is then defined by the relation $Q_{rad} = k_r/(2k_i)$ and can be asymptotically approximated as follows (by assuming $k_r R \gg 1$) [32, 41]:

$$Q_{rad} \simeq \frac{1}{2}\left(l+\frac{1}{2}\right) n_s^{-(1-2p)} \left(n_s^2-1\right)^{1/2} \exp\left[2\left(l+\frac{1}{2}\right)(\eta_l - \tanh\eta_l)\right], \tag{2.27}$$

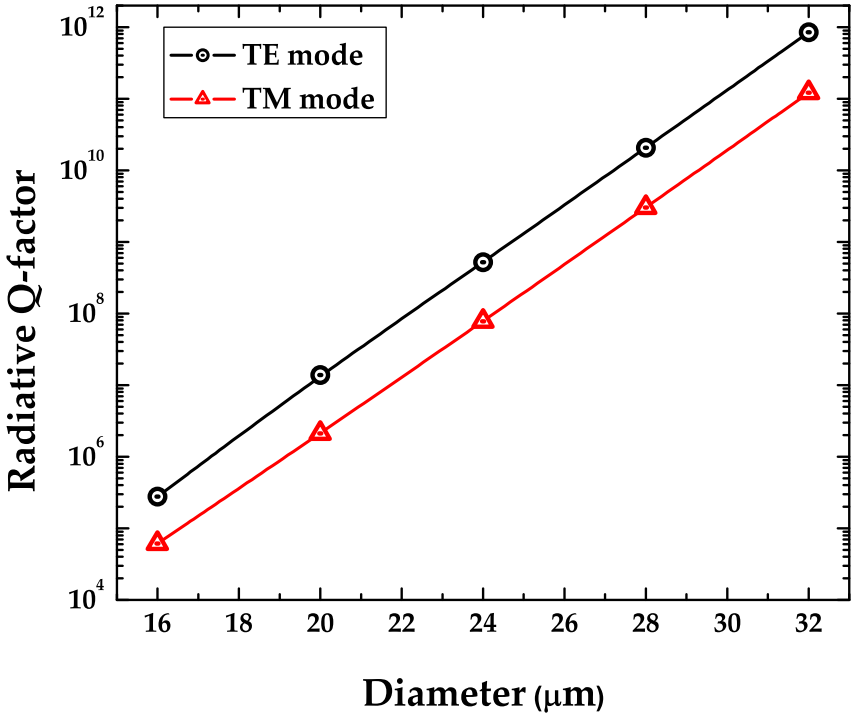

Figure 2.4: Theoretical radiative Q-factor for TE/TM mode ($\lambda \simeq 1.55\,\mu$m) calculated from the equation (2.27).

where η_l is defined as follows,

$$\eta_l = \cosh^{-1}\left[n_s \left(1 - \frac{1}{l+\frac{1}{2}} \left\{ \zeta_q \left[\frac{1}{2}\left(l+\frac{1}{2} \right) \right]^{1/3} + \frac{n_s^{1-2p}}{\sqrt{n_s^2-1}} \right\} \right)^{-1} \right], \tag{2.28}$$

where p is the polarization mode number (0 for TE and 1 for TM), l is the polar mode number, and ζ_q is the qth zero of the Airy function. Figure 2.4 shows calculated radiative Q-factors for TE/TM mode (radial mode number $q = 1$). However, this approximation of the radiative Q-factor is found to be slightly deviated from the result of numerical calculations (FDTD) even though the scaling rule is still applicable [33].

Chapter 3

Semianalytic Theory of Toroidal Microcavity

Among the properties of whispering-gallery type resonators, the cavity mode volume V is one of the critical parameters that characterizes the cavity due to its fundamental relationship with the lasing threshold, nonlinear optical wave generation, and cavity quantum electrodynamics (cQED) [14]. Since the mode volume V of a toroidal microcavity is smaller than that of a spherical microcavity (for the same principal diameter), it is very important to characterize and predict the mode volume in terms of the toroidal microcavity parameters [13]. While intrinsic Q-factors are functions dependent on other physical/chemical properties such as water adsorption, surface scattering, and material absorption, the mode volume V of each polarization (TE or TM) can be estimated more accurately once the geometry of the device (including the material properties such as a refractive index) is clarified. Although the effects of water adsorption, surface scattering, and material absorption will not be investigated, whispering-gallery loss-limited Q-factors [13, 34], which are mainly determined by the geometry and the cavity mode, will be dealt with in this chapter with a perturbation expansion of the cavity mode field and volume current method (VCM) [42, 43].

The cavity mode field of the toroidal microcavity with three integer mode numbers (q, l, m) has not been solved in closed form. Therefore, the other useful metrics of the toroidal microcavity such as cavity mode volumes, radiative (whispering-gallery) Q-factors, phase-matching conditions, resonance wavelengths, and free spectral ranges (FSR) could not be explicitly calculated, and it was necessary to resort to numerical simulation [13]. The complication arises from the inseparability of a scalar wave equation in local toroidal coordinates and the corresponding lack of knowledge for the solutions of these two-dimensional

problems. However, the difficulty of obtaining analytic solutions can be circumvented, and an approximate solution instead of an exact solution can be obtained with a perturbation method using a proper expansion parameter for a "fiber-like" (small inverse aspect ratio) toroidal geometry.

In this chapter, an iterative perturbation expansion method will be applied to calculate the cavity mode field inside and near the periphery of the toroidal microcavity with a small inverse aspect ratio.[1] The cavity mode field in a small inverse aspect ratio toroidal microcavity can be obtained, in principle, by transforming the Helmholtz equation in a Cartesian coordinate system into a scalar wave equation in the local toroidal coordinates [44]. As a result of this transformation, solutions of the transformed wave equation become analytically tractable with the perturbation expansion to a desired order (at the expense of complexity in the solution derived). With the cavity mode field, other useful characteristics are automatically obtained. The limit of this kind of expansion will also be addressed to show the applicability of the perturbation approaches. These perturbation approaches give an excellent qualitative/quantitative agreement with the numerical solutions given by the finite element method (FEM), which justifies the proposed perturbative approach for the toroidal microcavities with small inverse aspect ratio.

3.1 Problem formulations

A local toroidal coordinate system (r, ϕ, θ) that is intuitively suitable for electromagnetic problems with a toroidal geometry will be used throughout the rest of this chapter. Figure 3.1 shows the local toroidal coordinate system with a rendering of the toroidal microcavity structure ($D = 2R$: major diameter, $d = 2a$: minor diameter, $D_p = 2R_p$: principal diameter). The problem can also be formulated based on three scalar Helmholtz equations (each separated from a vector Helmholtz equation) written in Cartesian coordinates, but it will be extremely cumbersome to satisfy the boundary condition at the surface of the toroidal microcavity due to the curved geometry. The inverse aspect ratio δ, defined by the ratio between minor and major diameter a/R, will play an important role in the expansion of the cavity mode field and the subsequent estimation of various cavity characteristics.

[1] In this chapter, only the bound mode approximation will be considered by modeling exponentially decaying field outside the toroidal microcavity boundary.

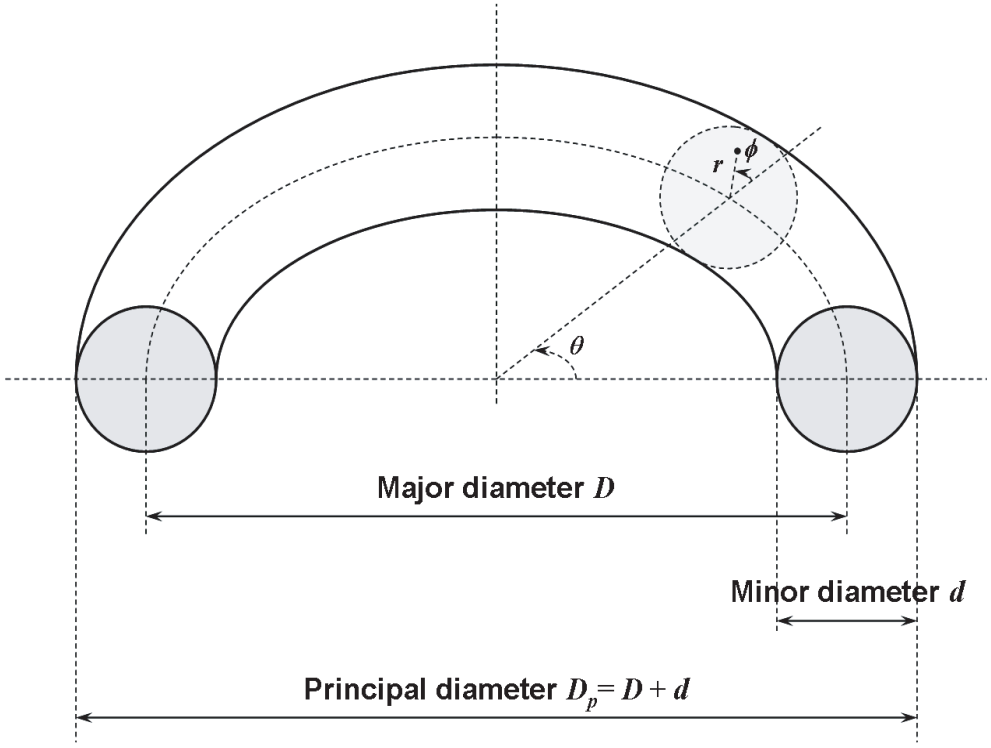

Figure 3.1: A local toroidal coordinate system along with a corresponding boundary of the toroidal microcavity. The definitions of principal ($D_p = 2R_p$), major ($D = 2R$) and minor diameter ($d = 2a$) are illustrated.

For a more accurate modeling, Maxwell's equation with all six field components (E_r, E_ϕ, E_θ, H_r, H_ϕ, H_θ) should be used because the magnitude of nontransverse field components ($|E_r|, |E_\theta|$ for TE, $|H_r|, |H_\theta|$ for TM) may not be negligible compared to that of transverse fields in general toroidal geometry. Therefore, the assumptions of a pure transverse field will need to be carefully investigated. However, for large inverse aspect ratio the assumption of TE/TM modes are verified to be quite accurate [34], and for small inverse aspect ratio the problem is similar to the case of straight fiber that certainly supports TE/TM modes. Therefore, in the following sections, only the TE/TM mode approximation will be considered by solving one scalar wave equation for the toroidal microcavity with small inverse aspect ratio. Although the derived scalar wave equation is not separable in the transverse plane of propagation due to the coupling term induced by the geometrical perturbation from a straight waveguide geometry, the perturbation expansion method can then be utilized to give approximate analytic solutions for the transverse fields. The problem of solving the cavity mode field of the toroidal microcavity is very similar to the problem of bent optical fibers. Lamouroux et al. solved Maxwell's equation without assuming a weak guidance approximation (which is required for decoupling mode calculation with polarization properties) and obtained a general solution of toroidally bent fibers with all six field components up to the first order [45]. However, the applicability of those solutions to the characterization of the toroidal microcavity is inherently limited due to its complexity in the derived formula. Since the nontransverse field components can be assumed to be very small compared to the transverse field components for the small inverse aspect ratio (for example, $|E_{r,\theta}| \ll |E_\phi|$ for TE mode), the scalar wave equation for the transverse field will be used in subsequent evaluations. Then, as has been derived previously for the evaluation of the mode field in the bent optical fibers, the scalar Helmholtz equation can be reduced to the following simple wave equation in transverse local toroidal coordinates after separating $(1 + r/a\cos\phi)^{-1/2}e^{-jm\theta}$ factor (the round-trip phase shift should be multiples of 2π):

$$\left(\frac{\partial^2}{\partial r^2} + \frac{1}{r}\frac{\partial}{\partial r} + \frac{1}{r^2}\frac{\partial^2}{\partial \phi^2} + k^2 n^2\right)\Psi(r,\phi) + \left(1 + \delta\frac{r}{a}\cos\phi\right)^{-2}\left(\frac{1}{4R^2} - \beta^2\right)\Psi(r,\phi) = 0, \quad (3.1)$$

where r and ϕ are the local toroidal coordinates in the transversal plane, k is the wave vector ($k = \omega\sqrt{\mu\epsilon_0}$) in the free-space, n is the refractive index ($= n_0$ for surrounding material),

and β is the intrinsic propagation constant defined with respect to the major radius R.[2]

This scalar wave equation can be solved to an arbitrary order of δ with an assumption of TE/TM mode without separating the wave function into two transverse components. When solving this equation, three integer mode numbers (q, l, m) are naturally introduced to characterize the cavity mode fields. The radial and polar mode number, q and l, determines the type of transverse mode field patterns and azimuthal mode number m, accounts for azimuthal variations of the cavity mode field. This definition of the mode numbers looks similar to that of the microsphere resonators but has a slight different meaning and should be distinguished from the mode numbers (q, l, m) for the microsphere resonators [34]. While the fundamental mode of the microsphere resonator is characterized by the condition $q = 1$, $l = m$, the fundamental mode ($q = 0$, $l = 0$) of the toroidal microcavity resonator is decoupled in terms of polar and azimuthal mode numbers. The transverse electric (magnetic) field can be obtained after solving wave equation (3.1) using the perturbation expansion and transforming the wave function according to the formula:

$$E_\phi = N\left(1 + \delta\frac{r}{a}\cos\phi\right)^{-1/2}\Psi(r,\phi)e^{-jm\theta} \quad \text{(TE modes)}, \tag{3.2}$$

$$H_\phi = N\left(1 + \delta\frac{r}{a}\cos\phi\right)^{-1/2}\Psi(r,\phi)e^{-jm\theta} \quad \text{(TM modes)}, \tag{3.3}$$

where N is a normalization constant obtained from the condition of unit power flow. TE modes are defined by $\vec{E} = \hat{\phi}E_\phi, E_r \simeq 0, E_\theta \simeq 0$ and TM modes are defined similarly as $\vec{H} = \hat{\phi}H_\phi, H_r \simeq 0, H_\theta \simeq 0$. As stated before, the mode field cannot be separated in the coordinates (r, ϕ) which is different from the case of microsphere resonators. The intrinsic propagation constant β is defined as,[3]

$$\beta \equiv \frac{m}{R} = \frac{m}{R_p - a}. \tag{3.4}$$

Similar to the case of microsphere resonators, this propagation constant can be thought as

[2]It will be shown later that this intrinsic propagation constant β should be updated to a modified propagation constant β_e by an iterative procedure in order to improve the accuracy of the modeling.

[3]Note that the major radius R is used in defining the intrinsic propagation constant β. For a spherical microcavity, the sphere radius R_0, which corresponds to the principal radius R_p of the toroidal microcavity, is used. This discrepancy will be resolved with the definition of the modified propagation constant β_e in the following sections.

the wave vector in the net direction of propagation. However, for a more precise characterization of the cavity modes, this should be updated to a modified propagation constant β_e, as will be clear later in this chapter. The objective of the following section is to derive the cavity mode field in terms of the expansion parameter and to show the actual cavity field modes as the mode number changes.

3.2 Properties of toroidal microcavity resonators

Using the scalar wave equation expressed in local toroidal coordinates as introduced in the previous section, a perturbational approach similar to the one given in [44], i.e., a power-series expansion can now be applied to provide analytic approximate solutions to the mode field in the toroidal microcavity.[4]

3.2.1 Cavity mode field

The intrinsic propagation constant β is quantized to sets of discrete values (given by azimuthal mode number m) and the spacing between adjacent βs is determined by the major diameter of the toroid. If the inverse aspect ratio δ is very small ($\delta = a/R < 0.1$), the error made by approximating the cavity mode field patterns using the second order expansion for a wave function will be quite small in subsequent characterization.To increase the accuracy of the results and to use a wider range of minor diameters, the cavity mode field can be expanded further to include higher orders terms. Making use of the perturbation expansion, we can set the wave function:

$$\Psi = \sum_{j=0} \delta^j \Psi^{(j)}. \tag{3.5}$$

Truncating the wave function expansion up to the second order and inserting it to the transform equation (3.2), the electric field can be expressed as,[5]

$$\vec{E} = \hat{\phi} N \left(1 + \delta \frac{r}{a} \cos\phi\right)^{-1/2} \{\Psi^{(0)}(r,\phi) + \delta\Psi^{(1)}(r,\phi) + \delta^2\Psi^{(2)}(r,\phi)\} e^{-jm\theta}, \tag{3.6}$$

[4]In the original paper written for a bent optical fiber [44], the propagation constant β is also expanded as $\beta^2 = \beta_{(0)}^2 + \beta_{(2)}^2\delta^2$. However, this makes the cavity field expression more complicated when the desired order of perturbation theory becomes larger. Therefore, in this chapter, different approach has been taken to modify the propagation constant with the iterative method.

[5]Without any loss of generality, only TE mode will be considered in this chapter. However, this method can be applied to TM modes in the same way.

where N is the (power) normalization constant that can be obtained by the volume integral of the squared electric field divided by effective equatorial path length $2\pi R_e$.The scalar wave equation for each order is given by,

$$D\Psi^{(0)}(r,\phi) = 0, \tag{3.7}$$

$$D\Psi^{(1)}(r,\phi) = -2\beta^2\left(\frac{r}{a}\right)\cos\phi\,\Psi^{(0)}(r,\phi), \tag{3.8}$$

$$D\Psi^{(2)}(r,\phi) = -2\beta^2\left(\frac{r}{a}\right)\cos\phi\,\Psi^{(1)}(r,\phi) + \left[3\beta^2\left(\frac{r}{a}\right)^2\cos^2\phi - \frac{1}{4a^2}\right]\Psi^{(0)}(r,\phi), \tag{3.9}$$

where the differential operator D is given by,

$$D \equiv \left[\frac{\partial^2}{\partial r^2} + \frac{1}{r}\frac{\partial}{\partial r} + \frac{1}{r^2}\frac{\partial^2}{\partial\phi^2} + \left(k^2n^2 - \beta^2\right)\right]. \tag{3.10}$$

After solving the wave equations of each order, the electric fields inside/outside the transverse toroidal plane can be obtained by substituting the following wave functions into the equation (3.6) for the mode number $(q,l,m) = (q,0,m)$:

$$\Psi_{in}^{(0)}(\xi,\phi) = \frac{J_0(u\xi)}{J_0(u)}, \tag{3.11}$$

$$\Psi_{out}^{(0)}(\xi,\phi) = \frac{K_0(w\xi)}{K_0(w)}, \tag{3.12}$$

$$\Psi_{in}^{(1)}(\xi,\phi) = 2(\beta a)^2 u\xi^2\frac{J_1(u\xi)}{J_0(u)}\left[\frac{A_0}{\xi^2} - \frac{1}{4u^2}\right]\cos\phi, \tag{3.13}$$

$$\Psi_{out}^{(1)}(\xi,\phi) = 2(\beta a)^2 w\xi^2\frac{K_1(w\xi)}{K_0(w)}\left[\frac{B_0}{\xi^2} + \frac{1}{4w^2}\right]\cos\phi, \tag{3.14}$$

$$\begin{aligned}\Psi_{in}^{(2)}(\xi,\phi) = &-\frac{1}{8u}\frac{J_0(u\xi)}{J_0(u)} + \frac{J_1(u\xi)}{J_0(u)}\left\{-\frac{\xi}{8u} + (\beta a)^2\frac{\xi^3}{4u} + (\beta a)^2\frac{\xi}{4u}\left[\xi^2 + 4A_0(\beta a)^2\right]\cos 2\phi\right\} \\ &+\frac{J_2(u\xi)}{J_0(u)}\left\{C_0 - \frac{(\beta a)^2\xi^2}{4u^2} - \frac{A_0(\beta a)^4\xi^2}{2} + \frac{(\beta a)^4\xi^4}{16u^2} + \left[D_0 - \frac{A_0(\beta a)^4\xi^2}{2} + \frac{(\beta a)^4\xi^4}{16u^2}\right]\cos 2\phi\right\} \\ &-\frac{(\beta a)^4\xi^3}{24u^3}\frac{J_3(u\xi)}{J_0(u)},\end{aligned} \tag{3.15}$$

$$\begin{aligned}\Psi_{out}^{(2)}(\xi,\phi) = &\frac{1}{8w}\frac{K_0(w\xi)}{K_0(w)} + \frac{K_1(w\xi)}{K_0(w)}\left\{\frac{\xi}{8w} - (\beta a)^2\frac{\xi^3}{4w} - (\beta a)^2\frac{\xi}{4w}\left[\xi^2 + 4B_0(\beta a)^2\right]\cos 2\phi\right\} \\ &+\frac{K_2(w\xi)}{K_0(w)}\left\{E_0 - \frac{(\beta a)^2\xi^2}{4w^2} + \frac{B_0(\beta a)^4\xi^2}{2} + \frac{(\beta a)^4\xi^4}{16w^2} + \left[F_0 + \frac{B_0(\beta a)^4\xi^2}{2} + \frac{(\beta a)^4\xi^4}{16w^2}\right]\cos 2\phi\right\} \\ &+\frac{(\beta a)^4\xi^3}{24w^3}\frac{K_3(w\xi)}{K_0(w)},\end{aligned} \tag{3.16}$$

where $\xi = r/a$ denotes the normalized radial coordinate, A_0 and B_0 are the constants given by $\left[\frac{2}{w}\frac{K_1(w)}{K_0(w)} + 1\right] / \left(4u^2\right)$ and $\left[\frac{2}{u}\frac{J_1(u)}{J_0(u)} - 1\right] / \left(4w^2\right)$ respectively (these constants are obtained by matching tangential electric fields at the surface between the toroidal microcavity and the surrounding material), C_0, D_0, E_0, and F_0 are the constants similarly obtained, u and w are the normalized toroidal microcavity parameters ($u^2 + w^2 = v^2$ where v is the v-parameter defined similarly for the case of weakly guiding fibers), J_j denotes the Bessel function of the jth order, and K_j denotes the modified Hankel functions of the jth order. For higher modes with $l \geq 1$, the cavity mode field can be obtained similarly. For TE modes, the magnetic field is then given by,

$$\vec{H} = i\frac{1}{\omega\mu}\nabla \times \vec{E} = i\frac{1}{\omega\mu}\nabla \times \left(\hat{\phi}E_\phi\right). \tag{3.17}$$

After evaluating the above expression in the local toroidal coordinates, the tangential magnetic field is given by,

$$H_\theta = \left[\frac{1}{r} + \frac{\partial}{\partial r}\right] E_\phi. \tag{3.18}$$

Matching H_θ at the toroidal microcavity surface, $r = a$, gives the following characteristic equation for TE modes. The normalized toroidal microcavity parameters u and w can be obtained by solving the following characteristic equation:

$$u\frac{J_1(u)}{J_0(u)} = w\frac{K_1(w)}{K_0(w)} \quad (\mathrm{TE}_{q0m} \text{ mode}), \tag{3.19}$$

where $u = a\sqrt{(nk)^2 - \beta^2}$ and $w = a\sqrt{\beta^2 - (n_0 k)^2}$. With this characteristic equation along with the quantization of the intrinsic propagation constant $\beta = m/R$, rough estimates of the resonance wavelengths and the FSR can be obtained from the equation (3.19). However, for a more precise prediction of the cavity mode field and the resonance wavelengths, an iterative modification of the intrinsic propagation constant and normalized toroidal microcavity parameters is required using the following modified characteristic equation:

$$u_e\frac{J_1(u_e)}{J_0(u_e)} = w_e\frac{K_1(w_e)}{K_0(w_e)} \quad (\mathrm{TE}_{q0m} \text{ mode}), \tag{3.20}$$

where $u_e = a\sqrt{(nk)^2 - \beta_e^2}$, $w_e = a\sqrt{\beta_e^2 - (n_0 k)^2}$, and β_e is the modified propagation constant. For this purpose, an effective radial coordinate r_e and an effective radius R_e of the toroidal microcavity is defined as follows:

$$r_e \equiv a\frac{\iint \epsilon|\vec{E}|^2\xi^2\cos\phi\, d\xi d\phi}{\iint \epsilon|\vec{E}|^2\xi\, d\xi d\phi}, \tag{3.21}$$

$$R_e = R + r_e = R\left(1 + \delta\frac{\iint \epsilon|\vec{E}|^2\xi^2\cos\phi\, d\xi d\phi}{\iint \epsilon|\vec{E}|^2\xi\, d\xi d\phi}\right). \tag{3.22}$$

After obtaining the effective radius R_e with the intrinsic propagation constant β, the resonance wavelength (including the normalized toroidal microcavity parameters, u and w) is updated with the modified propagation constant β_e and the modified characteristic equation (3.20). The modified propagation constant β_e can be obtained by projecting the intrinsic propagation constant to the effective radius R_e [46]:

$$\beta_e = \beta\left(1 + \frac{r_e}{2R}\right)^{-1} = 2\beta\left(1 + \frac{R_e}{R}\right)^{-1}. \tag{3.23}$$

After several iterations with the equations (3.20)–(3.23) and the field expressions (3.11)–(3.16), all the related parameters converge rapidly to the constant values including the resonance wavelength.[6] An asymptotic formula for the modified propagation constant β_e for the fundamental TE mode is found empirically:[7]

$$\beta_e \simeq \frac{2\pi}{\lambda}\left\{n - (2-n)\left[1 + \zeta\left(\frac{a}{\lambda/n}\right)^2\right]^{-1}\right\}, \tag{3.24}$$

where $\zeta = 6.8288$ gives a very good estimate on the modified propagation constant β_e. With a test fitting in the wavelength band of 850 and 1550 nm, the error was found to be below $\sim$1% for the toroidal microcavity with principal diameter ranging from 40 to 80 μm. Figure 3.2 shows a mode index ($n_e = \beta_e/k$) of the fundamental TE mode as a function of minor radius (equation (3.24)). It is worthwhile to note that the principal diameter has

[6] The convergence takes two to four iterations for the examples given in this chapter to give a relatively small error.

[7] This empirical expression is especially useful for the cavity mode field evaluation. With this empirical formula, the cavity mode field at the specified resonance wavelength can be directly obtained without the iterative procedure.

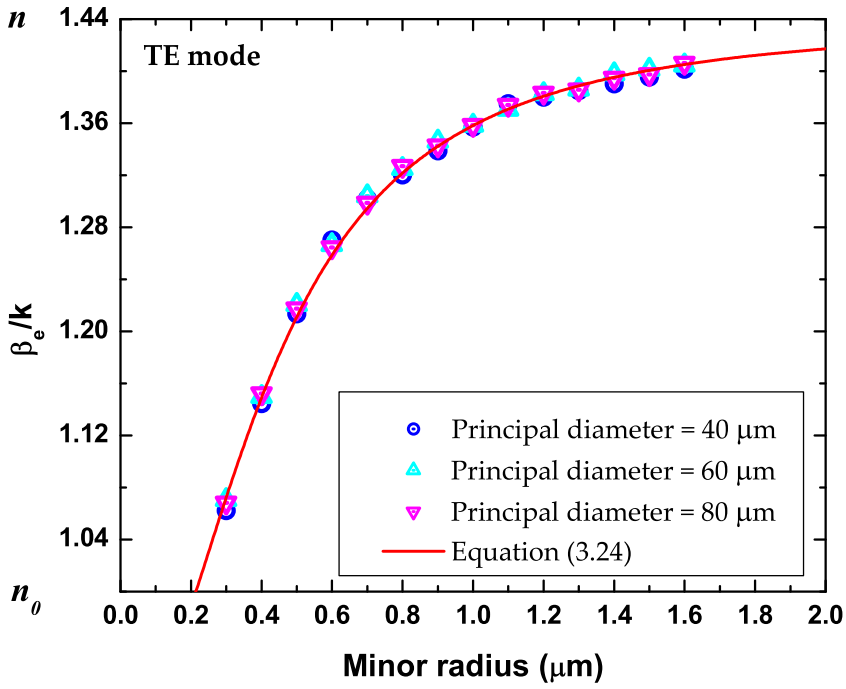

Figure 3.2: The mode index ($n_e = \beta_e/k$) of the fundamental TE mode as a function of minor radius. The iteration method gives a slight variation in mode index due to the change in actual resonance wavelengths (∼1550 nm) for different minor diameters.

a negligible effect on the evaluation of the modified propagation constant for the case of $R_p/\lambda \gg 1$.

Figure 3.3 shows the normalized squared cavity mode field (fundamental TE mode with $(q, l) = (0, 0)$) calculated from the iterative perturbation theory for a toroidal microcavity with minor/principal diameter of 3/60 μm along with a theoretical prediction provided by a finite element method (FEM) simulation. An excellent agreement between the numerical and the semianalytic evaluation can be confirmed. It can be seen that a peak of the cavity mode field shifts toward outside due to the curvature of the geometrical boundary. As the radial mode number q increases, the amount of peak-shift generally decreases compared to that of a fundamental mode and the number of squared cavity mode field maxima in the equatorial plane increases as $2q + 1$ (Figure 3.4). Figure 3.5 shows the normalized squared electric field in the equatorial plane for the fundamental $(q, l, m) = (0, 0, 107)$ and the higher order mode $(q, l, m) = (1, 0, 91)$. The resonance wavelengths are chosen to be near 1.55 μm

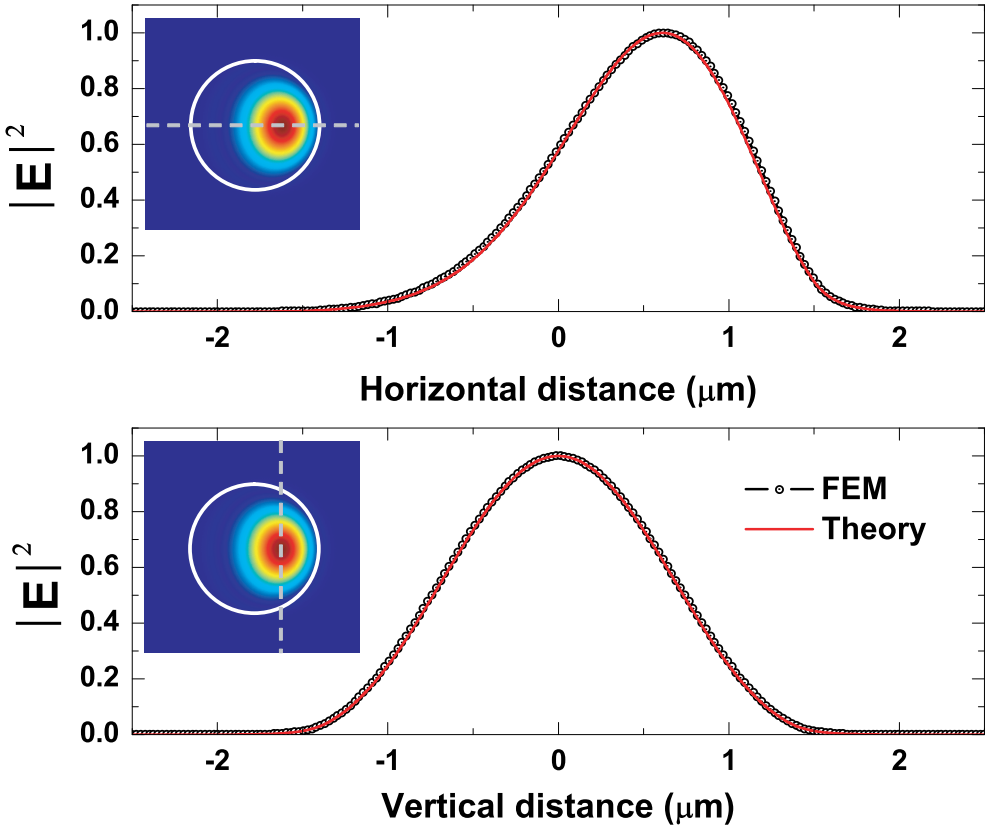

Figure 3.3: The normalized squared cavity mode field (fundamental TE mode with $(q, l) = (0, 0)$) calculated from iterative perturbation theory for a toroidal microcavity with minor/principal diameter of 3/60 μm along with a theoretical prediction provided by a finite element method (FEM) simulation.

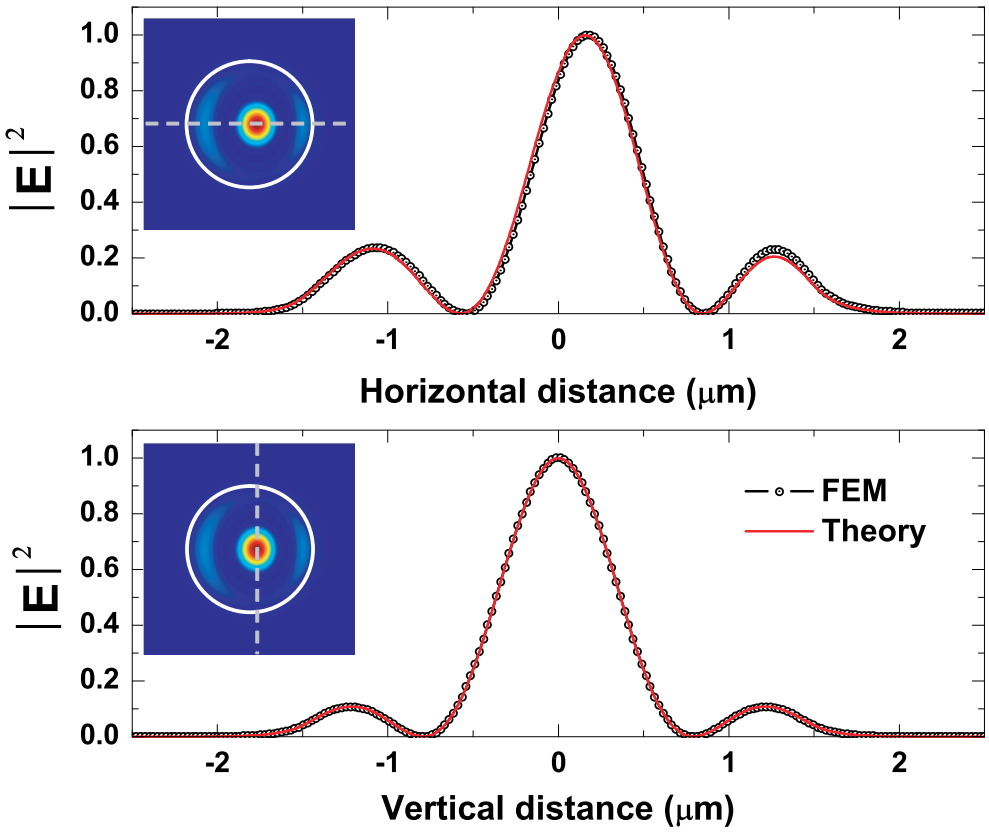

Figure 3.4: The normalized squared cavity mode field (TE mode with $(q, l) = (1, 0)$) calculated from iterative perturbation theory.

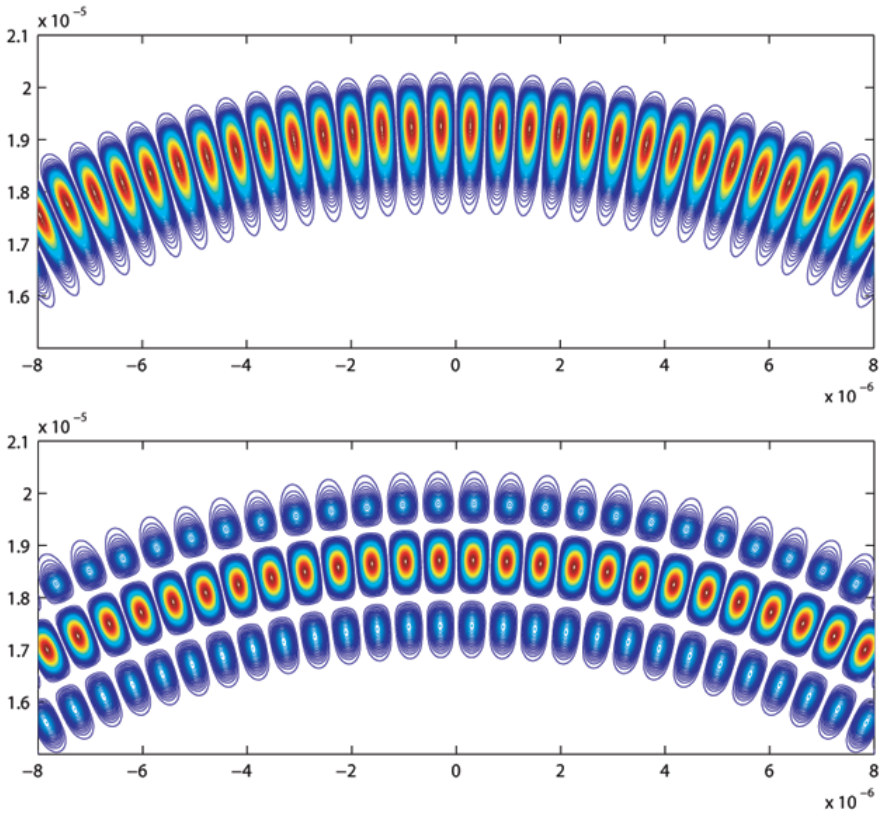

Figure 3.5: The normalized squared electric field in the equatorial plane for the fundamental $(q, l, m) = (0, 0, 107)$ and the higher order mode $(q, l, m) = (1, 0, 91)$. The resonance wavelengths are chosen to be near 1.55 μm. The principal/minor diameters are 40/3 μm.

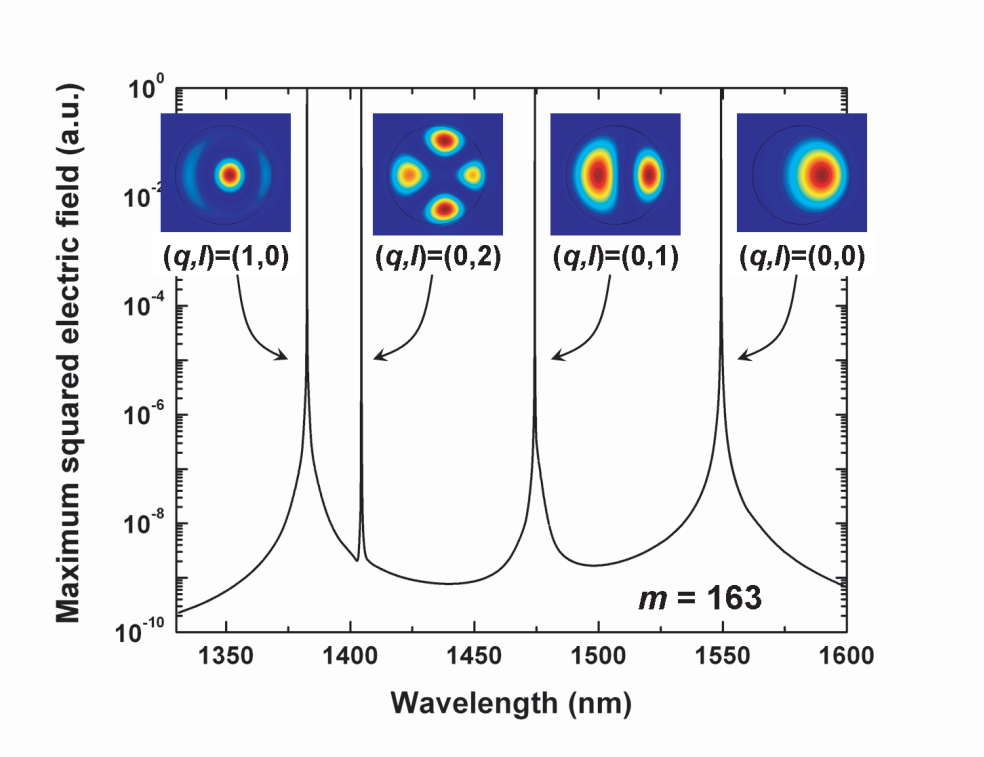

Figure 3.6: Finite element simulations of the resonance spectrum (proportional to the magnitude of squared electric field inside the toroidal microcavity) for a fixed azimuthal mode number $m = 163$.

and the principal/minor diameters are set to 40/3 μm. Figure 3.6 shows the finite element simulation of the resonance spectrum of the TE modes (proportional to the magnitude of squared electric field inside the toroidal microcavity) for a fixed azimuthal mode number $m = 163$. The supported modes for this specific cavity are shown with their mode numbers $(q, l) = (0, 0),\ (0, 1),\ (0, 2)$ and $(1, 0)$, respectively. In this case, the fundamental TE mode is located at 1549.33 nm and the higher order modes are located at shorter wavelengths.

3.2.2 Resonance wavelength

Resonance wavelengths of a toroidal microcavity and corresponding FSR can be obtained as described in the previous section for each TE/TM mode using the characteristic equation along with the iteratively-obtained modified propagation constant β_e.[8] The free spectral

[8]For the purpose of resonance wavelength prediction, eigenvalues of the characteristic equation will be assumed to be real. However, it is worthwhile to mention that the eigenvalues can be complex in general and the complex-valued eigenvalues will give a simple estimation of the radiative Q-factor [32, 35]. Further study will be needed to resolve this.

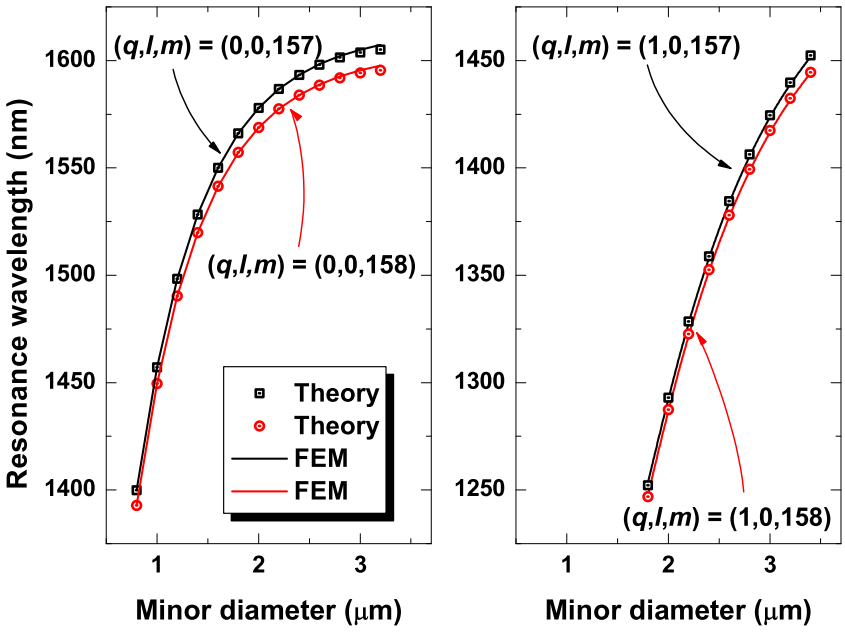

Figure 3.7: Left: Resonance wavelengths for fundamental TE_{00m} modes as a function of minor diameter (principal diameter of toroidal microcavity is fixed at 60 μm). Resonance wavelengths are plotted for two adjacent azimuthal mode numbers $m = 157$ and 158. Right: Resonance wavelengths for TE_{10m} modes.

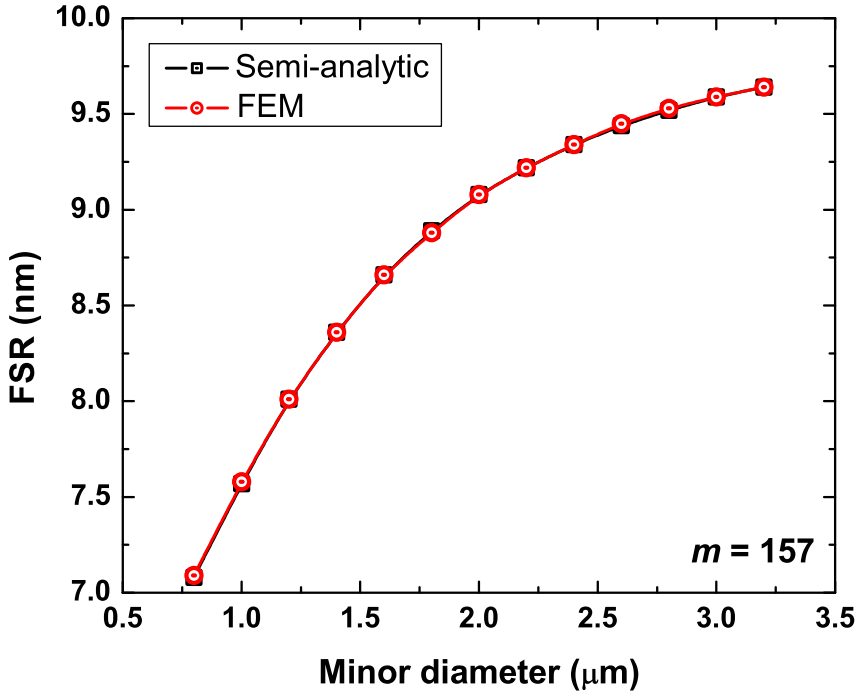

Figure 3.8: FSR calculated for the fundamental cavity mode $m = 157$ and 158 as a function of the minor diameter (the principal diameter of the toroidal microcavity is fixed at 60 μm).

range of the fundamental cavity modes is given by the condition $q = l = 0,\ \Delta m = 1$ and similarly for higher order cavity modes. The resonance wavelength shifts towards shorter wavelengths as the geometry of a spherical microcavity is compressed down to that of a toroidal microcavity for fixed principal diameter D_p and azimuthal mode number m [13]. The dependency of wavelength shifts on dimension can be intuitively understood by a simple analogy. After having separated the azimuthal θ-dependence, the problem reduces to that of a two-dimensional potential well for the confined eigenmodes (effective potential depends on the difference in the refractive index and the curvature). As the dimension of the toroidal microcavity (minor diameter) decreases for a fixed principal diameter, the eigenfrequency spectrum (resonance wavelength) moves toward a higher energy level (shorter wavelength). This resonance wavelength blue-shift is more pronounced if the minor diameter of a toroidal microcavity becomes more compressed to a fiber-like geometry due to the presence of additional confinements from the radial direction. Figure 3.7 shows the resonance wavelengths

for two adjacent azimuthal mode numbers $m = 157$ and 158 as a function of minor diameter of the toroidal microcavity (the principal diameter of the toroidal microcavity is fixed at 60 μm). An excellent agreement in resonance wavelengths is confirmed by comparison with FEM simulations. Even though the iterative prediction for the resonance wavelength starts to deviate as the minor diameter becomes larger, FSR of the microcavity still remains accurate due to the error canceling as shown in Figure 3.8.

3.2.3 Cavity mode volume

The mode volume of a microcavity has substantial impacts on various experiments and theoretical predictions. On the assumption that the cavity quality factor can be maintained at the same level,[9] smaller mode volume is generally preferred to larger mode volume for nonlinear optics, Purcell effects, cavity quantum electrodynamics and lasing threshold reduction in microcavities. The mode volume of a toroidal microcavity can be engineered to some extents by independently modifying the major/minor diameters (while for spherical resonators, only the diameter of sphere can be controlled), or by changing the refractive index of the cavity materials or the polarization of cavity mode field. With the cavity mode fields obtained by the perturbation theoretic analysis, the mode volume of a microcavity with small inverse aspect ratio can be calculated in the local toroidal coordinate system using the definition (2.24) of the cavity mode volume:

$$V = \frac{1}{|\vec{E}_{max}|^2} \iiint \epsilon(r) |\vec{E}(r, \phi, \theta)|^2 \, (R + r\cos\phi) r \, dr d\phi d\theta. \tag{3.25}$$

The semianalytic formula for an electric field (equations (3.6)) can be inserted into the above expression and can be evaluated numerically. It was previously pointed out that the mode volume of the toroidal microcavity consists of two major parts, which are fiber-like contribution for small inverse aspect ratio and sphere-like contribution for large inverse aspect ratio, respectively [13]. For fiber-like mode volume regime, if the minor diameter of a toroidal microcavity becomes smaller, the mode volume of the toroidal microcavity becomes smaller until it reaches its minimum value. Figure 3.9 shows the calculated mode volume V of the fundamental $(q, l) = (0, 0)$ mode of the toroidal microcavity for small

[9] For the same Q-factor, circulating intensity inside the cavity is inversely proportional to the cavity mode volume, $I_{cav} \propto 1/V$, see section 2.1.3.

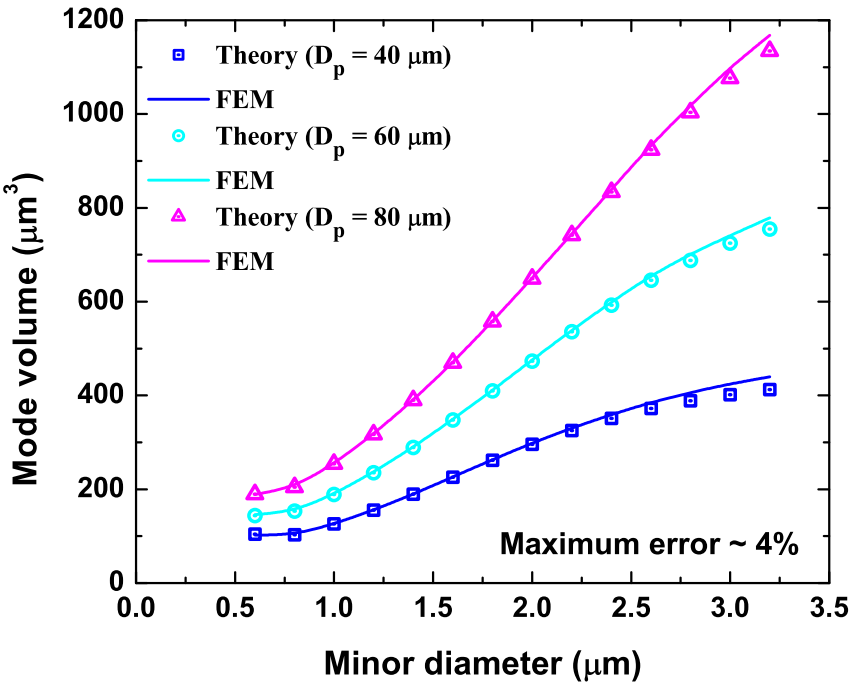

Figure 3.9: Calculated mode volume V of a fundamental $(q, l) = (0, 0)$ mode of the toroidal microcavity for small inverse aspect ratio.

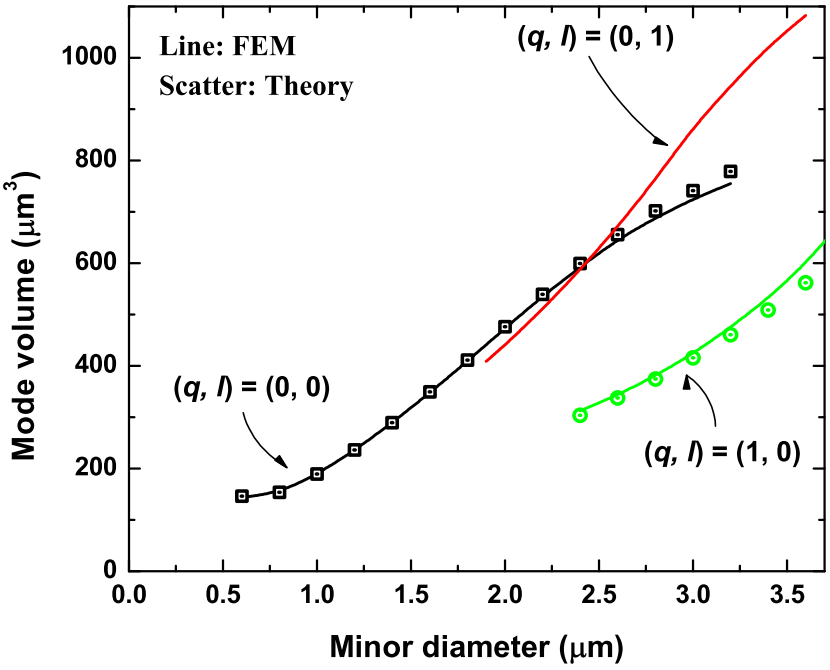

Figure 3.10: Mode volume of higher order modes calculated from the finite element method and the semianalytic calculations.

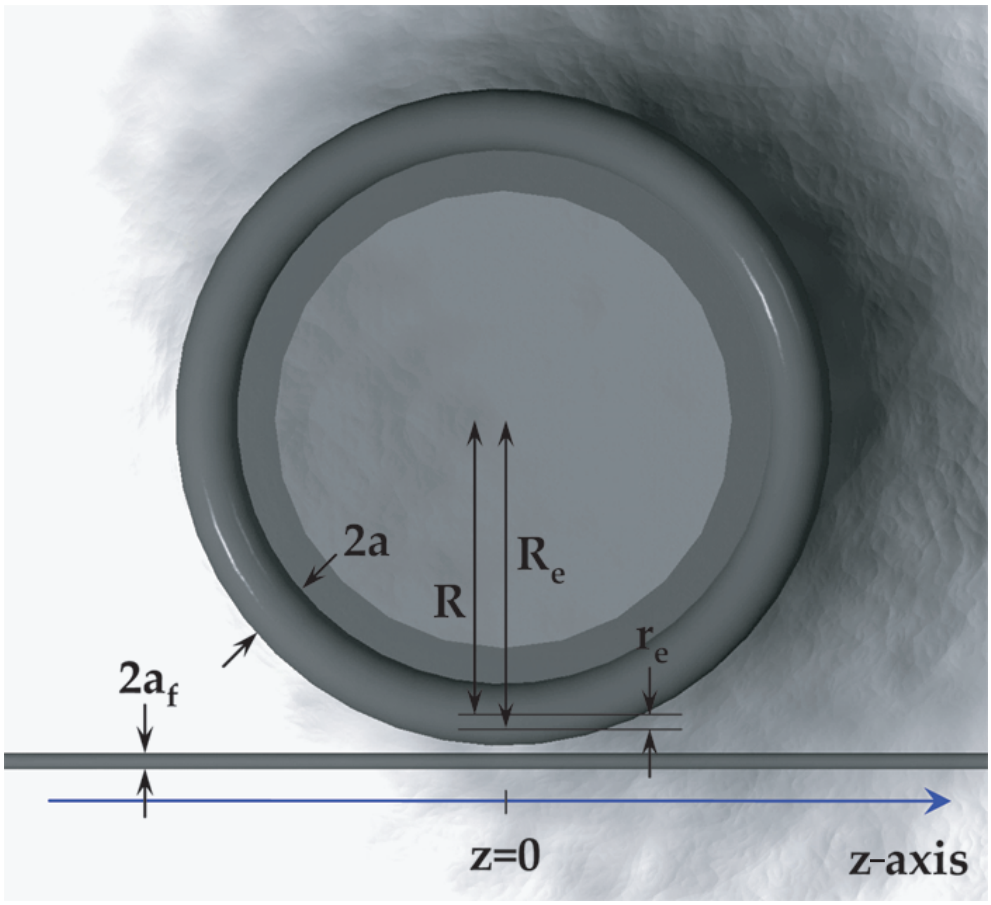

Figure 3.11: Relative geometry and parameters of toroidal microcavity and tapered fiber used to derive a phase-matching condition.

inverse aspect ratio. The applicability of the iterative perturbation expansion is limited to the fiber-like and the early transition regime as can be seen in Figure 3.9. Figure 3.10 shows the mode volume of higher order modes calculated from the finite element method and the semianalytic calculations. For a fixed aspect ratio, it is found that higher order modes can have a smaller mode volume mode than the fundamental mode especially for a slightly larger toroidal microcavity. However, the cutoff inverse aspect ratio for higher order modes is always larger than that for a fundamental mode and it is the fundamental mode that has a global minimum in the mode volume.

3.2.4 Phase-matching conditions

Phase-matching between the cavity mode and the waveguide mode is a necessary condition that permits us to effectively couple waves into and out of the microcavity resonators.

To access all three regimes of coupling (undercoupled, overcoupled, and critically-coupled regime) with a variation in gap width between the waveguide and the microcavity, phase-matching is essential (in addition to high enough intrinsic Q-factors of the cavity). From an intuitive point of view, a simple phase-matching criterion can be written as,

$$\beta_e = \beta_{taper}. \tag{3.26}$$

Phase-mismatching (i.e., the difference in propagation constants, $\Delta\beta$), however, is present even for the toroidal microcavity and the tapered fiber with the same propagation constants and this is caused by the curved geometry of the cavity. To transform the propagation constant β_e in the curved geometry into the equivalent propagation constant $\beta_{e,tr}$ in straight waveguide coordinates (as seen by the straight tapered fiber), the following mapping formula can be used [46]:

$$\beta_{e,tr} \simeq \left[1 - \frac{d_{sep}}{2R_e} - \left(\frac{z}{2R_e}\right)^2\right]\beta_e, \tag{3.27}$$

where β_e is the modified propagation constant obtained by the iterative method. At the minimum separation between the toroidal microcavity and the tapered fiber, i.e., $z = 0$, the effective propagation constant projected onto the axis of straight tapered fiber can be written (assuming $d_{sep} = a - r_e + a_f$, where a_f denotes the tapered fiber radius) as follows:

$$\beta_{e,tr}(z=0) \simeq \left(1 - \frac{a - r_e + a_f}{2R_e}\right)\beta_e. \tag{3.28}$$

To get a phase-matching condition, the propagation constant β_{taper} of the tapered fiber mode HE_{11} should be solved as a function of the tapered fiber radius a_f using the following characteristic equation [47]:

$$\frac{J_0(u_f)}{u_f J_1(u_f)} = -\left(\frac{n_f^2 + n_0^2}{2n_f^2}\right)\frac{K_1'(w_f)}{w_f K_1(w_f)} + \left(\frac{1}{u_f^2} - R\right), \tag{3.29}$$

where

$$R = \left[\left(\frac{n_f^2 - n_0^2}{2n_f^2}\right)^2\left(\frac{K_1'(w_f)}{w_f K_1(w_f)}\right)^2 + \left(\frac{\beta_{taper}}{n_f k}\right)^2\left(\frac{1}{w_f^2} + \frac{1}{u_f^2}\right)^2\right]^{1/2}, \tag{3.30}$$

$$u_f = a_f\sqrt{(n_f k)^2 - \beta_{taper}^2}, \qquad w_f = a_f\sqrt{\beta_{taper}^2 - (n_0 k)^2}, \tag{3.31}$$

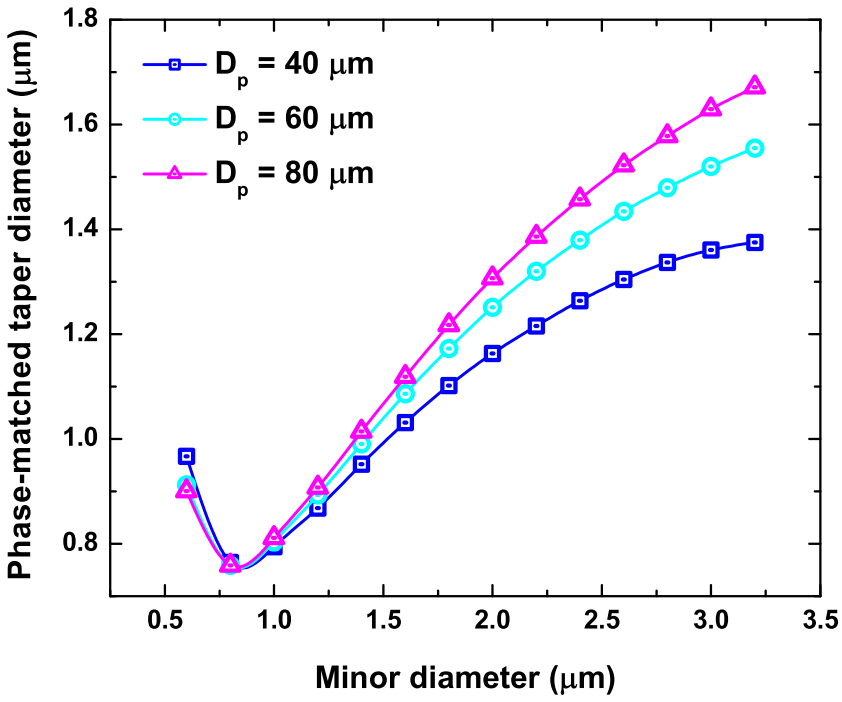

Figure 3.12: Phase-matched tapered fiber diameter as a function of the minor diameter for toroidal microcavities with 40, 60 and 80 μm principal diameter.

where n_f denotes the refractive index of the tapered fiber and n_0 is the refractive index of the surrounding. The following transcendental equation should then be solved for a phase-matched diameter of the tapered fiber:

$$\beta_{taper}(a_f) = \left(1 - \frac{a - r_e + a_f}{2R_e}\right)\beta_e(a). \tag{3.32}$$

Figure 3.12 shows the phase-matched tapered waveguide diameter as a function of the minor diameter for fixed toroidal microcavity principal diameters of 40, 60, and 80 μm. For a very small minor diameter ($d < 0.8$ μm), the phase-matched tapered waveguide diameter decreases as the minor diameter of the toroidal microcavity becomes larger. In this regime, the decrease of the phase-matched diameter is mainly caused by the decrease of the effective radial coordinate r_e. For a slightly larger minor diameters, the phase-matched tapered fiber diameter increases as the minor diameter becomes larger. This increase of phase-matched

diameter becomes slow due to the slow increase of β_e for larger minor diameters. In addition, it can be clearly seen that the phase-matched fiber diameter increases for larger principal diameter toroidal microcavity for a fixed minor diameter. However, it should be noted that, for a larger tapered fiber diameter, higher order tapered fiber modes can be present and the ideality of coupled cavity-taper system can be degraded.

3.2.5 Radiative Q-factors

The loss of a surface-tension-induced optical cavity consists of several mechanisms, and the total Q-factor of a toroidal microcavity resonator is determined by the combination of these loss mechanisms. Among these, the whispering-gallery loss (or the radiative loss), which is induced by the curvature of open dielectric cavity, can be a dominating factor especially for small toroidal microcavities.[10] In this section, the radiation loss of toroidal microcavity resonators will be computed using the "volume current method" (VCM). In this approach, the polarization current density created by the electric field inside the dielectric microcavity (given by $\vec{J}(r,\phi,\theta) = \epsilon_0\omega\Delta\epsilon\vec{E}(r,\phi,\theta)$) acts as a polarization current source, and this induces a far field (vector potential $\vec{A}$) by a scalar Green's function. By calculating Poynting vector $\vec{S}$ from this vector potential, the radiation loss can be calculated. A similar problem, the radiation loss calculation of a bent optical fiber, has been tackled in many papers [42, 48]. One of these, an approach given by Kuznetsov and Haus [42], can be modified to fit our current toroidal microcavity geometry. The same approach has also already been shown to be applicable to the case of microsphere resonators [34]. The radiative Q-factor of a toroidal microcavity now can be formulated as,[11]

$$Q_{rad} \simeq \frac{\pi n^2 R_e}{\lambda Z_0 \int S_{r'} r'^2 \sin\theta' d\theta'}, \tag{3.33}$$

where Z_0 denotes the impedance of the free-space ($Z_0 \simeq 377$), R_e is the effective radius defined previously, and $S_{r'}$ is the magnitude of the Poynting vector in the radial direction

[10] For a spherical microcavity, the only dimension of interest is the diameter. However, the situation is slightly different for a toroidal microcavity. Additional compressions in the polar/radial direction increase radiative loss when compared to the spherical microcavity especially for small inverse aspect ratio δ.

[11] In this approximation, electric field polarization is assumed to be normal to the equatorial plane. This approximation is intuitively justified expecially for the fundamental mode, which has a higher field density concentrated near the equatorial plane, $\phi \ll 1$. For more accurate calculation, the term related to a norm of the vector product, $|\hat{r'} \times \hat{\phi}|$, should be included into the equation (3.33) making the expression rather complex.

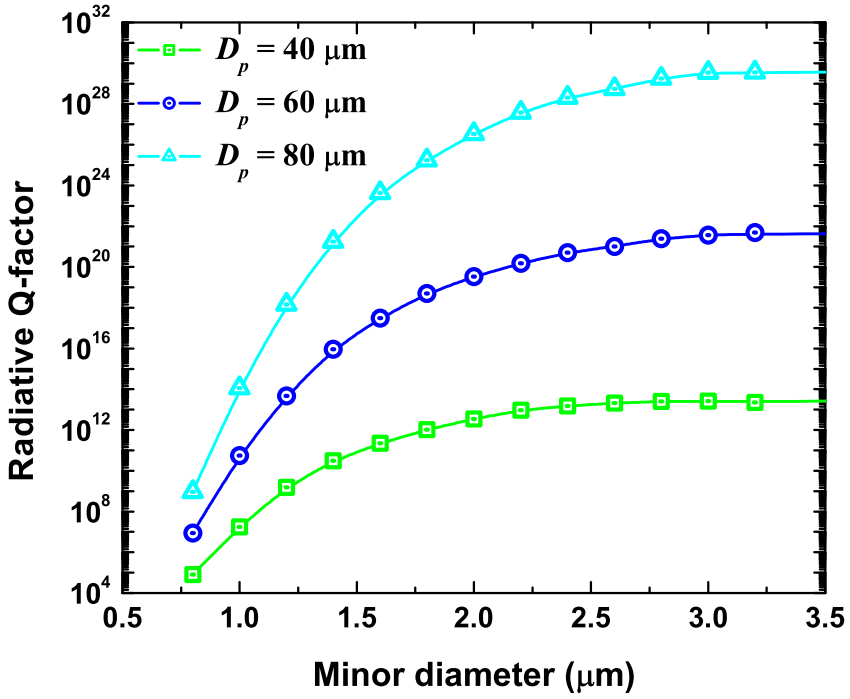

Figure 3.13: Radiative Q-factor for fundamental TE modes of toroidal microcavities with principal diameters of 40, 60, and 80 μm. The resonance wavelengths were chosen to be near 1550 nm.

of the spherical polar coordinates used to describe the far field.[12] Figure 3.13 shows the calculated radiative Q-factor for fundamental TE modes as a function of the minor diameter of toroidal microcavities with principal diameters of 40, 60 and 80 μm. The resonance wavelengths were chosen to be located near 1550 nm. As can be confirmed from Figure 3.13, the whispering-gallery loss is a sensitive function of the minor diameter. As the size of minor diameter decreases, the radiative Q-factor decreases very quickly in the regime of small inverse aspect ratio due to the additional leakage of confined modes, which is induced by the increased compression in toroidal boundary.

[12]Primes are used for the spherical polar coordinates.

3.3 Conclusions

Semianalytic approaches utilizing an iterative method and a perturbation expansion have been proven to be a valuable approximation to a toroidal microcavity characterization. The proposed analysis method is in excellent agreement with the finite element simulation and promises a further expansion possibility for a useful characterization for the toroidal microcavity with small inverse aspect ratio. Although the solutions given in this thesis are not fully analytic, an asymptotic expansion or other approximate methods may be able to give a simpler analytic formula.

Chapter 4

Nanocrystal Quantum Dot Microcavity Lasers

Semiconductor nanocrystal quantum dots are versatile building blocks that promise diverse applications ranging from biological tagging materials, solar cells, and field-effect transistors to light-emitting diodes [49–53]. Their discrete density of states and enhanced oscillator strength can also be used to realize ultra-low threshold quantum dot lasers [54–61]. In this chapter, we demonstrate an ultralow threshold on-chip tapered fiber coupled toroidal microcavity nanocrystal quantum dot laser with a threshold pump energy below 10 fJ at room temperature, a factor of 1 million lower than previously reported for strongly-confined, nanocrystal quantum dot lasers [58].

Reduction of laser threshold can be obtained by leveraging large oscillator strength gain media with high-quality-factor (Q-factor)/high-spatial-confinement resonator designs. Along these lines, two, emerging strategies have been pursued and verified as a means to explore the limits of classical laser performance. In the first, small mode volume (high spatial confinement) photonic crystal microcavities offering moderate Q-factors are loaded with epitaxially-grown, self-assembled semiconductor quantum dots (InAs/GaAs QDs) with impressive results (lasing threshold power of 160 nW at 4.5 K) [62]. In the latter, dielectric microsphere resonators capable of high-Q performance with moderate spatial confinement have been coated with strongly-quantum-confined, semiconductor colloidal dots (CdSe/ZnS (core/shell) nanocrystals) to also achieve excellent performance (lasing threshold power of 12 μW at room temperature) [58].

As a chip-based microcavity providing Q-factors in excess of 100 million, silica toroidal microcavity resonators provide both long photon storage times and improved spatial con-

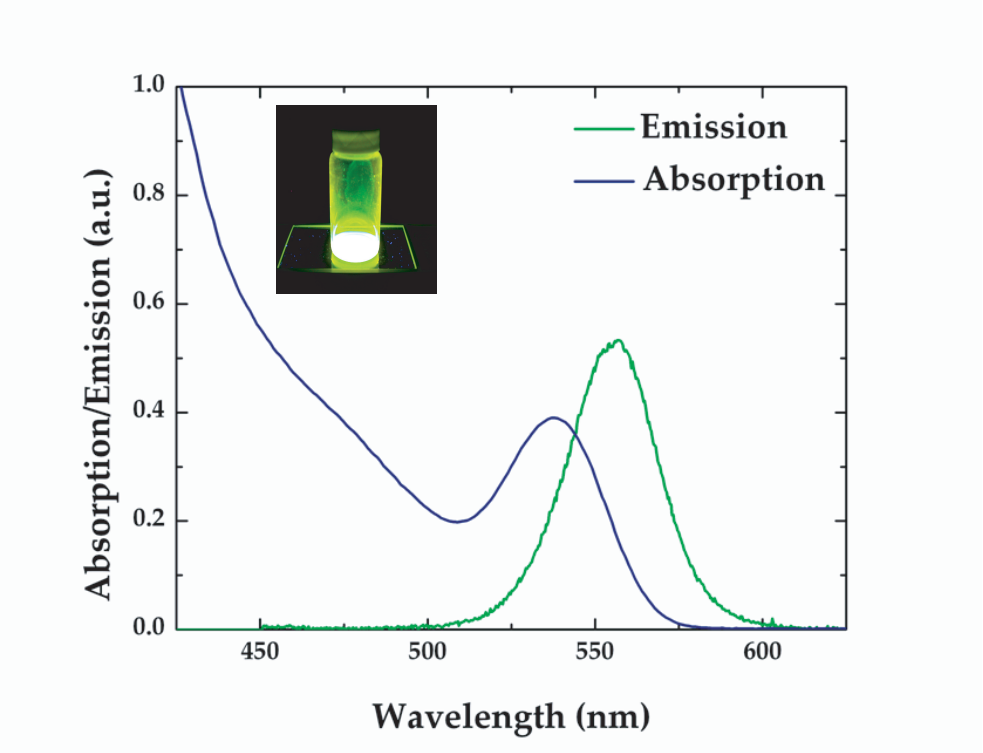

Figure 4.1: Absorption and photoluminescence spectra of QDs in hexane solution are shown. Inset: QDs in toluene excited by UV lamp.

finement over microsphere resonators of comparable size [23]. The devices are also fabricated at lithographically predefined locations on a silicon chip which provides additional benefits over microsphere resonators. Furthermore, with highly-ideal, tapered-fiber coupling, efficient pumping and laser emission extraction is possible with low insertion loss [25, 26].

4.1 CdSe/ZnS (core/shell) nanocrystal quantum dots

CdSe/ZnS (core/shell) nanocrystals having a high photoluminescence (PL) quantum yield (>50%) are similarly synthesized by the organometallic method as published [63,64]. Monodisperse QDs are produced generally within 5% size distribution. Figure 4.1 shows the typical absorption and photoluminescence (PL) spectra measured by a spectrophotometer and a CCD spectrometer (PL is measured while CdSe/ZnS QDs in hexane are excited by a GaN laser). In the subsequent characterization and experiments, CdSe/ZnS (core/shell) QDs with peak wavelengths in the range of 560-570 nm are used. Typical PL emission from the QDs has a Gaussian width of 29-33 nm. Inset in Figure 4.1 shows the image of QDs (in

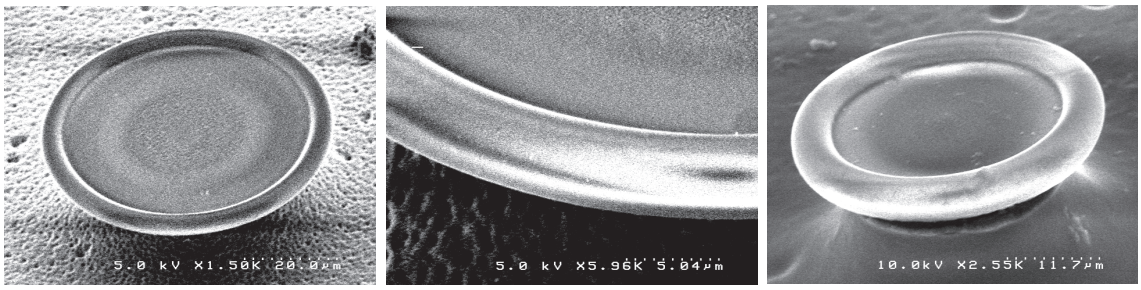

Figure 4.2: Scanning Electron Microscope (SEM) images of the QD coated toroidal microcavities. Left: QD solution-coated, center: enlarged view, right: QD sol-gel coated.

hexane) under UV lamp excitation.

4.2 CW excitation of QD coated toroidal microcavity

Ultrahigh-Q silica toroidal microcavities and tapered fiber waveguides are fabricated by the procedures published earlier [23]. For the subsequent experiments, multimode graded index fiber (NA = 0.27) with the core size of 62.5 μm is used to make a tapered fiber. The waist diameter of the tapered fiber center is adiabatically reduced down to around 1 μm allowing pump pulses to be coupled evanescently to the toroidal microcavity. The QDs are dispersed in toluene or hexane and spincast on toroidal microcavities. Thin, densely-packed QD films are generally formed on the surfaces of the toroidal microcavities. The thickness can be tuned down to a QD monolayer by controlling the spincasting condition and the concentration of QD solutions. Typical QD thicknesses explored in this work were a few densely-packed layers down to a QD monolayer with $\sim$0.3% volume fraction. Volume fraction was estimated from spectrophotometric measurements of the solutions that have retrieved QDs from the spun-cast wafer surfaces by using a known QD absorption cross section [65]. Estimated QD numbers in the active region of the toroidal microcavity is then calculated by assuming homogeneous QD coating on the toroidal microcavity. Figure 4.2 shows scanning electron microscope (SEM) images of the QD coated toroidal microcavities. As can be seen in the first two images (in Figure 4.2), it is not possible to see any defects or aggregations induced by spin-coating process within the resolution limit of SEM.

Continuous wave excitation of QD coated toroidal microcavity via a tapered fiber has been performed and the typical output spectra are shown in Figure 4.3. Whispering-gallery

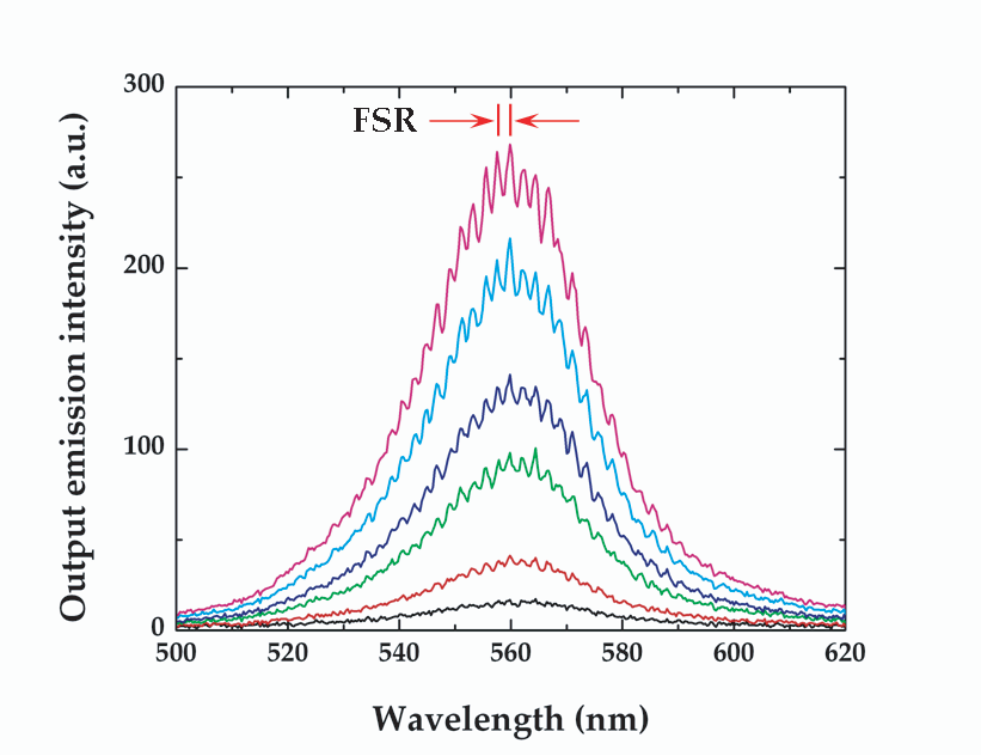

Figure 4.3: CW excitation of QD coated toroidal microcavity. whispering-gallery modes can be identified.

modes can be identified with a corresponding FSR relevant to the size of the toroidal microcavity used in the experiment. Due to photo-bleaching (photo-oxidation) effect, PL from the QDs gradually decreased with a time scale from tens of seconds to tens of minutes depending on the pump power. Figure 4.4 shows the output emission spectra taken at 4 minutes interval. The intensity decrease and the peak emission blueshift confirm the photo-oxidation effects and corresponding QD size reductions that have been verified by several references [66,67]. The output power from the QD coated toroidal microcavity as a function of input pump power shows no threshold behavior within the available power limit of the pump laser (<50 mW before being coupled to the tapered fiber). The absence of threshold behavior can be attributed to the high probability of charged QDs with CW excitation.[1]

[1]The origin of charging or ionization of QDs is not clearly proven yet. Carrier tunneling and Auger autoionization are proposed as possible QD ionization mechanisms in [68, 69].

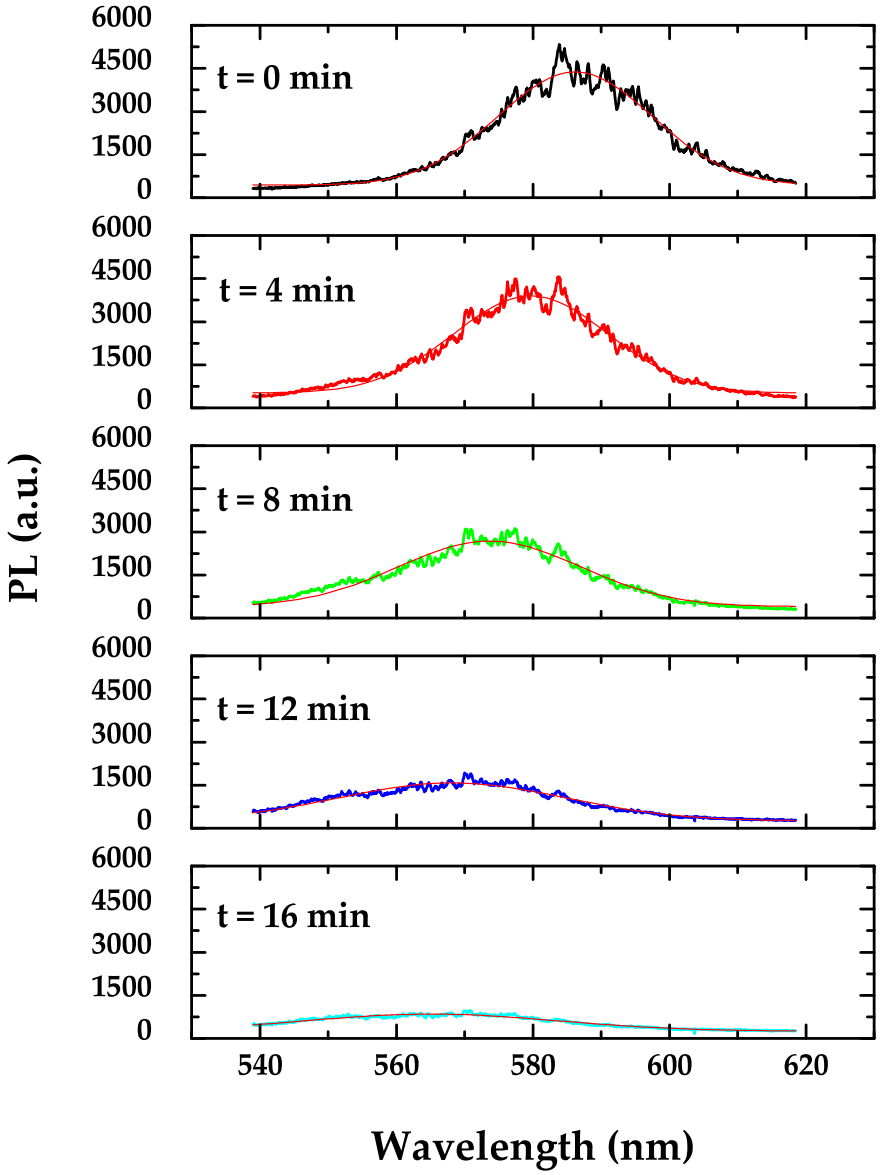

Figure 4.4: PL from the QD coated toroidal microcavity as a function of elapsed time (4 minutes interval). Lines are Gaussian fittings to the observed PL.

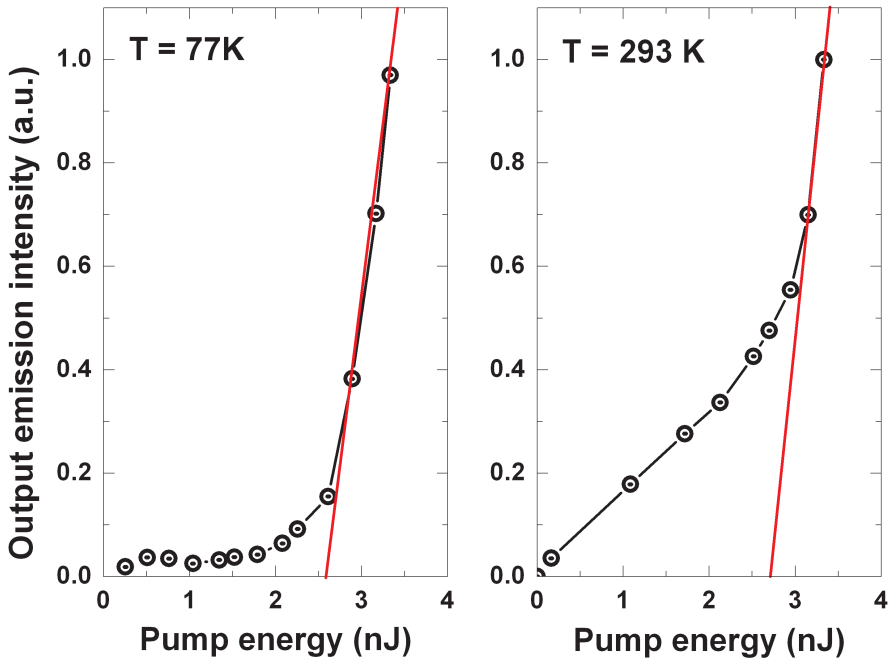

Figure 4.5: Normalized output emission power as a function of input pulse energy at two different temperatures. Left: liquid nitrogen temperature, right: room temperature.

4.3 Pulsed excitation of QD coated toroidal microcavity

Pulsed excitation is used for all subsequent experiments to avoid Auger-induced or tunneling-induced ionization of QDs [68, 69] as explained in the previous section. In addition, pulsed excitation is prefered for the stimulated emission to compete with nonradiative multiexciton Auger recombination [70] in the strongly-confined regime. The excitation pulse is frequency doubled from the fundamental of a mode-locked Ti:sapphire femtosecond laser having a pulse width of <100 fs (for the fundamental) and a repetition rate of 80 MHz. Output emission is collected by a streak camera or a liquid nitrogen-cooled CCD spectrometer.

4.3.1 Free-space excitation

Measurements at two different temperatures are conducted to investigate temperature-dependent characteristics of QD coated toroidal microcavity lasers. For a low temperature measurement, QD coated toroidal microcavity is held at the liquid nitrogen temperature using a cold finger cryostat. Room temperature experiment is performed under ambient

environment. Figure 4.5 shows typical data for the output emission power as a function of free-space pump excitation energy (L-L curve) at liquid nitrogen and room temperature. Threshold pump energy of ∼2.6 nJ has been achieved for a QD cast toroidal microcavity at liquid nitrogen temperature. The lasing emission is collected by a streak camera. It is worthwhile to note that the threshold energies are not very sensitive to the temperature change [70]. This is characteristic of QDs in strong confinement regime and is in contrast to other epitaxially grown large QDs.

4.3.2 Tapered fiber coupled excitation

Figure 4.6 shows the schematic experimental set up for a tapered fiber coupled excitation of the QD cast toroidal microcavity lasers. Inset shows a optical microscopy image of a representative QD cast toroidal microcavity with a minor/principal diameter of 5/60.6 μm under tapered fiber pulsed excitation. The lasing emission is bi-directionally coupled out of the cavity (inset) and measured at one end of the tapered fiber either by a streak camera with time resolution of 20 ps or by a liquid nitrogen cooled CCD spectrometer. From the optical micrograph, it can be confirmed that the whispering-gallery modes (residing in the periphery of the toroidal microcavity) are selectively excited by the use of tapered fiber coupling. Figure 4.7 shows actual experimental setup used in the tapered fiber excitation of QD cast toroidal microcavities.

To understand the loading conditions affecting pump and signal coupling, we studied the effect of QD surface coverage (i.e., volume fraction) on the total intrinsic Q-factor of the toroidal microcavity. The intrinsic Q-factor will be affected primarily by QD absorption at a particular wavelength as well as scattering caused by the discrete nature of the QDs as dielectric nanoparticles ($Q_0^{-1} = Q_{abs}^{-1} + Q_{scatter}^{-1}$). Figure 4.8 shows the theoretical intrinsic Q-factors (based on measured absorption and scattering parameters) for two differentT densities. The QD absorption-limited Q-factor can be calculated once the mode intensity profile is known with the physical dimension of the toroidal microcavity. The Q-factor in the absence of QDs is assumed to be in excess of 100 million (The adsorbed water molecules or OH^- on the surface have a negligible effect on Q-factor at the visible wavelength [2]). At wavelengths well above the absorption band of the QDs, the Q-factor is QD scattering limited as illustrated ($Q_{scatter}^{-1} \propto \lambda^{-7/2}$). However, at the pump wavelength the Q-factor is

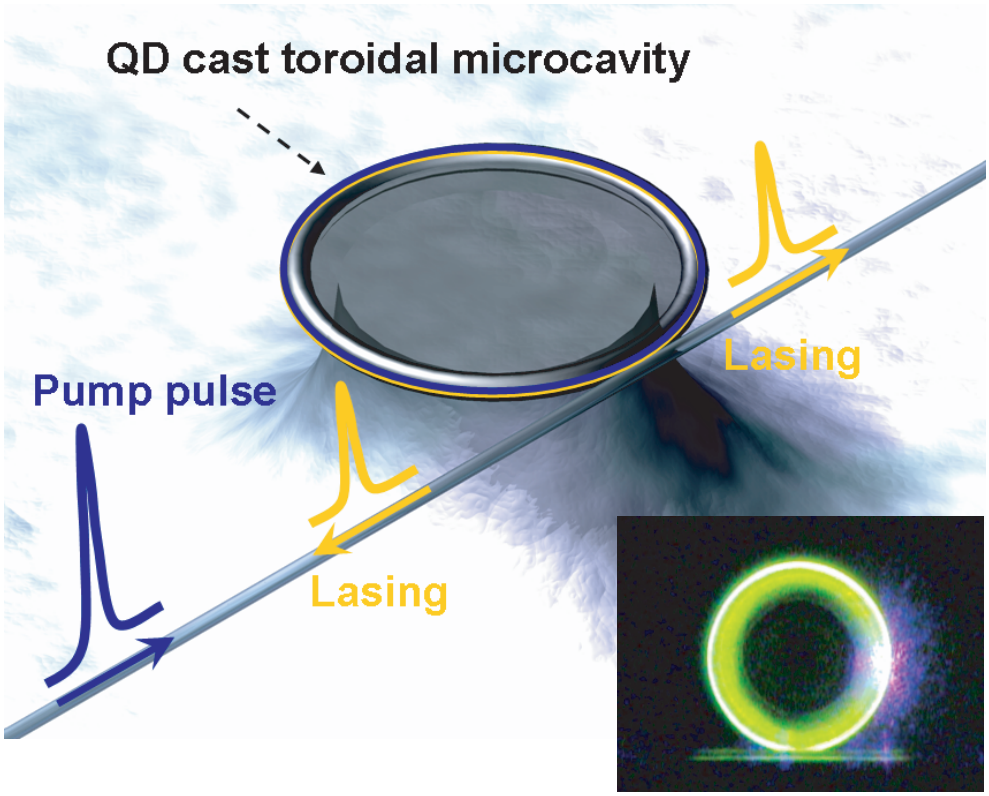

Figure 4.6: Schematic experimental setup of a tapered-fiber-coupled, toroidal-microcavity, nanocrystal QD laser. Pump pulses are coupled to the microcavity and lasing pulses are bidirectionally emitted through the tapered fiber. Pulse repetition rate is 80 MHz and pump wavelength is 388 nm. The output emission is collected either by a streak camera or by a high-resolution, liquid-nitrogen-cooled, CCD spectrometer. Inset: optical micrograph of QD cast toroidal microcavity laser.

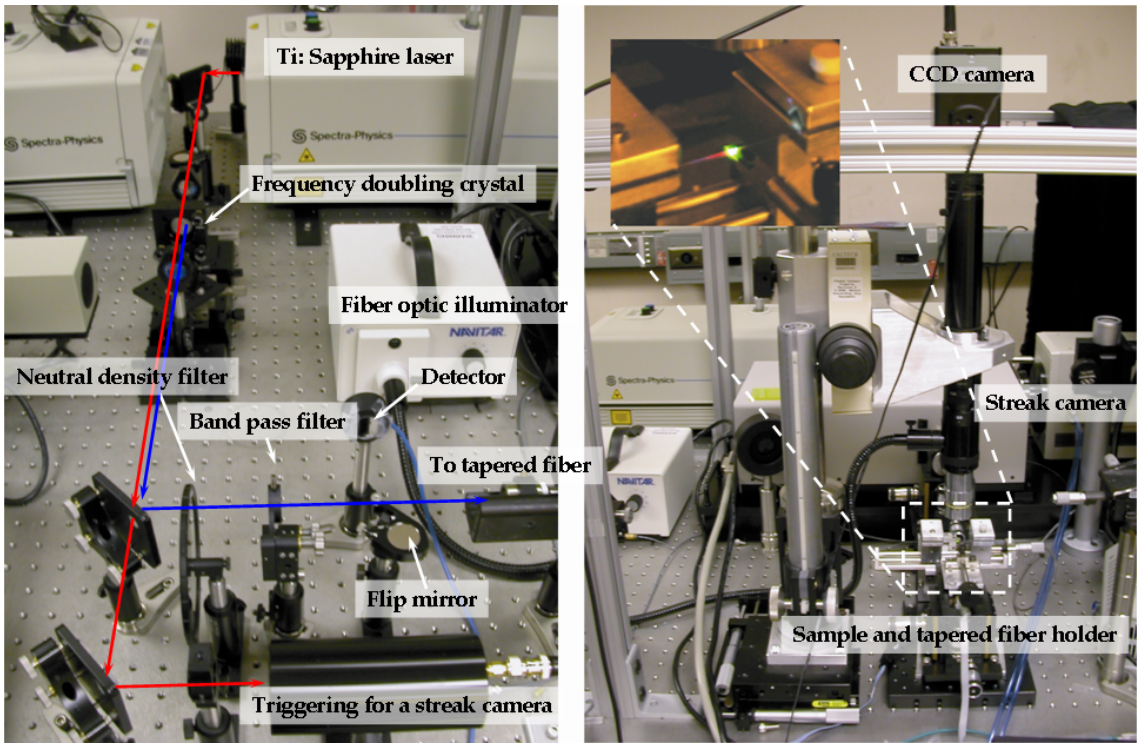

Figure 4.7: Experimental setup for tapered fiber excitation of a QD coated toroidal microcavity. Inset: image taken by a digital camera while the sample is excited via the tapered fiber coupling.

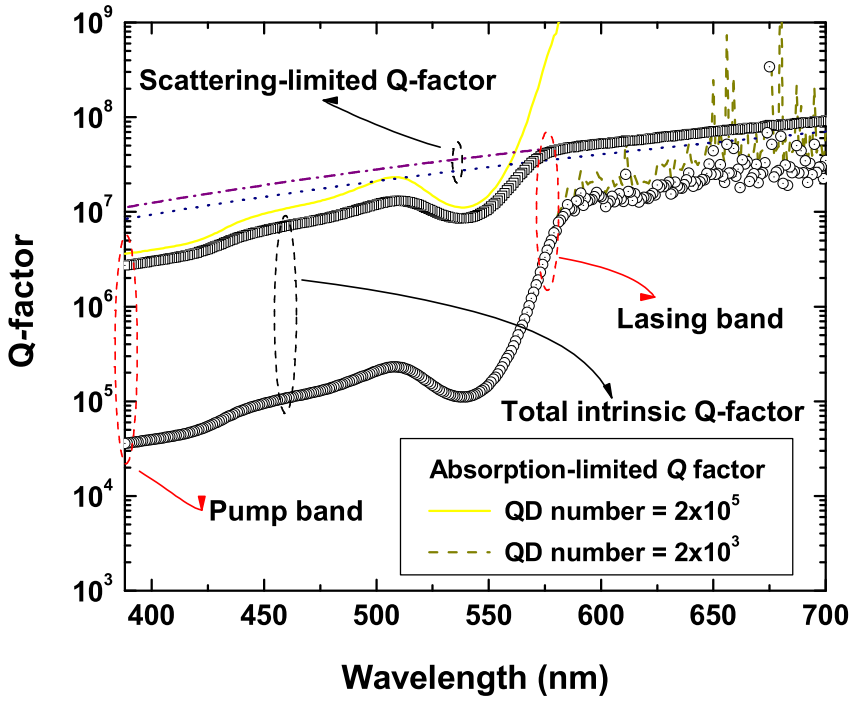

Figure 4.8: Theoretical total intrinsic Q-factors for two different surface coverages of QDs on a toroidal microcavity (circle/rectangle : high/low coverage). QD scattering-limited Q-factors (dot/dash-dot : high/low coverage) and absorption-limited Q-factors (solid/dash : high/low coverage) are also shown.

absorption limited and estimated to be in the range from 2×10^4 to 3×10^6 depending on the coverage density. The following equation is used to estimate the QD absorption-related Q-factors:

$$Q_{abs} = \frac{2\pi n_{ref}}{\lambda \sigma_{QD}(\lambda)} \frac{\int_0^{2\pi}\int_0^{\infty} I(r,\phi) r dr d\phi}{\int_0^{2\pi}\int_0^{\infty} I(r,\phi) n(r,\phi) r dr d\phi}, \tag{4.1}$$

where $\sigma_{QD}(\lambda)$, $n(r,\phi)$, and $I(r,\phi)$ are QD absorption cross section [65], QD concentration, and normalized mode intensity pattern of the toroidal microcavity, respectively. The measured intrinsic Q-factor at 682 nm is 1.2×10^7 for low coverage density (0.3% volume fraction). Optimal pump coupling resulted when tapered fiber and toroidal microcavity were in contact. This arrangement indicates the presence of strong pump-band absorption provided by the QDs. Furthermore, the absorption-limited pump-band Q-factor is so low so as to enable efficient coupling of even short pulses, which themselves are spectrally broad

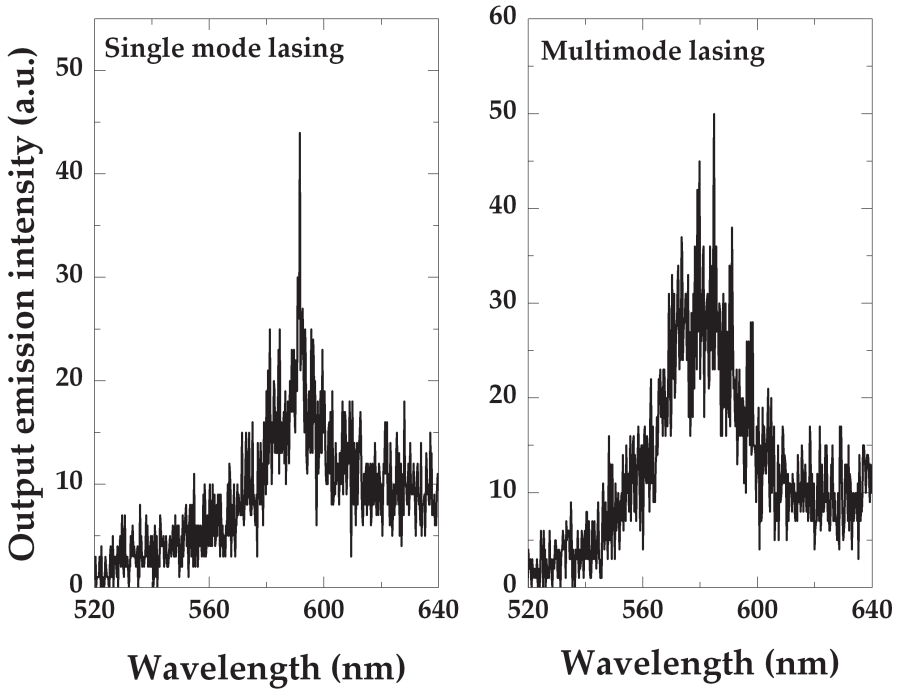

Figure 4.9: Single mode and multimode lasing spectra from tapered fiber coupled torodial microcavity QD lasers. Spectra are integrated over a time window of 50 ps after each pulse excitation. Left: Single mode lasing spectrum, right: Multimode lasing spectrum.

(for toroidal cavities used here, there exist many higher-order modes at the pump wavelength in addition to the fundamental pump mode and the presence of these modes with low Q-factors can result in an improved coupling). Depending on the sample, both single mode and multimode lasing have been observed. Representative single mode lasing is shown in Figure 4.9 (left) with the lasing peak at 579 nm. Figure 4.9 (right) shows a multimode spectrum. The streak camera image of the output emission corresponding to a multimode lasing is shown in Figure 4.10. The measured mode spacing of approximately 5 nm is larger than the next-nearest neighbor spacing ($\sim$1 nm) and is consistent with spectral hole burning in the gain distribution [71]. The mechanisms responsible for single mode versus multimode oscillation in this system are still under investigation. The lasing spectra are obtained by integrating 50 ps windows after each excitation pulse. Through control experiments, the broad background emission (>600 nm) originates from the defects within the silica fibers (Figure 4.11) and those defects are believed to result from the tapering (heating) process by hydrogen flame. As can be seen from Figure 4.11, tapered fiber emission peak is located at

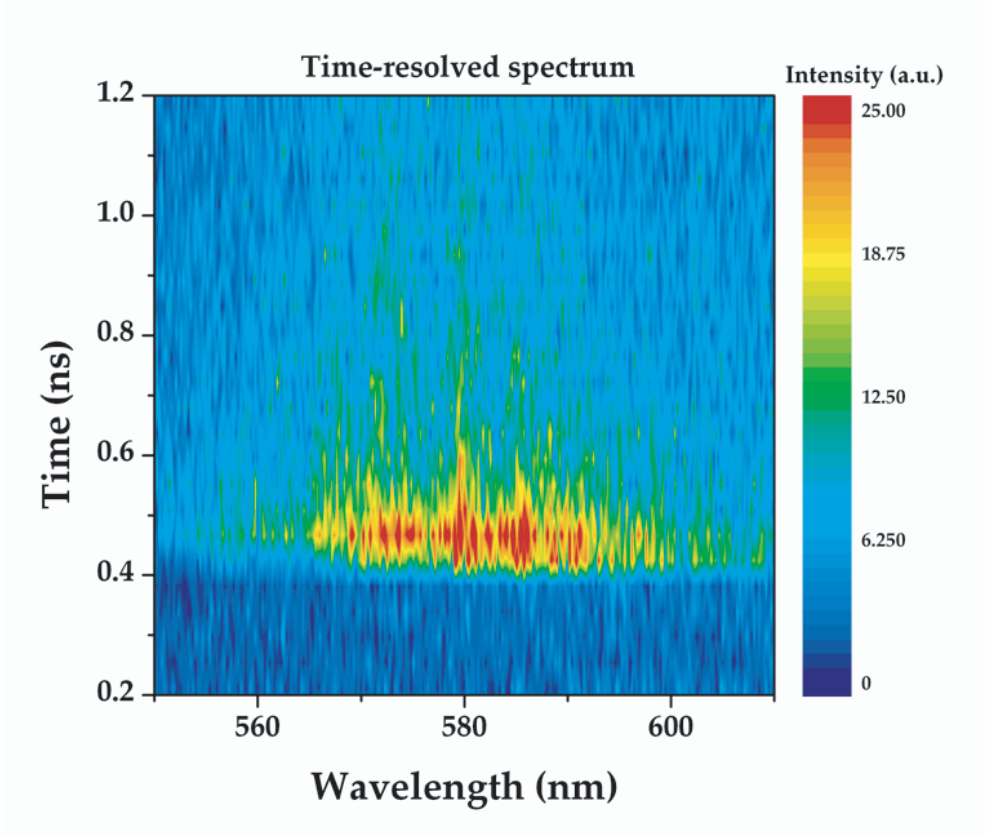

Figure 4.10: Streak camera image of output emission intensity corresponding to a multimode lasing case in Figure 4.9.

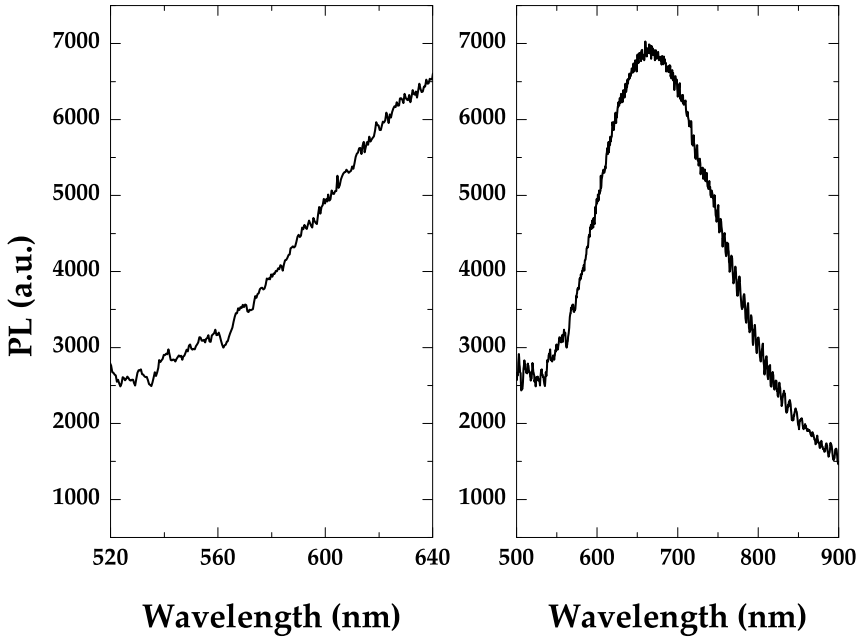

Figure 4.11: Tapered fiber emission without QD coated toroidal microcavity. Strong photoluminescence is observed under pulsed excitation.

~650 nm. This tapered fiber emission adds a noise background to the measured lasing spectrum. For comparison to the free-space pumping case, Figure 4.12 (a) shows an LL curve measured using a tapered-fiber coupled QD laser at room temperature with other conditions kept identical to the free-space pumping experiment. Decay lifetime is recorded at various pump energies along with processed CCD images of the QD cast toroidal microcavity lasers (Figure 4.13). The processed CCD images illustrate the actual whispering-gallery mode traces in the toroidal microcavity and are more clearly shown for the case of low energy excitation due to the saturated response of the CCD pixels at higher pulse energy. As can be clearly seen in these decay curves, at even low pump energy of around 5.3 pJ (which is still above the threshold) the biexitonic decay can be identified showing the effectiveness of toroidal microcavity QD lasers. All the curves can be fitted with two exponentials having definite lifetime of 3.7 ns and 70 ps each corresponding to an excitonic and a biexitonic lifetime. A threshold energy (~1 pJ, in the left panel) is measured (Figure 4.12 (a)), and this represents a reduction by a factor of ~2600 when compared to the free-space excitation

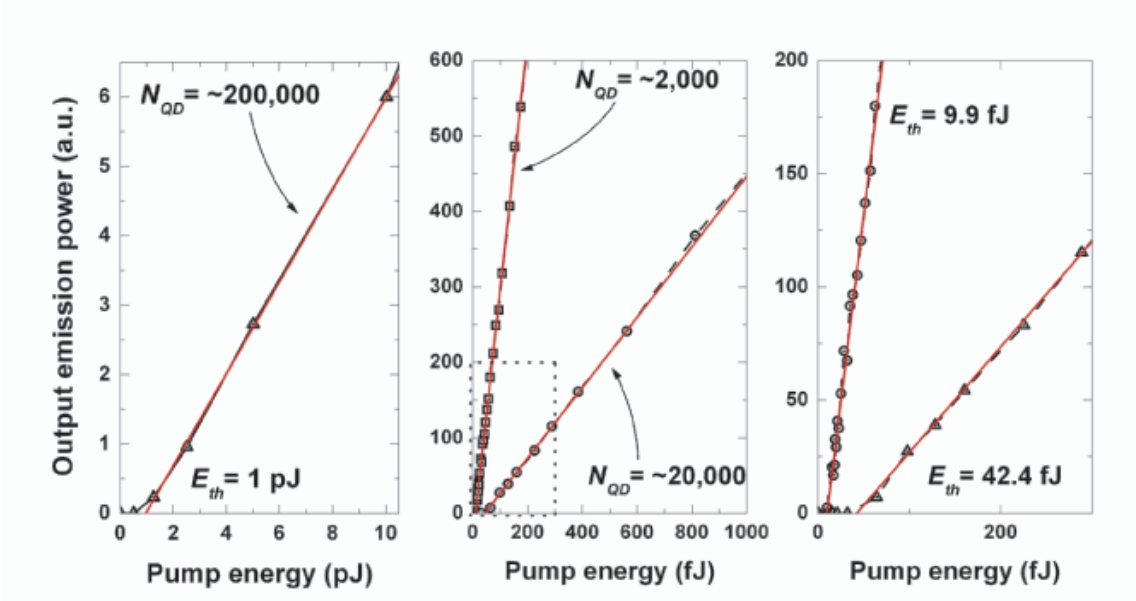

Figure 4.12: Output emission powers for three different QD concentration samples. (a) LL curve for a QD coated toroidal microcavity laser having $\sim 2 \times 10^5$ QDs in the active region. (b) LL curves for lower density QD toroidal microcavity lasers having $\sim 2 \times 10^4$ and $\sim 2 \times 10^3$ QDs in the active region. (c) Magnified graphs showing the area enclosed by doted line in Figure 4.12 (b)

case. This reduction of threshold energy can be explained by efficient and direct delivery of pump energy to the QD gain region as compared to the free-space excitation, in which case, pump pulse is not coupled efficiently to the toroidal microcavity. The following simple formula on the average number of excitons can be qualitatively used to describe foregoing arguments [72]:

$$\langle N_{ex} \rangle = \frac{\sigma \lambda}{hc} \frac{E_{pulse}}{A}, \tag{4.2}$$

where σ is the absorption cross section at the pump wavelength, λ is the pump wavelength, h is the Planck constant, c is the speed of light, E_{pulse} is the input pulse energy and A is the effective area of the excitation. For the case of free-space pumping, the effective area A is on the order of a few thousand μm^2 to excite the whole area of toroidal microcavity. However, the effective area is on the order of a few μm^2 with the tapered fiber coupling. Therefore, from equation (4.2), to generate the same number of excitons, orders of magnitude lower pump energy will be needed for a tapered fiber coupling than for a free-space pumping.

We next studied the effect of reducing the number of QDs in the active region of the toroidal microcavity on the threshold energy. By decreasing the number of QDs in the

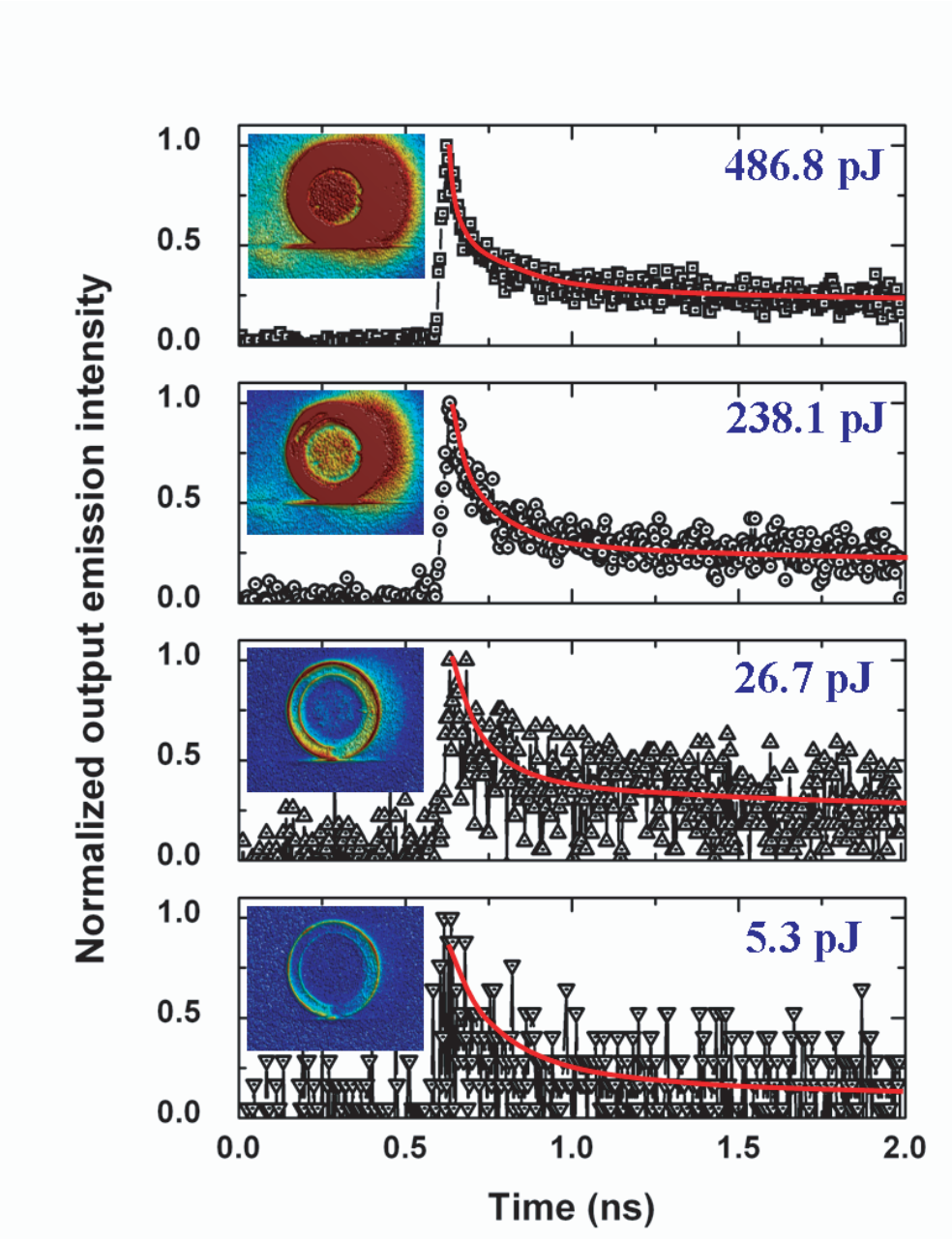

Figure 4.13: Time-resolved decay measured by a streak camera for a high density toroidal microcavity laser.

active gain region, two benefits can be obtained. First, the cavity Q-factor is increased by reducing QD-related contribution to scattering/absorption loss (Figure 4.8) and this in turn reduces the required optical gain to achieve threshold condition. Second, and most important, the transparency condition is lowered in proportion to the numeric reduction in QDs within the gain region. Concerning this latter effect, the threshold pump energy consists of a transparency component and a gain component. Optimization of threshold therefore requires a balance of these two components that can be achieved experimentally through variation of the QD number. Using a simple semiconductor laser theory, the threshold pumping rate can be expressed as follows:

$$R_{th} = \frac{1}{\tau_{QD}} \left(N_{QD} + \frac{1}{B\tau_p} \right). \tag{4.3}$$

The first term is related to the total concentration of QDs in the active gain region and the second term is inversely proportional to the cavity photon lifetime. With the assumption of relatively high Q-factor, the contribution from the second term is negligible in the high Q laser systems. Therefore, the lasing threshold will be approximately proportional to the QD numbers in the active gain region. To test this scaling rule for an optimum threshold, two other samples having a decreased number of QDs (Figure 4.12 (b) and (c)) were measured. Threshold pump energies of 42.4 fJ and 9.9 fJ are obtained respectively for ∼20000 and ∼2000 QDs within the active region. In Figure 4.14, the measured threshold pump energies are plotted as a function of the estimated number of QDs in the active region (volume fraction in the active gain region). For comparison, the theoretical lower bound on threshold energy provided by the transparency condition is also plotted.[2]

4.4 Conclusions

These observed improvements in laser threshold demonstrate the effectiveness of colloidal QDs as a tool to explore the limits of laser performance in the strongly confined regime, and, in addition, the utility of tapered fiber coupling to a high-Q toroidal microcavity. From a fundamental viewpoint, the measurement of 9.9 fJ is a record low threshold for

[2]This condition is given by the amount of input energy required to achieve the transparency condition, i.e., generating a single exciton in each QD when averaged.

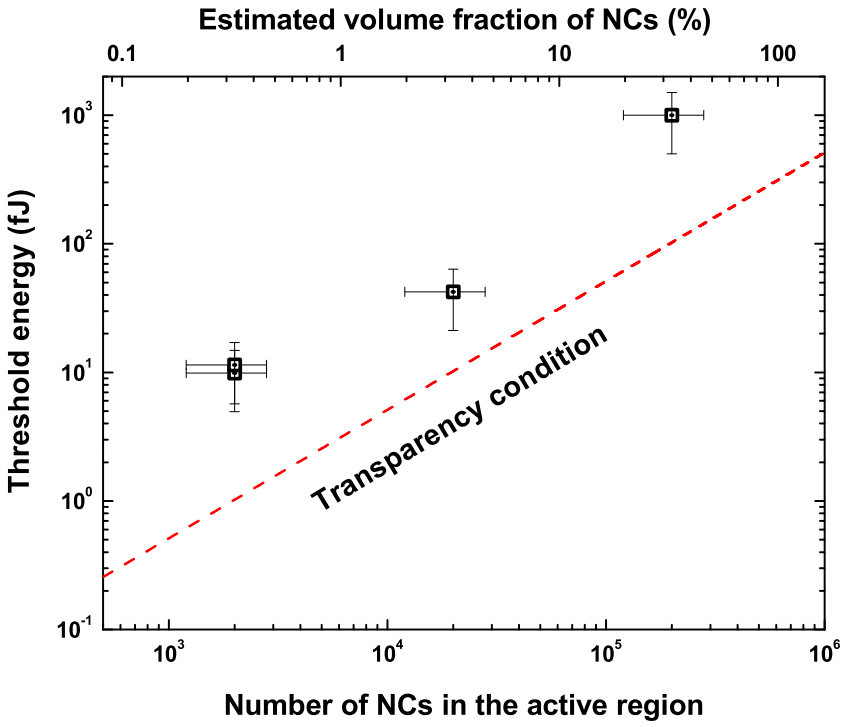

Figure 4.14: Threshold energy as a function of estimated number of QDs in the active gain region of the toroidal microcavity. Theoretical transparency condition is plotted along with experimentally measured threshold energies.

strongly-confined QDs and is close to the transparency bound for operation in this regime. Significantly, this result is obtained for room temperature operation, a result of using the strongly confined quantum dot lasing medium. Ultralow threshold pulse energy operation of these devices may create new avenues for optical switching technology where low pulse energy consumption is important. More generally, the ability to coat microresonators on a chip with semiconductor nanocrystals opens up use of other nanocrytal surface functionalizations for operation in the visible/infrared or potentially for sensing applications.

Chapter 5

Erbium-Implanted Toroidal Microcavity Lasers

Among the practical applications of ultrahigh-Q microresonators, rare-earth doped microcavity lasers have been successfully demonstrated in recent years. These include whispering-gallery-type microsphere lasers doped with neodymium, erbium and ytterbium-sensitized erbium [20–22, 73–77]. For the case of a neodymium-doped microsphere laser demonstrated by Sandoghdar et al. [20], the (absorbed) threshold power was as low as 200 nW. Using the chip-based toroidal microcavities, a novel sol-gel coating technique was applied recently to fabricate erbium-doped toroidal microcavity lasers on a silicon chip [78]. In addition to the advantages in fabrication, these devices provide improved spectral performance as compared to microspheres owing to their reduced modal spectra [23, 78]. In particular, single mode operation was possible in these devices. As a complementary method of gain functionalization that is more compatible with standard VLSI processing, we have recently demonstrated erbium-implantation based toroidal microcavity lasers [79]. For both types of erbium-doped resonators (made by sol-gel processing or implantation), the internal dynamics and the dependence on cavity loading between the waveguide (tapered optical fiber) and the microcavity have not been thoroughly investigated. In this chapter, we used the ion implantation method to incorporate erbium ions into ultrahigh-Q toroidal microcavities and study in detail various lasing characteristics when these devices are coupled to a tapered optical fiber for excitation. In addition, experimental results are correlated with modeling of devices to understand the limits of performance as well as the basic lasing mechanisms. Using samples of varying sizes and erbium ion concentrations, the minimum threshold power was shown to be as low as 4.5 μW and the highest output power was

measured to be 39.4 μW. A maximum unidirectional slope efficiency of 5.5% was observed. Lasing wavelength control between adjacent whispering-gallery modes was demonstrated and explained by a cavity-loading-induced change in the upper state population of erbium ions. The remainder of this paper is organized as follows. In section 5.1, we present a detailed description of erbium-doped high-Q toroidal microcavity lasers using coupled-mode formalism. In section 5.2, we briefly illustrate the fabrication process used to create the erbium-implanted toroidal microcavities. In section 5.3, we investigate experimentally the performance of erbium-implanted toroidal microcavity lasers and compare these experimental results with the proposed analysis. Finally, in section 5.4, we conclude and discuss future research directions.

5.1 Analytic modeling

The analysis is based on the coupling-of-modes formalism for the resonator coupled to an external waveguide [16, 26, 30, 80, 81] with the addition of gain (or loss) terms from the excited erbium ions. Considering two resonant modes at the pump and (lasing) signal wavelengths in the microcavity along with the pump wave coupled into the resonator from the waveguide (Figure 5.1 shows the graphical rendering of the toroidal microcavity-tapered fiber system), the basic coupled equations of motion for the pump and signal field can be written as follows:

$$\frac{da_s}{dt} = -\frac{1}{2\tau_s}a_s + g_s a_s, \tag{5.1}$$

$$\frac{da_p}{dt} = -\frac{1}{2\tau_p}a_p - l_p a_p + j\kappa_p s_p, \tag{5.2}$$

where a_s, a_p are internal cavity fields at the signal and pump wavelengths ($|a_{s,p}|^2$ is normalized to the energy in the cavity; and counter-rotating field coupling induced by surface inhomogeneity is not included in this analysis), $\tau_{s,p}$ are cavity photon lifetimes at signal and pump wavelengths (which include passive cavity loss mechanisms such as surface scattering, absorption and waveguide coupling [2, 26, 82] but exclude the gain/loss caused by the erbium ions), g_s, l_p are intracavity gain (or loss) coefficients depending on the mode, κ_p is the amplitude coupling coefficient between the resonator and the waveguide pump wave (which is defined as $\sqrt{1/\tau_{e,p}}$ and can be controlled by changing the gap width between the

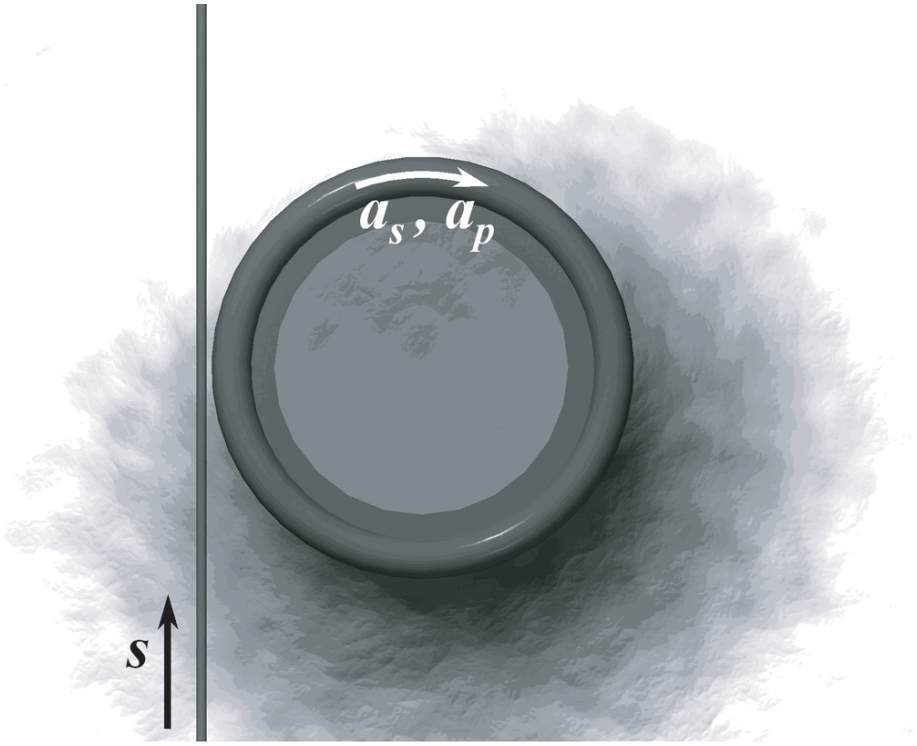

Figure 5.1: Graphical rendering of the toroidal microcavity-tapered optical fiber system. Input/output waveguide (tapered optical fiber) and erbium-doped toroidal microcavity are shown along with an input pump wave s_p and internal cavity fields a_p and a_s.

resonator and the waveguide), and s_p is the pump field amplitude in the input waveguide ($|s_p|^2$ is normalized to the pump power in the waveguide). For simplicity, we have used the slowly varying envelope approximation (SVEA). Competing effects such as cooperative up-conversion of erbium ions, excited-state absorption (pump or signal), pair-induced quenching [83–85] and the inclusion of spontaneous emission are not considered here. However, these effects can easily be incorporated analytically into the above basic equations by including appropriate additional rate terms and their associated rate equations. Mode splitting due to coupling of counter-rotating waves (induced by inhomogeneity of cavity surfaces) [37, 81] is not considered. Under steady-state conditions, the time derivative terms in (5.1) and (5.2) can be set to vanish, leading to the following two equations (5.3) and (5.4). The first equation is equivalent to the well-known threshold condition (i.e., cavity gain should be equal to cavity loss.[1]) for lasing and the second equation relates the internal cavity energy at the pump wavelength to the input pump power at the waveguide-resonator

[1]This is a classical definition of a threshold. For more recent elaboration on the definition of a laser, see [86].

junction:

$$g_s = \frac{1}{2\tau_s}, \tag{5.3}$$

$$|a_p|^2 = \frac{{\kappa_p}^2}{(\frac{1}{2\tau_p} + l_p)^2}|s_p|^2. \tag{5.4}$$

Even though these equations seem to be decoupled from each other, they are in fact coupled since the erbium upper state population N_2 determines both g_s and l_p as shown below (equations (5.5) and (5.6)). The intracavity gain and loss coefficients, g_s and l_p, can be expressed as,

$$g_s = \frac{c}{2n_s}\left[\frac{N_2}{N_T}(\alpha_s + g_s^*) - \alpha_s\right], \tag{5.5}$$

$$l_p = \frac{c}{2n_p}\left[-\frac{N_2}{N_T}(\alpha_p + g_p^*) + \alpha_p\right], \tag{5.6}$$

where c is the speed of light, n_s, n_p are the refractive indices at the signal and pump wavelengths, N_T is the average erbium ion concentration, and $\alpha_{s,p}$ and $g^*_{s,p}$ are Giles-parameters [83,84,87] originally introduced for the modeling of erbium-doped fiber amplifiers and defined as,

$$\alpha_{s,p} \equiv \Gamma_{s,p} N_T \sigma^a_{s,p}, \tag{5.7}$$

$$g^*_{s,p} \equiv \Gamma_{s,p} N_T \sigma^e_{s,p}. \tag{5.8}$$

In these expressions $\Gamma_{s,p}$ is an overlap factor (defined as the dimensionless spatial overlap integral between the normalized optical intensity distribution and the normalized erbium ion distribution) at signal and pump wavelengths and ${\sigma_{s,p}}^{a,e}$ is the absorption/emission cross section of erbium ions at signal and pump wavelengths. To fully utilize the simplicity of Giles-parameters as given by (5.7) and (5.8) for further discussion, it is necessary to specify the overlap factors in the toroidal microcavities. However, to date, there has not been a detailed analytic model for the field distribution in the dielectric toroidal resonators. In addition, the erbium ion diffusion process during the laser reflow process (see Armani et al. [23] and also section 5.3) is not well known. Therefore, throughout this chapter, the erbium ions will be assumed to diffuse homogeneously and the overlap factors of unity ($\Gamma_{s,p} = 1$) for both signal and pump wavelength will be assumed for the simplicity (on the assumption that the mode field distribution is well confined in the microcavity). We note

that the pump wavelength used is in the range 1460-1480 nm and therefore signal and pump overlap factors will be nearly the same.

5.1.1 Upper state population of erbium ions in microcavity

Combining equation (5.3) with (5.5), the normalized erbium upper state population N_2/N_T can be expressed as follows:

$$\frac{N_2}{N_T} = \frac{\alpha_s + \alpha_s^{passive}}{\alpha_s + g_s^*}, \tag{5.9}$$

where the passive cavity signal loss $\alpha_s^{passive}$ is defined as,

$$\alpha_s^{passive} \equiv \frac{c}{n_s \tau_s} = \frac{2\pi n_s}{\lambda_s Q_{T,s}^{passive}}, \tag{5.10}$$

with $Q_{T,s}^{passive}$ the loaded quality factor at the signal wavelength, excluding the effects of erbium ions. Equation (5.9) is especially useful because it provides a simple relation between the normalized upper state population in the microcavity and the parameters of microcavity and erbium ions. It reflects the well-known *clamping* of the population inversion under lasing conditions. The normalized upper state population N_2/N_T is shown in Figure 5.2 as a function of gap width (cavity loading) and signal intrinsic Q-factor. The calculation is performed assuming $\Gamma_{s,p} = 1$, a signal wavelength of 1552.9 nm, erbium ion concentration of 2×10^{19} cm^{-3} and a cavity diameter of 50 μm coupled to a phase-matched tapered fiber. In the highly undercoupled regime (large gap width between the microcavity and the tapered fiber), the normalized erbium upper state population is determined by intrinsic signal quality factor and Giles-parameters. For ultrahigh Q-factor, it is set near $\alpha_s/(\alpha_s + g_s^*) = 0.39$ (determined by Giles parameters and therefore varying with lasing wavelength). At each preassumed lasing wavelength, a possible minimum N_2/N_T is defined by $\alpha_s/(\alpha_s + g_s^*)$ below which lasing will not be permitted. As the cavity loading increases (gap width decreases), the loaded signal quality factor decreases and therefore the normalized erbium upper state population increases (favoring the possibility of shorter wavelength lasing). It is well known that the peak gain wavelength [88] and the corresponding lasing wavelength are determined by the normalized erbium upper state population. In section 5.3, lasing wavelength control by change of cavity loading will be further examined on the basis of equation (5.9).

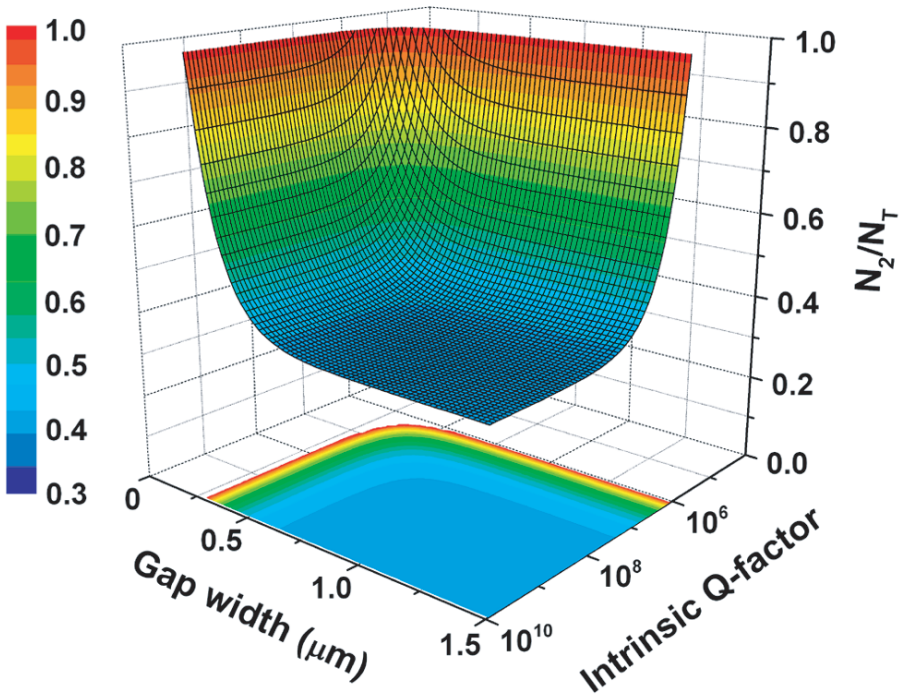

Figure 5.2: Normalized upper state population of erbium ions N_2/N_T under condition (5.3) calculated as a function of gap width (cavity loading) and signal intrinsic Q-factor.

5.1.2 Q-factors at pump and signal wavelengths

In the equation (5.9) for the population inversion, cavity loss $\alpha_s^{passive}$ at the signal wavelength is the only variable that can be controlled (after fabrication) by changing the waveguide loading of the cavity. This passive cavity signal loss $\alpha_s^{passive}$ can be expressed using the loaded Q-factor as in (5.10). In the case of weak coupling between the resonator and the waveguide, the decomposition of the loaded Q-factor for the passive (i.e., without the effects of erbium ions) microcavity is given by the following simple form:

$$\frac{1}{Q_T^{passive}} = \frac{1}{Q_0^{passive}} + \frac{1}{Q_{ext}}, \tag{5.11}$$

where Q_{ext} is the external Q-factor of the microcavity (determined by cavity loading) and $Q_0^{passive}$ is the intrinsic Q-factor originating from loss mechanisms such as cavity surface scattering, adsorbed surface water, residual OH^- impurities, whispering-gallery leakage, and bulk material absorption loss [2, 82]. For undoped, silica microcavities having diameters larger than approximately 20 μm and for the wavelength band of interest in this work

(1400–1600 nm), intrinsic Q-factors are limited primarily by water adsorption and surface scattering [2,34]. It should also be noted that in the present work, the erbium implantation process could potentially alter $Q_0^{passive}$ by the introduction of absorbing (point) defects in the ion beam modified silica network structure [89]. Transitions between the ground- and excited-state manifolds ($^4I_{15/2}$ and $^4I_{13/2}$) of erbium introduce signal gain and pump absorption terms as described in (5.1) and (5.2). By extending the definition of Q-factor to include these effects, the following "erbium-population-inversion dependent" cavity Q-factors can be obtained:

$$\begin{aligned}\frac{1}{Q_s^{Er}} &= \frac{\lambda_s}{2\pi n_s}\left[-\frac{N_2}{N_T}(\alpha_s + g_s^*) + \alpha_s\right] \\ &= -\frac{\lambda_s \alpha_s^{passive}}{2\pi n_s} \\ &= -\frac{1}{Q_{T,s}^{passive}},\end{aligned} \tag{5.12}$$

$$\begin{aligned}\frac{1}{Q_p^{Er}} &= \frac{\lambda_p}{2\pi n_p}\left[-\frac{N_2}{N_T}(\alpha_p + g_p^*) + \alpha_p\right] \\ &= \frac{\lambda_p}{2\pi n_p}\left[-\frac{\alpha_p + g_p^*}{\alpha_s + g_s^*}(\alpha_s + \alpha_s^{passive}) + \alpha_p\right] \\ &= \frac{\lambda_p}{2\pi n_p}\left(\frac{g_s^*\alpha_p - g_p^*\alpha_s}{\alpha_s + g_s^*}\right) - \frac{n_s\lambda_p}{n_p\lambda_s}\frac{\alpha_p + g_p^*}{\alpha_s + g_s^*}\frac{1}{Q_{T,s}^{passive}},\end{aligned} \tag{5.13}$$

where equation (5.9) has been used to relate the population inversion to other parameters. Using these intuitive definitions, the total Q-factors (including the effects of gain/loss from excited erbium ions) for the signal (lasing mode) and pump wave can be expressed as follows:

$$\frac{1}{Q_{T,s}} = \frac{1}{Q_s^{Er}} + \frac{1}{Q_{T,s}^{passive}} = 0, \tag{5.14}$$

$$\begin{aligned}\frac{1}{Q_{T,p}} &= \frac{1}{Q_p^{Er}} + \frac{1}{Q_{T,p}^{passive}} \\ &= \frac{\lambda_p}{2\pi n_p}\left(\frac{g_s^*\alpha_p - g_p^*\alpha_s}{\alpha_s + g_s^*}\right) - \frac{n_s\lambda_p}{n_p\lambda_s}\frac{\alpha_p + g_p^*}{\alpha_s + g_s^*}\frac{1}{Q_{T,s}^{passive}} + \frac{1}{Q_{T,p}^{passive}} \\ &= \frac{1}{Q_{0,p}^{Er}} + \frac{1}{Q_{ext,p}}.\end{aligned} \tag{5.15}$$

The condition stated in equation (5.14), which is the threshold condition expressed in terms of Q-factor, suggests that an infinite Q-factor for the signal wave is possible (i.e., perfect balance of gain and loss). However, the infinite Q-factor is a by-product of neglecting spontaneous emission in equation (5.1). In reality, this will not be observed because of the spontaneous emission, which is also responsible for a finite laser linewidth. Beside the form of equations (5.14) and (5.15) in lasing operation, another interesting regime is the condition of negligible upper state population inversion (i.e., weak pump condition). The weakly-pumped intrinsic Q-factors (including absorption both in the pump and the emission band) are given by setting the population inversion N_2/N_T to zero in equations (5.12) and (5.13):

$$Q^{Er}_{wp,s} \simeq \frac{2\pi n_s}{\alpha_s \lambda_s} = \frac{2\pi n_s}{\Gamma_s N_T \sigma^a_s \lambda_s}, \tag{5.16}$$

$$Q^{Er}_{wp,p} \simeq \frac{2\pi n_p}{\alpha_p \lambda_p} = \frac{2\pi n_p}{\Gamma_p N_T \sigma^a_p \lambda_p}. \tag{5.17}$$

Here, a "*wp*" subscript denotes that these Q-factors correspond to the weakly-pumped case (i.e., negligible upper state population).[2] Clearly, in the weak pump condition, higher erbium concentrations will reduce these quantities and, in turn, lower the total cavity Q-factor. These weakly-pumped intrinsic Q-factors are easily measured in experiments. Their measurement along with knowledge of basic parameters gives a rough estimate of the erbium concentration and overlap factor.

5.1.3 Lasing output power

To obtain the output lasing power as a function of input pump power, the upper state population is first expressed in terms of the internal cavity fields. From the rate equation for an excited population of erbium ions under steady-state conditions [83, 84, 87], the following expression results:

$$\frac{N_2}{N_T} = \frac{\frac{\alpha_s}{\nu_s}\frac{|a_s|^2}{n_s V^s_m} + \frac{\alpha_p}{\nu_p}\frac{|a_p|^2}{n_p V^p_m}}{\frac{\alpha_s + g^*_s}{\nu_s}\frac{|a_s|^2}{n_s V^s_m} + \frac{\alpha_p + g^*_p}{\nu_p}\frac{|a_p|^2}{n_p V^p_m} + \frac{hN_T}{c\tau_{Er,N_T}}}, \tag{5.18}$$

where $V^{s,p}_m$ are the effective pump and signal mode volumes in the microcavity, h is the Plancks constant and τ_{Er,N_T} is the lifetime of the erbium ions. This normalized upper state

[2]Roughly speaking, these expressions are obtained by letting $N_2/N_T \to 0$ in equations (5.12) and (5.13)

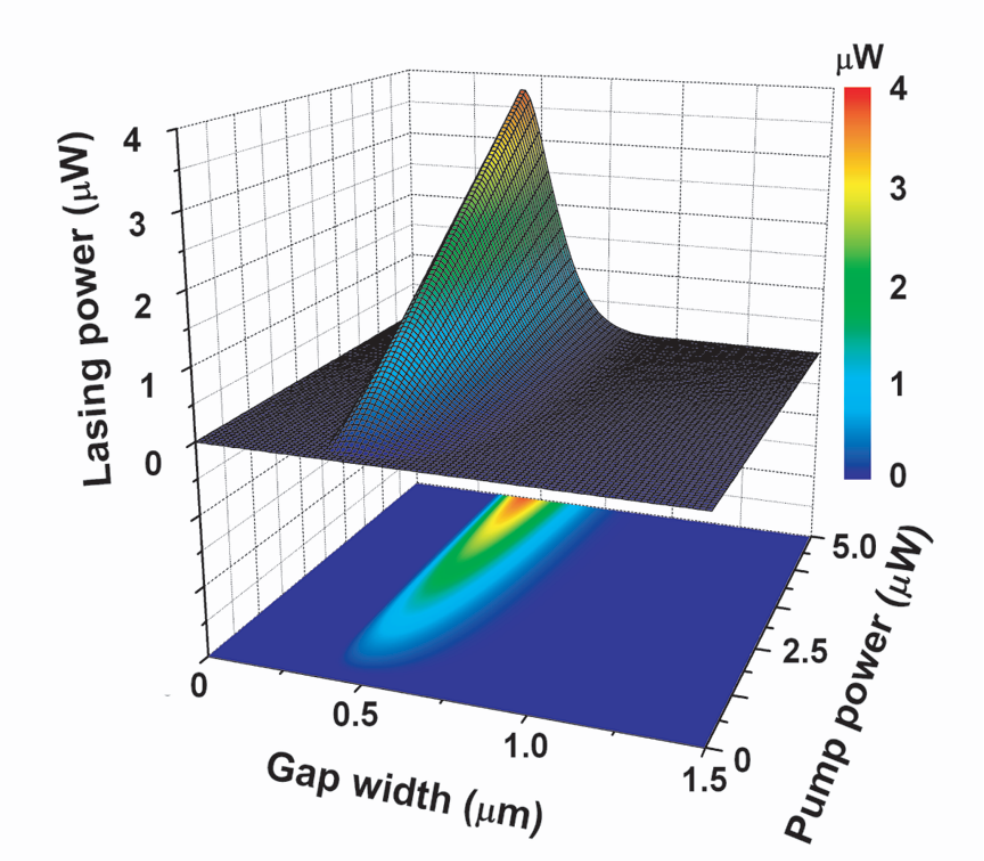

Figure 5.3: Lasing power calculated as a function of input pump power and gap width.

population is equated to its threshold value (assuming lasing condition and population clamping) from equation (5.9). After simple algebraic manipulation, the following relation between internal circulating pump and signal energies can be obtained:

$$|a_s|^2 = \left(\frac{\nu_s n_s V_m^s}{\nu_p n_p V_m^p}\right) \frac{\alpha_p(\alpha_s + g_s^*) - (\alpha_p + g_p^*)(\alpha_s + \alpha_s^{passive})}{\alpha_s^{passive}(\alpha_s + g_s^*)} |a_p|^2 - N_T h\nu_s V_m^s \frac{\alpha_{Er}(\alpha_s + \alpha_s^{passive})}{\alpha_s^{passive}(\alpha_s + g_s^*)}, \tag{5.19}$$

where $\alpha_{Er} \equiv n_s / c\tau_{Er,N_T}$. To relate these internal field quantities to the fiber-taper coupled quantities, the internal pump energy $|a_p|^2$ is related to the input waveguide power $|s_p|^2$ through the following expression (obtained by combining equations (5.4), (5.6) and (5.9)):

$$|a_p|^2 = \frac{4n_p^2\kappa_p^2(\alpha_s + g_s^*)^2}{c^2\left[(\alpha_p + \alpha_p^{passive})(\alpha_s + g_s^*) - (\alpha_p + g_p^*)(\alpha_s + \alpha_s^{passive})\right]^2} |s_p|^2. \tag{5.20}$$

Expressions (5.19) and (5.20) account for both waveguide loading and population-dependent coupling effects. To convert from internal cavity energy to output lasing power, the internal energy expression (5.19) is multiplied with κ_s^2 ($P_L = \kappa_s^2 \times |a_s|^2$). Figure 5.3 shows the output lasing power as a function of input pump power for different cavity loading conditions. Input parameters are the same as for the calculations in Figure 5.2. In addition, a pump wavelength of 1471 nm and $Q_0^{passive} = 4 \times 10^7$ are used. As can be seen, the lasing threshold is a sensitive function of the gap width. The slope efficiency, defined as the differential output power versus input power, is also strongly dependent on the coupling conditions. In the next section, we will further discuss the threshold power and differential slope efficiency.

5.1.4 Threshold and slope efficiency

The input (fiber launched) threshold pump power can be obtained directly from equation (5.19) and (5.20) by setting the internal circulating signal energy to zero and solving for the required pump power:

$$\begin{aligned} |s|_{th}^2 = {} & N_T h \nu_s V_m^s \left(\frac{\nu_s n_s V_m^s}{\nu_p n_p V_m^p} \right) \left(\frac{c^2}{4 n_p^2 \kappa_p^2} \right) \\ & \times \frac{\left[(\alpha_p + \alpha_p^{passive})(\alpha_s + g_s^*) - (\alpha_p + g_p^*)(\alpha_s + \alpha_s^{passive}) \right]^2}{(\alpha_s + g_s^*)^2} \\ & \times \frac{\alpha_{Er}(\alpha_s + \alpha_s^{passive})}{\alpha_p(\alpha_s + g_s^*) - (\alpha_p + g_p^*)(\alpha_s + \alpha_s^{passive})}. \end{aligned} \tag{5.21}$$

It should be noted that the threshold power derived here is a lower limit as modal coupling of counter-rotating pump waves [37, 81], concentration-related quenching, and excited state absorption are not taken into account. To obtain an expression for the coupled threshold power rather than input threshold power, it is necessary to account for the power coupled from the tapered optical fiber into the cavity (assuming perfect ideality [26]). The pump transmission is given by,

$$T_p = \left| 1 + j\kappa_p \frac{a_p}{s_p} \right|^2. \tag{5.22}$$

This quantity can be easily calculated using equation (5.20) and different cavity loading conditions can be divided into three characteristic regimes on the basis of (5.22); the three regimes are overcoupled ($0 < T_p < 1$, smaller gap width than critically coupled position),

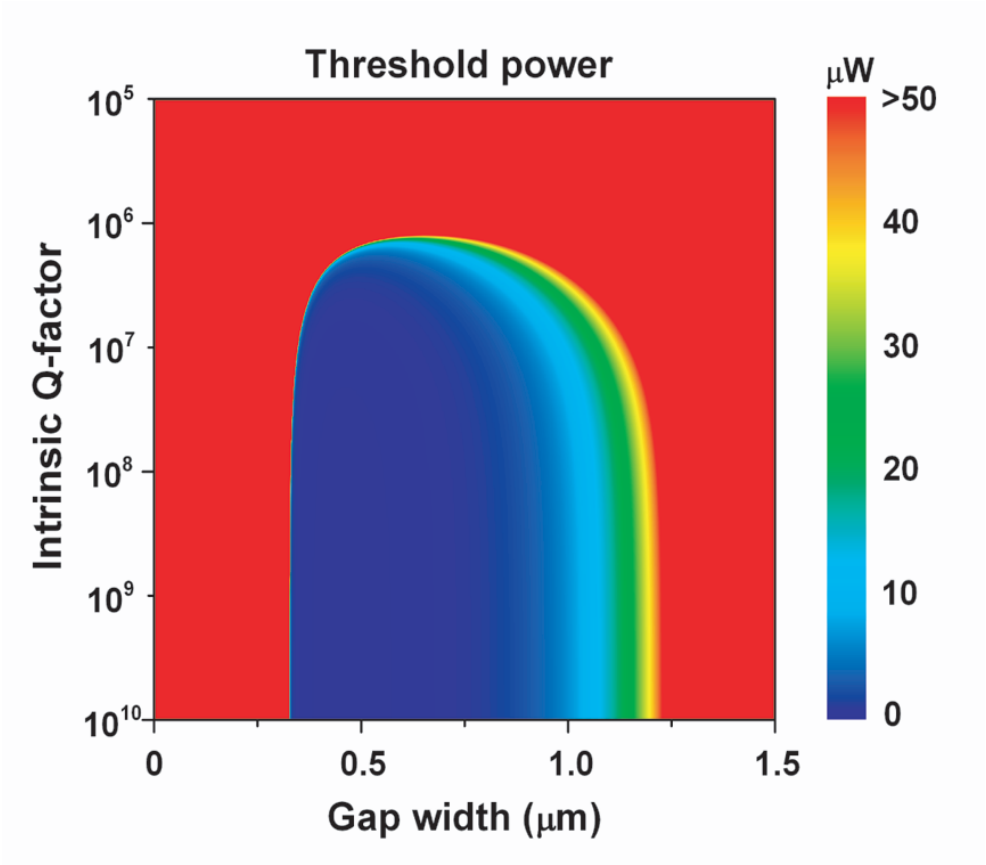

Figure 5.4: Threshold power as a function of gap width and intrinsic Q-factor.

critically coupled ($T_p = 1$), and undercoupled condition ($0 < T_p < 1$, larger gap width than critically coupled position), respectively. The coupled threshold power can now be expressed simply as,

$$P_{th}^{coupled} = (1 - T_p)|s|_{th}^2. \tag{5.23}$$

The differential slope efficiency expression can be derived from equation (5.19) and (5.20) as follows:

$$\eta \equiv \frac{dP_L}{d|s_p|^2} = \kappa_s^2 \left(\frac{\nu_s n_s V_m^s}{\nu_p n_p V_m^p}\right) \frac{\alpha_p(\alpha_s + g_s^*) - (\alpha_p + g_p^*)(\alpha_s + \alpha_s^{passive})}{\alpha_s^{passive}(\alpha_s + g_s^*)} \times \frac{4n_p^2\kappa_p^2(\alpha_s + g_s^*)^2}{c^2\left[(\alpha_p + \alpha_p^{passive})(\alpha_s + g_s^*) - (\alpha_p + g_p^*)(\alpha_s + \alpha_s^{passive})\right]^2}. \tag{5.24}$$

Figures 5.4-5.6 shows: the input threshold power, the slope efficiency, and the fraction of coupled input pump power, all as a function of cavity loading (gap width) and intrinsic

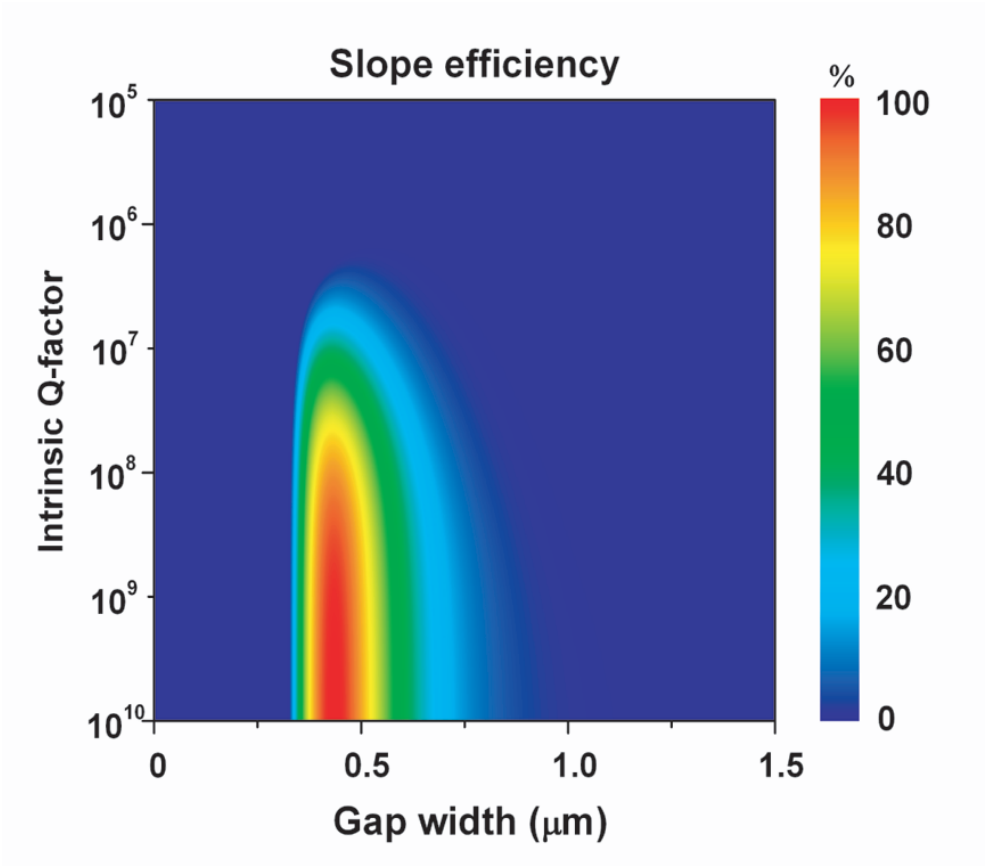

Figure 5.5: Slope efficiency as a function of gap width and intrinsic Q-factor.

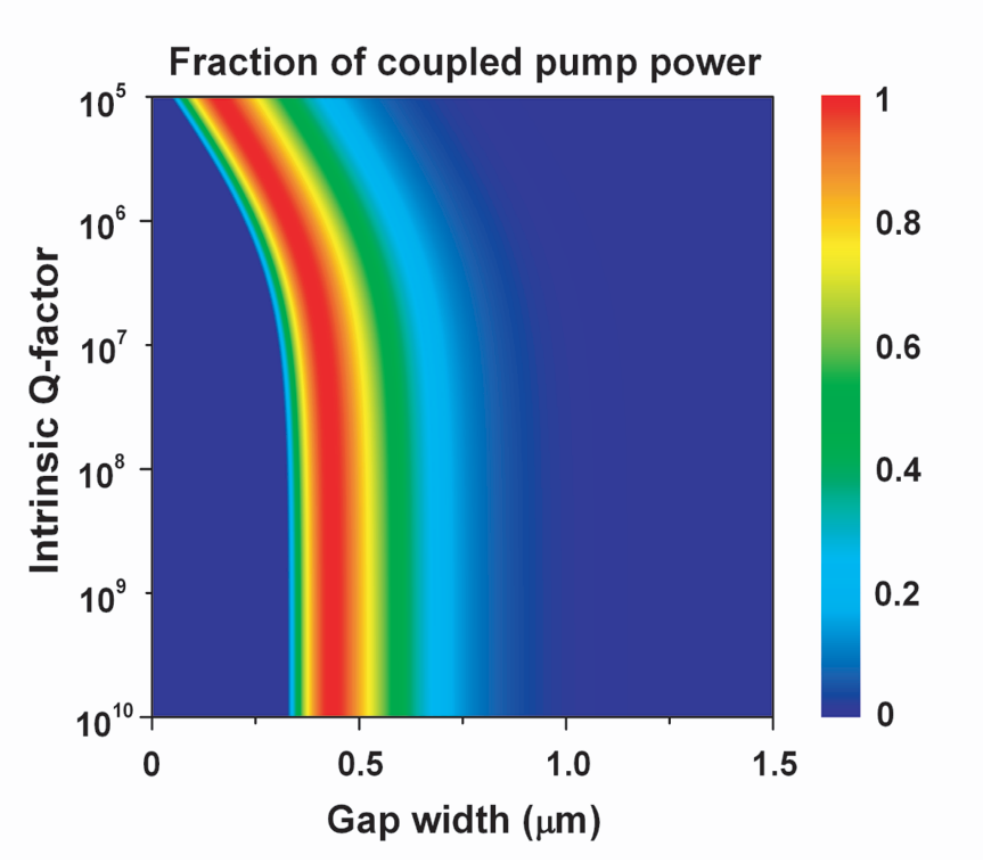

Figure 5.6: Fraction of coupled pump power as a function of gap width and intrinsic Q-factor.

Q-factor, calculated using (5.21), (5.24), and (5.22) using the same parameters as in Figure 5.3. Figure 5.4 shows that at a given Q-factor, the minimum threshold power is a sensitive function of gap width as also shown in Figure 5.3. The threshold increases sharply in the overcoupled regime (small gap width) due to the sharp increase in cavity loss, and in the undercoupled regime due to pump-coupling inefficiency from the fiber to the resonator. For an optimum gap width, the threshold increases for decreasing intrinsic Q-factor. The slope efficiency (Figure 5.5) reaches ∼100% for very high Q-factor (10^{10}) at an optimum gap width of ∼0.5 μm. It drops rapidly under over- and under-coupled conditions. This optimum gap width for the lowest threshold power and highest slope efficiency in Figure 5.4 and 5.5 corresponds to a slightly undercoupled condition, as can be seen in Figure 5.6. This figure also shows that the critical coupling point (as inferred by the gap width) is roughly constant for high intrinsic Q-factors and moves towards the microcavity as intrinsic Q-factor decreases (or $Q < 10^6$). This change of critical coupling point is caused by the variation of intrinsic erbium-related Q-factor ($Q_{0,p}^{Er}$, defined in (5.15)). As the intrinsic Q-factor decreases below 10^7, the intrinsic erbium-related Q-factor becomes independent of erbium parameters and related only to intrinsic Q-factor, leading to a decrease in critical coupling gap width. Asymmetries of threshold power, slope efficiency and the fraction of coupled power with respect to gap width of minimum/maximum value are observed in Figure 5.4-5.6. These asymmetries result from the lasing condition imposed on minimum gap width for lasing (maximum achievable gain should be larger than the total round trip loss), which will be discussed in the next section.

5.1.5 Lasing condition revisited

Equation (5.9) can be used to establish a lower bound for the erbium ion concentration required to obtain lasing in a cavity with a given passive Q-factor. Taking into account that the maximum upper state population cannot exceed the total erbium ion concentration ($N_2 < N_T$) in (5.9),

$$g_s^* > \alpha_s^{passive}. \tag{5.25}$$

Equation (5.25) sets the limit on the minimum erbium concentration at fixed passive intrinsic quality factor required to overcome loss. Rewriting (5.25) using the constituent relation

given by (5.8) and (5.10), the minimum erbium ion concentration is bounded by,

$$N_T > \frac{2\pi n_s}{\lambda_s \Gamma_s \sigma_s^e Q_{T,s}^{passive}}. \tag{5.26}$$

As an illustrative example, by assuming the parameters discussed above, and a passive Q-factor of 5×10^7, the erbium concentration should be greater than 7.3×10^{17} cm^{-3} (0.001 at. %). Under 980 nm pumping nearly complete inversion is feasible and the limits contemplated in equation (5.26) may be achieved. However, when pumping occurs in the erbium absorption band at or slightly below 1.5 μm, pump stimulated emission must be taken into account. A tighter bound on N_T is then obtained by following two lines of reasoning. First, from (5.19), the following inequality is required for positive differential slope efficiency (i.e., lasing operation):

$$\alpha_p \frac{(\alpha_s + g_s^*)}{(\alpha_p + g_p^*)} - \alpha_s > \alpha_s^{passive}. \tag{5.27}$$

For the special case of 980 nm band pumping (at which wavelength the emission cross section is nearly zero), equation (5.27) becomes identical to (5.25). However, in general (5.27) is a stricter condition. Inequality (5.27) can also be obtained by setting a limit on the maximum achievable population inversion in equation (5.9):

$$\frac{N_2}{N_T} < \frac{\alpha_p}{\alpha_p + g_p^*}, \tag{5.28}$$

which is the limit of population inversion when the pump energy is high in (5.18) (i.e., is near the emission band). Figure 5.7 is a plot of the gap width above which lasing is possible at a given erbium concentration. Curves are shown for passive cavity Q-factors ranging from 2×10^7 to 1×10^8. Several features are apparent in the figure. First, for a fixed passive intrinsic Q-factor, there is a minimum erbium ion concentration required for lasing action. As the passive intrinsic Q-factor becomes larger, the required minimum erbium ion concentration decreases. Second, for high erbium ion concentration, the minimum gap width for lasing decreases and eventually becomes zero (at which tapered fiber and microcavity contact each other). This characteristic concentration (3.4×10^{20} cm^{-3}, 0.5 at. % in this case) above which lasing can be observed with zero gap width is independent of intrinsic

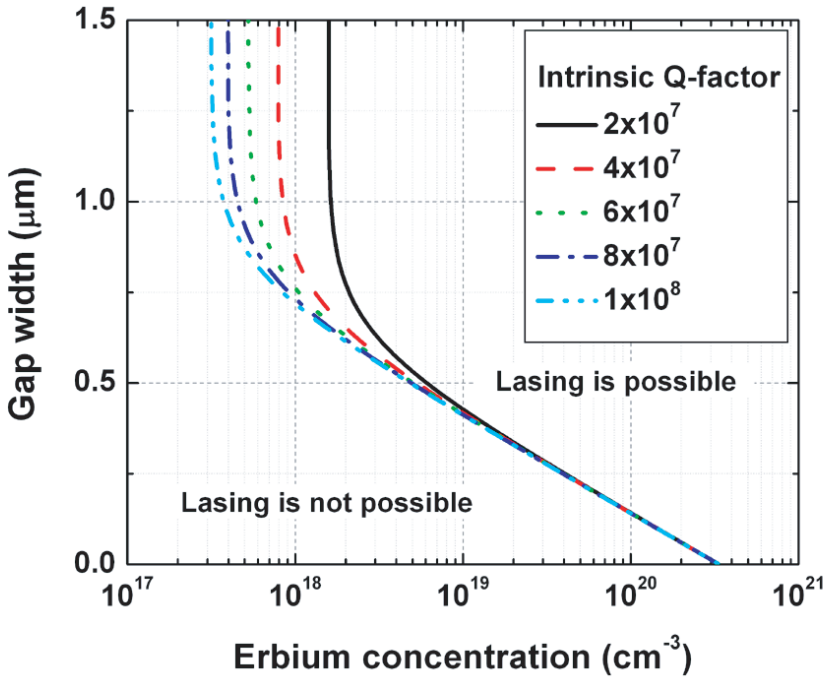

Figure 5.7: Gap width to obtain lasing at a given erbium concentration. Data are shown for different passive cavity intrinsic quality factor $Q_0^{passive}$ in the range from 2×10^7 to 1×10^8.

Q-factors and determined mainly by erbium parameters and microcavity size parameters.

5.1.6 Dependence on erbium concentration

For the purpose of optimizing the coupled threshold power and differential slope efficiency as a function of erbium ion concentration, equations (5.21) and (5.24) are evaluated. In this analysis, cooperative upconversion or ion paring are not taken into account. Instead, to take into account concentration quenching and subsequent lifetime shortening of the erbium ions, the concentration-dependent erbium upper-state lifetime τ_{Er,N_T} is assumed to follow the reduction formula (with quenching concentration N_Q of 5×10^{20} cm$^{-}3$ assumed) given in [90]:

$$\tau_{Er,N_T} = \frac{\tau_{Er}}{1 + (N_T/N_Q)^2}. \tag{5.29}$$

Figure 5.8 shows the minimum achievable threshold power plotted as a function of erbium concentration and intrinsic Q-factor. For a given Q-factor, there is an optimal erbium ion concentration, which gives the lowest input threshold power. The higher the intrinsic

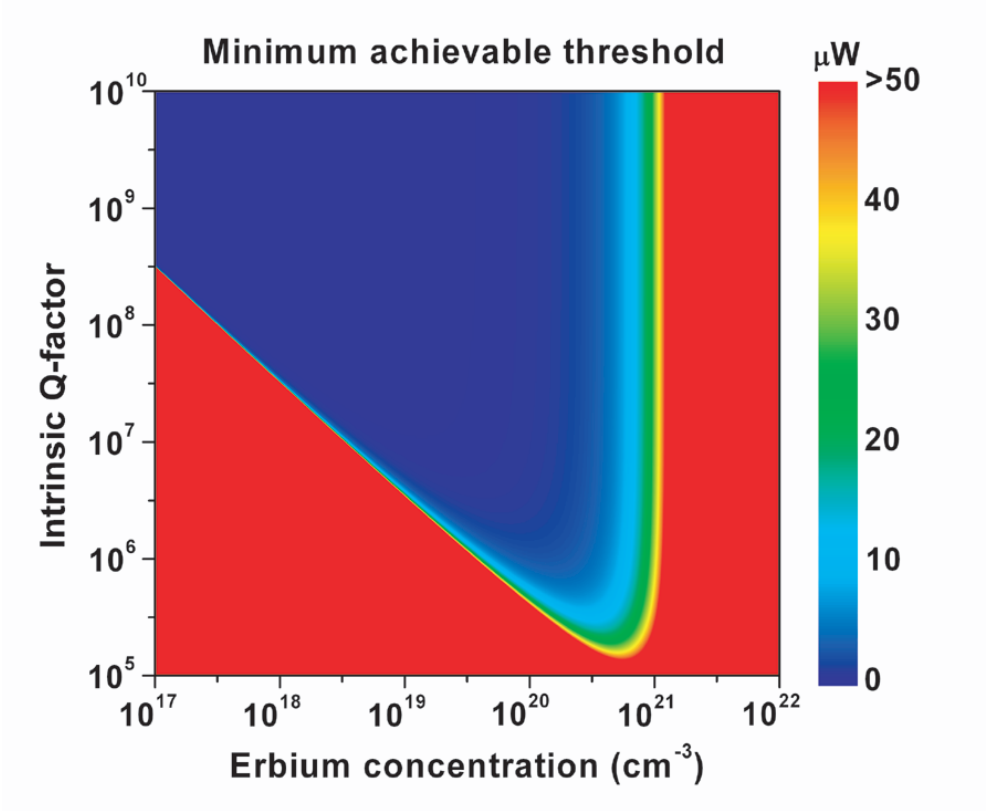

Figure 5.8: Minimum achievable threshold power plotted as a function of erbium ion concentration and intrinsic Q-factor.

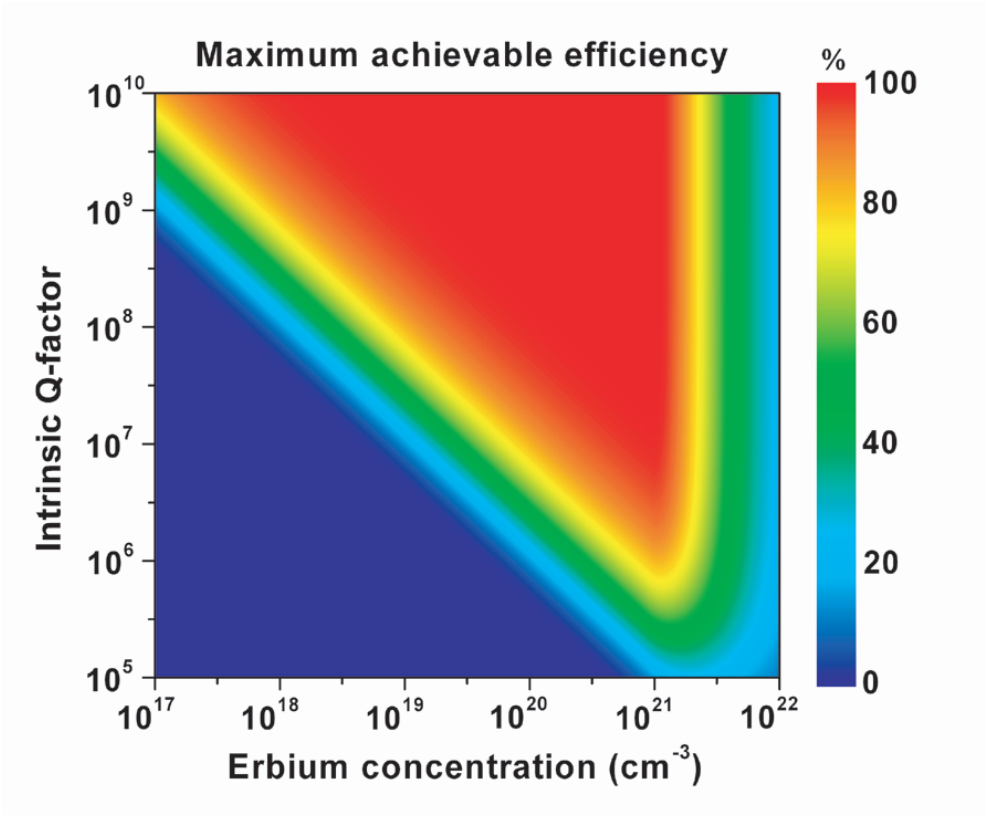

Figure 5.9: Maximum achievable differential slope efficiency plotted as a function of erbium concentration and intrinsic Q-factor.

Q-factor, the lower the optimum erbium concentration. On either side of the optimum concentration, the threshold power increases sharply with concentration. The increase on the low-concentration side is caused by condition (5.27); the increase on the high-concentration side is caused by concentration quenching, increase in pump transmission (reduced pumping efficiency, see Figure 5.6) and higher erbium concentration itself. Figure 5.9 shows the maximum achievable differential slope efficiency as a function of total erbium ion concentration and intrinsic Q-factor. At a given Q-factor, the slope efficiency initially becomes larger as the erbium concentration increases and then becomes smaller beyond a characteristic erbium concentration of 9×10^{20} cm^{-3} ($\sim$1.4 at. %). For a given Q-factor $> 10^6$, $\sim$100% efficiency can always be achieved, provided Q-factor and junction ideality is sufficiently high. Note that while these calculations do take into account the concentration-quenching related reduction in lifetime at high erbium ion concentrations, cooperative upconversion is not taken into account. This effect reduces the effective erbium ion population that can be achieved at a given pump power. Inclusion of this effect will cause a reduction in the achievable slope efficiency at given erbium ion concentration and Q-factor.

5.1.7 Mode volume, external coupling efficiency, and size of toroidal microcavity

The expressions derived in this section can be applied to any erbium-doped laser analysis. In this paper, the laser cavity corresponds to a toroidal microcavity, and the coupling, both to and from the toroidal microcavity, is achieved by evanescent-field coupling using a tapered optical fiber [25, 26, 91]. Because analytic expressions are not available for the coupling dependence on gap width and mode volume, the present analysis uses values in comparably-sized microspheres for which there are readily available analytical expressions [34, 80]. This will cause slight differences in the results. For example, the mode volume in a toroidal microcavity is smaller than that in a spherical cavity of the same diameter [13]. It is an approximately quadratic function of the major diameter of toroidal microcavity. As the lasing threshold is linear in mode volume (see equation (5.21)), the lowest lasing threshold power is expected for small toroids. For very small toroids, however, radiative (whispering-gallery) loss becomes dominant, and thus the smallest diameter of a toroidal microlaser that can be practically achieved is determined by a balance between gain (erbium concentration)

and loss, given a certain available pump power. From a calculation assuming an erbium concentration of 2.5×10^{20} cm^{-3} (for which the effects of concentration quenching and cooperative upconversion are relatively small) and the known size-dependent whispering-gallery loss [34], it follows that the smallest toroidal microcavity diameter is typically ~ 15 μm.

5.2 Fabrications of erbium-implanted toroidal microcavities

In this section we present fabrication procedures and structural data on toroidal microlasers that were doped with erbium by ion implantation. The starting platform for the fabrication of these microcavities is an intrinsic Si(100) wafer with a 2 μm thick SiO_2 film grown by thermal oxidation. The fabrication consists of five steps involving erbium ion implantation, high-temperature thermal annealing, photolithography, wet/dry etching and CO_2 laser reflow/annealing. Erbium ion implantation is performed with 2 MeV erbium ions at fluences of 1.2×10^{15}, 4.2×10^{15}, and 1.2×10^{16} cm^{-2} using a Van de Graaff accelerator. The erbium doping depth profile was measured by Rutherford backscattering spectrometry and is well fitted by a Gaussian with a peak depth of 562 nm and a standard deviation of $\sigma = 72$ nm. The peak erbium ion concentrations for the three implant fluences were 0.10, 0.35, and 1.0 at. %, respectively. To optically activate the erbium ions, the implanted wafer was annealed at 800°C for 1 hour in vacuum. Our data demonstrate that the 800°C thermal anneal is sufficient to restore the silica networks structure, to incorporate erbium ions on optically active sites, and to reduce the defect density to a low level so that high intrinsic Q-factor is achieved (see further on). The photoluminescence lifetime at 1.535 μm for the sample implanted with 4.2×10^{15} cm^{-2}, measured after annealing, is 10 ms (See Figure 5.10). This value is lower than the radiative lifetime of erbium ions in thermally grown SiO_2 (17 ms), which is ascribed to concentration quenching due to resonant energy transfer among erbium ions followed by quenching at OH^- impurity sites. Processing of the implanted wafers into toroidal microcavities proceeds as described elsewhere [23]. Figure 5.1 shows the graphical rendering of the toroidal microcavity with tapered optical fiber and the inset in Figure 5.11 shows a scanning electron microscope (SEM) image of a toroidal microcavity (major diameter of 23 μm) used in the experiment. Briefly, after the high temperature annealing process,

circular photoresist pads (40-100 μm diameter) are created on the erbium-implanted silica film by standard photolithography. Next, the sample is immersed in buffered HF at room temperature to remove unpatterned silica. In this way, arrays of circular silica disks are fabricated on the silicon chip. Isolation of the silica disks from the silicon substrate is needed to prevent unwanted light leakage into the silicon substrate. This is achieved by isotropic, silicon dry etching using XeF_2, leaving silica disks supported by a silicon pillar structures. Finally, to create ultrahigh-Q toroidal microcavities, the silica disks are selectively reflowed by irradiation using a CO_2 laser ($\lambda = 10.6$ μm). As has been demonstrated before [23], this leads to melting and subsequent collapsing of the silica disk to a toroidal shape, with limiting dimensions defined by the width of the supporting silicon pillar. Toroidal microcavities made in this way exhibit record high Q-factors for planar devices in excess of 10^8 and therefore make excellent base resonators for the study of erbium-doped laser structures [78,79]. To study the effect of laser annealing on the optical properties of the erbium ions, we measured luminescence decay traces at 1.535 μm for both disk and toroidal microcavities (i.e., both pre- and post-reflow process), and they exhibit similar lifetimes of $\sim$10 ms [79]. In the following analysis we have assumed that as a result of the laser annealing, the erbium ions are homogeneously distributed throughout the toroidal volume, at average concentrations of 6×10^{18}, 2×10^{19}, and 6×10^{19} cm^{-3}, for the three implant fluences, respectively (corresponding to concentrations of 0.009, 0.03, and 0.09 at. %, respectively).

5.3 Experiment and characterization

A typical, high-resolution transmission spectrum measured through the fiber coupled to the erbium-implanted toroidal microcavity (4.2×10^{15} erbium/cm^2) is shown in Figure 5.11. The spectrum was measured by scanning a narrow-linewidth (<300 kHz), tunable (1400–1500 nm), external-cavity laser across a toroidal microcavity whispering-gallery resonance and monitoring the transmitted power using a photodetector (125 MHz). The frequency scanning speed (<100 Hz) of the laser was carefully chosen to satisfy both the quasi-steady-state condition imposed by the erbium ion decay rate and the maximum scanning speed condition required for the precise measurement of high Q-factors. To couple light efficiently in and out of the erbium-implanted toroidal microcavity, a tapered optical fiber (diameter

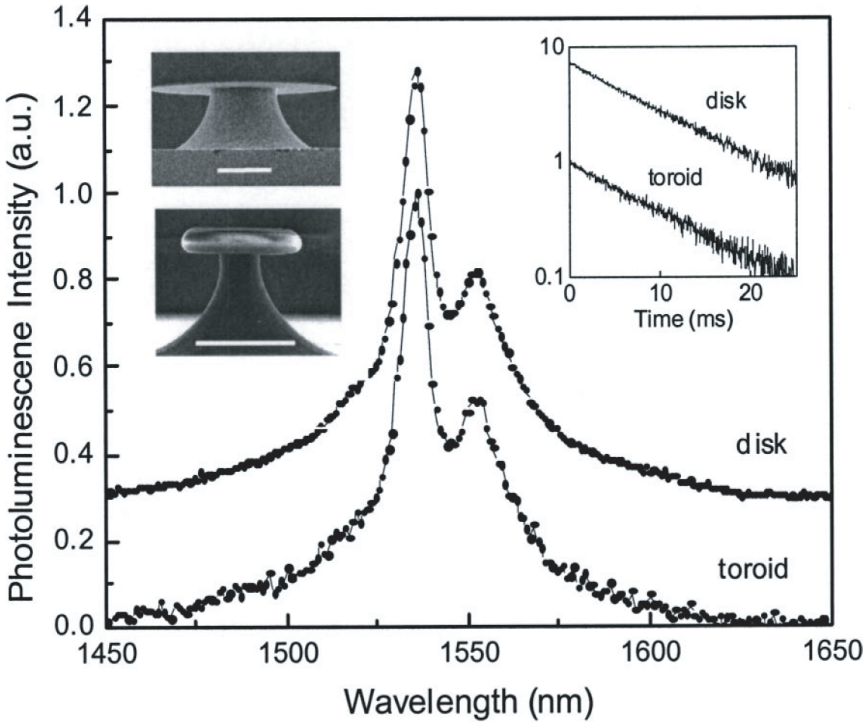

Figure 5.10: Photoluminescence spectra of erbium-implanted microresonators before and after laser annealing (the spectrum for the disk is shifted vertically for clarity). The right inset shows photoluminescence decay traces measured at $\lambda = 1535$ nm for both a disk and a toroid. The left insets show scanning electron microscopy images of a microresonator disk and toroid. Scale bars are both 43 μm.

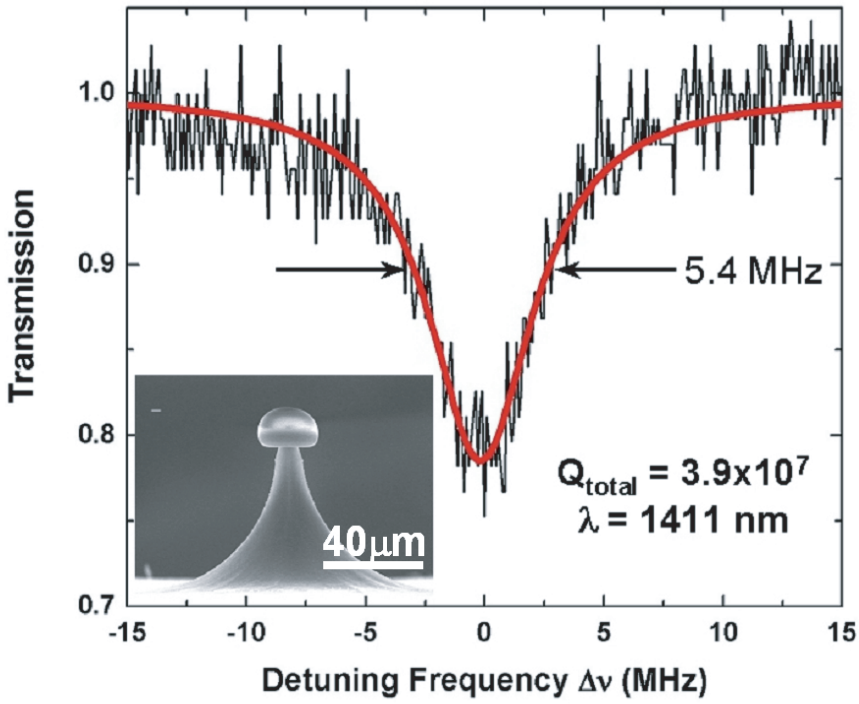

Figure 5.11: High-resolution whispering-gallery mode spectrum. Inset: SEM micrograph of a microcavity used in the experiment.

of 1-2 μm) was aligned in the equatorial plane of the toroidal microcavity. Taper fabrication and coupling characteristics are described elsewhere [25, 26, 91]. The microcavity was attached to a piezoelectric stage (minimum step size of 20 nm) that allowed for its precise positioning with respect to the tapered optical fiber. In the spectrum of Figure 5.11, the laser center wavelength was set to 1411 nm and the resulting loaded Q-factor was 3.9×10^7. To prevent thermal broadening and spectral distortion [92] associated with the high-Q, the input power was always kept below 10 μW during measurement of the resonance. Because the measurement was performed in the undercoupled regime ($\sim$79% transmission) and well below the lasing threshold, i.e., with the major fraction of the erbium ions in the ground state $^4I_{15/2}$, the observed linewidth provides a good estimate of the unloaded Q-factor. The erbium absorption related contribution to Q-factor can be estimated using (5.17) and yields $Q_0^{Er} = 3.25 \times 10^7$ (assuming $N_T = 2 \times 10^{19}$ cm^{-3}, $\sigma_p^a = 1 \times 10^{-22}$ cm^2, $n_p = 1.46$, and $\Gamma_p = 1$). It is therefore believed that the measured Q-factor is predominantly caused by the

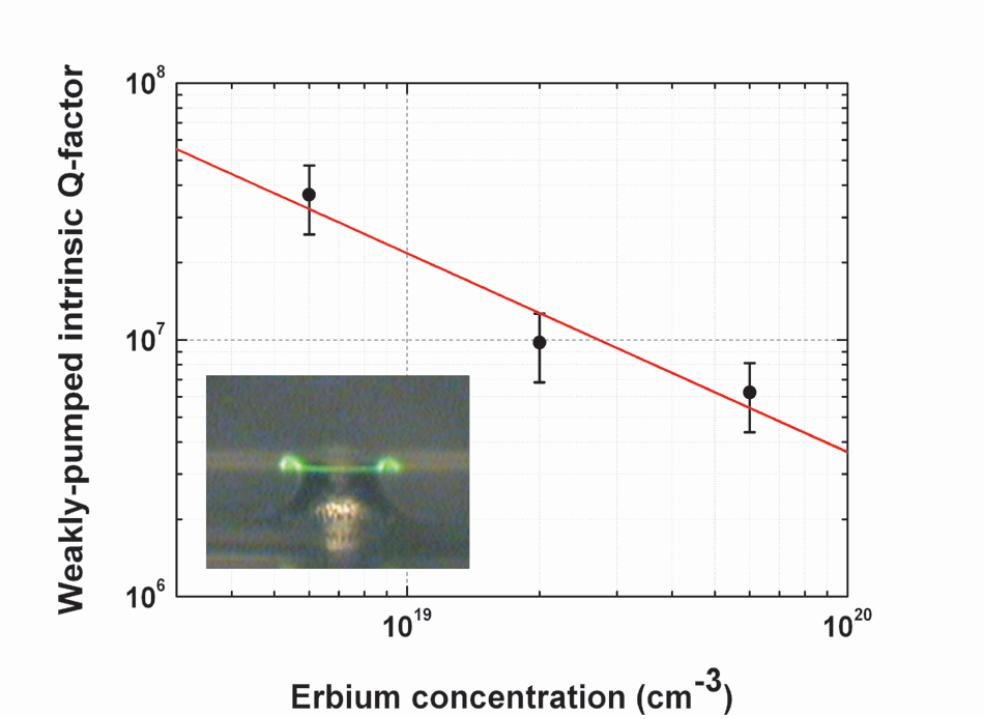

Figure 5.12: Measured weakly pumped intrinsic Q-factor (normalized to the pump wavelength of 1450 nm) as a function of erbium concentration and its linear fit on a log-log scale. Inset: upconversion luminescence observed in toroidal microcavity with implantation fluence of 1.2×10^{16} cm^{-2}.

absorption of erbium ions. To confirm the inverse relation between weakly-pumped intrinsic Q-factor and erbium ion concentration given by (5.16) and (5.17), weakly-pumped Q-factors at three different concentrations were measured as shown in Figure 5.12. A complication that arises when comparing Q-factors for different resonators is that all resonators have different resonance wavelengths, determined by their slightly different geometry. In order to compare Q-factors, they have been normalized to values at a wavelength of 1450 nm, using the known erbium absorption cross-section spectrum [84] as a (inverse) normalization factor. The line in Figure 5.12 provides the expected inverse relation between Q-factor and erbium concentration and fits the data well. This further confirms that the measured Q-factors are dominated by erbium-related absorption. The inset of Figure 5.12 shows a side-view color optical micrograph of a toroidal microcavity with high doping concentration (erbium ion fluence 1.2×10^{16} cm^{-2}, 0.09 at. % average), under high-intensity pumping. Green emission, resulting from second-order cooperative upconversion between exciter erbium ions is clearly seen. This green emission was not observed for toroidal microcavities doped at lower er-

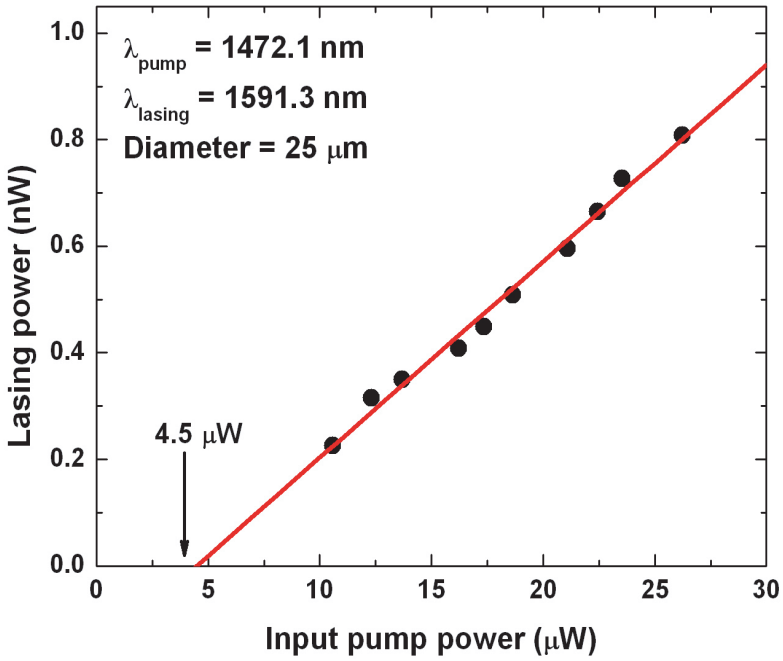

Figure 5.13: Measured lasing power as a function of input pump power for two different microcavity lasers showing two distinctive regimes of operation (all data are obtained for toroidal microcavities with a fluence of 4.2×10^{15} cm^{-2}). Low threshold fiber-launched power obtained from microcavity of 25 μm diameter.

bium concentrations. Figure 5.13 and 5.14 show the measured output lasing power versus fiber-coupled, input pump power for a microlaser implanted with 4.2×10^{15} erbium/cm^2. To pump the microlaser, the same laser used to measure the resonance spectrum in Figure 5.11 was tuned to a toroidal microcavity resonance within the absorption band (1460–1480 nm) of the erbium ions. Input pump power and lasing output power were carefully measured in order to account for modest amounts of tapered fiber loss. Two sets of measurements corresponding to two, different toroidal microcavities are presented in Figure 5.13 and 5.14. These devices illustrate two, distinctive operating conditions (low threshold and high output power). The order of magnitude difference in threshold powers of these devices is attributed to the difference in the size of microcavities as well as in the Q-factor. In Figure 5.13, a threshold power of 4.5 μW is observed for a 25 μm diameter toroidal microcavity (lasing wavelength of 1591.3 nm and pump wavelength of 1472.1 nm). The pump transmission was about $\sim$50% in this measurement so the actual coupled threshold pump power is estimated

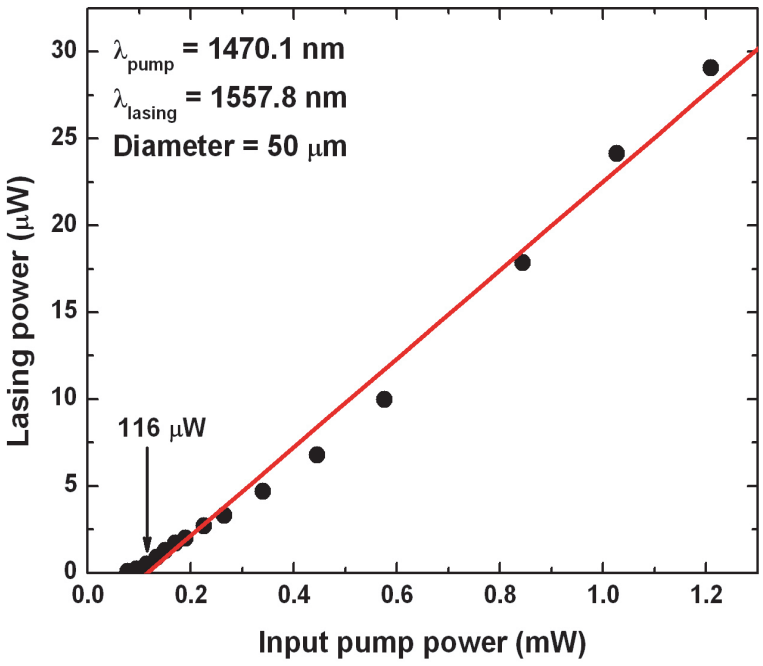

Figure 5.14: Measured lasing power as a function of input pump power for two different microcavity lasers showing two distinctive regimes of operation (all data are obtained for toroidal microcavities with a fluence of 4.2×10^{15} cm^{-2}). High output power obtained from microcavity of 50 μm diameter.

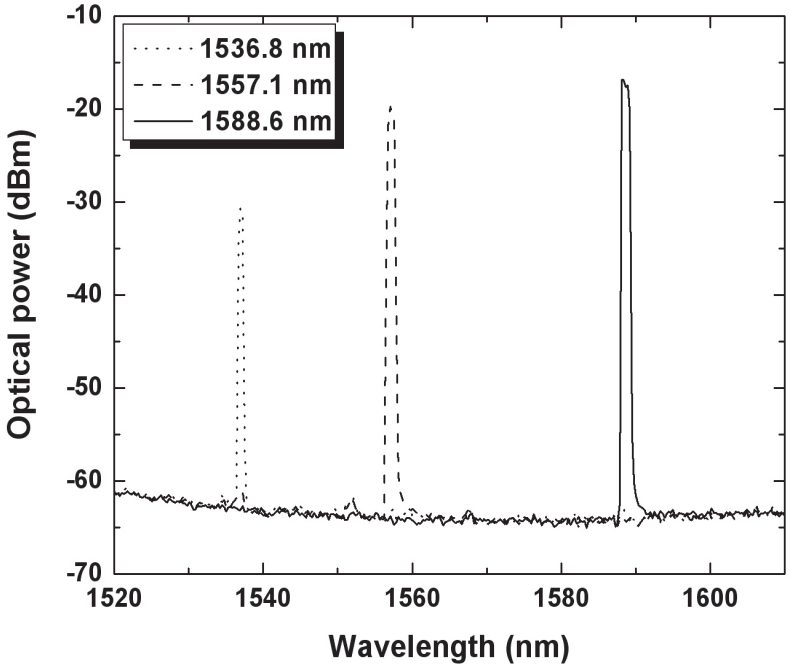

Figure 5.15: Discrete lasing wavelength control by variation of the waveguide-resonator gap distance (50 μm toroidal microcavity).

to be approximately 2-3 μW. This is, to the author's knowledge, the lowest threshold power reported for any erbium-doped laser. In this case, the Q-factor was so high that even at very low input pump power (<100 μW), thermally induced resonance broadening [92] and associated increase in pump power transmission (due to a finite frequency scanning range in experiment) resulted in a saturated output lasing power which prohibited further output power increase. Figure 5.14 shows a measurement with relatively high output lasing power (unidirectional slope efficiency = 2.6%) measured using a 50 μm diameter toroidal microcavity. The measured output power was 29 μW and the input threshold power was 116 μW. From a series of experiments on the same microcavity and for different cavity loading conditions, the highest (unidirectional) output power measured was 39.4 μW and the highest unidirectional slope efficiency was about 5.5%. The dependence of threshold, slope efficiency, and lasing wavelength on cavity loading (i.e., the gap width) by the tapered fiber was also investigated. Figure 5.15 contains a series of lasing wavelength scans under varying loading conditions and illustrates the effect of increased cavity loading on

oscillation wavelength. This measurement was performed using the same microcavity laser of Figure 5.14. At large gap width (corresponding to the undercoupled or weakly loaded regime), lasing at relatively longer wavelengths (1588.6 nm) is observed. As the gap width decreases (cavity loading increases), the lasing wavelength shifts in discrete steps to shorter wavelengths enabling us to broadly tune the lasing wavelength by the adjustment of cavity loading. This effect is believed to be due to the cavity-loading-induced change in the required inversion of erbium ions (equation (5.9)). In particular, as the loading increases (gap width decreases), and thus loaded Q-factor decreases, the oscillation wavelength must adjust to shorter wavelengths where the available erbium gain is larger (assuming that the Q-factors are the same for all the whispering-gallery modes in the erbium gain-bandwidth). This kind of discrete wavelength tuning was possible only in microcavities of moderate sizes. For larger cavity diameter (>70-80 μm), and hence smaller free spectral range (FSR), multimode lasing was dominant. For smaller diameters below $\sim$40 μm, the FSR is so large that within the erbium gain spectrum only one lasing wavelength satisfies the lasing condition, at an erbium upper state population determined by the gap width. The input threshold power and unidirectional slope efficiency were investigated as a function of cavity loading for two lasing wavelengths 1557.1 nm and 1588.6 nm. Figure 5.16 shows the input threshold power as a function of gap width between the tapered fiber and the microcavity. In the undercoupled regime, lasing starts at a relatively long wavelength (1588.6 nm) first with high threshold due to the small pump coupling. As the gap width decreases the threshold decreases at first, but ultimately increases abruptly near the gap-distance limit ($\sim$1.1 μm) defined by the condition (5.27). Eventually lasing at 1588.6 nm can no longer be supported because the increased cavity loading (and hence reduced Q-factor) cannot be compensated by the relatively small gain at this wavelength (small emission cross section). As the coupling distance is further reduced, the next lasing line at 1557.1 nm appears and similarly, the threshold power is observed to increase near the gap-distance limit ($\sim$0.4 μm for this wavelength). The inset in Figure 5.16 shows the differential slope efficiency as a function of gap width for the two lasing wavelengths. Starting from the weakly loaded regime, the differential slope efficiency increases as the cavity loading increases and reaches a maximum, in quantitative agreement with the calculations in Figure 5.5. The same is observed for the second lasing line that appears with increased loading. For each lasing wavelength, the

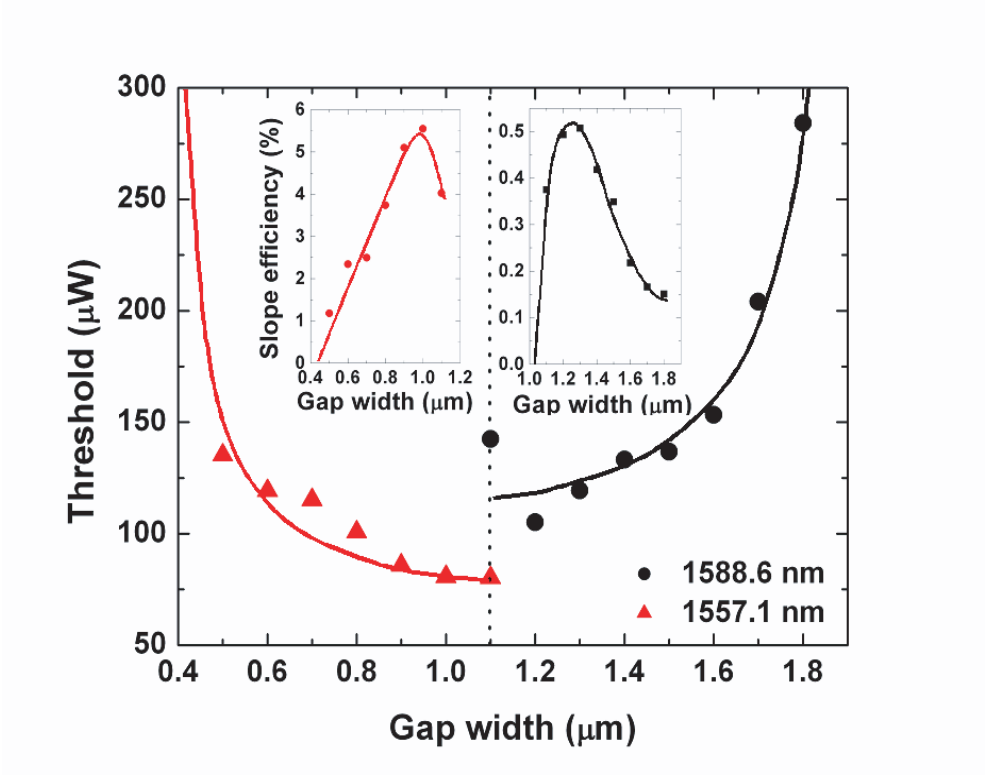

Figure 5.16: Threshold power as a function of gap width between the tapered fiber and the microcavity for two sequential lasting modes. Inset: differential (unidirectional) slope efficiency as a function of gap width between the tapered fiber and the microcavity for the same lasing modes. The drawn lines are guides for the eyes.

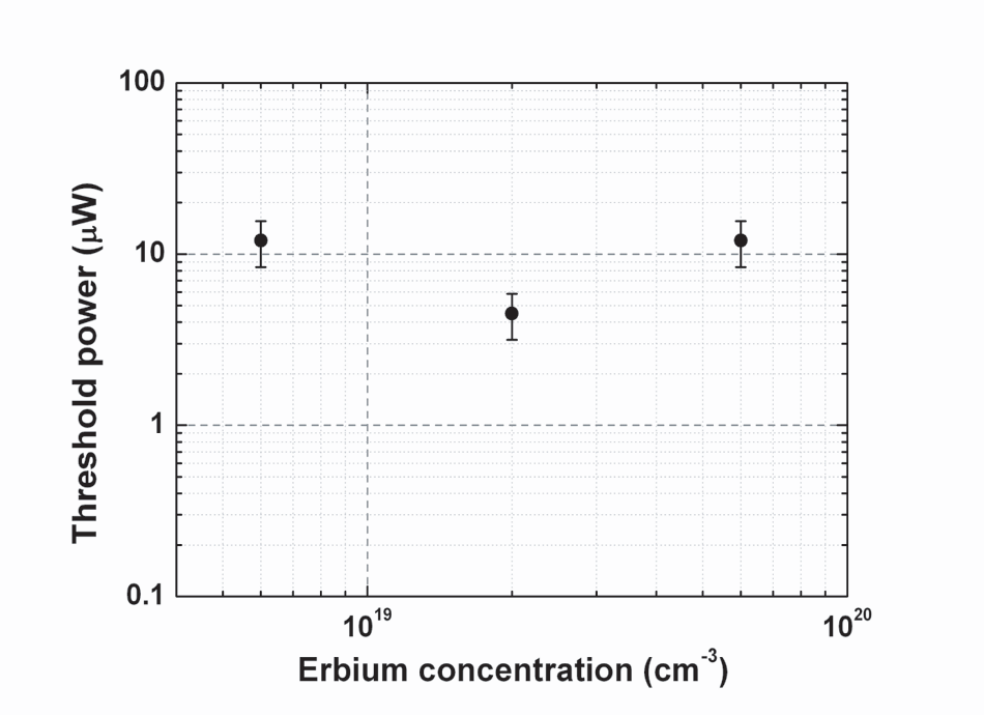

Figure 5.17: Minimum threshold power achieved from different samples with various erbium concentrations.

lowest threshold and highest slope efficiency are achieved at the same optimum gap width, in agreement with Figure 5.4 and 5.5. Figure 5.17 shows the threshold power measured for toroidal microcavities having three different erbium concentrations. The top axis shows the erbium concentration assuming erbium ions are homogeneously distributed in the toroidal microcavity. In each case, multiple measurements were performed on a series of toroidal microcavities with the same erbium ion fluence, and the lowest measured threshold was plotted in Figure 5.17. The data show only a weak dependence on erbium concentration. This, and the absolute values of the measured thresholds, is in qualitative agreement with Figure 5.8, which shows a weak dependence on concentration in the concentration range from 7×10^{18} to 3×10^{19} cm^3 for an intrinsic Q of 10^7, typical for our experiments.

5.4 Conclusions

Lasing in erbium-implanted high-Q silica toroidal microcavities coupled to a tapered fiber has been investigated analytically and experimentally. Threshold powers as low as 4.5 μW and output power of 39.4 μW are experimentally achieved using differently sized resonators

and coupling conditions. Controlling the lasing wavelength was possible by changing the tapered-fiber-microcavity gap width. Formulas predicting various performance metrics such as threshold power, differential slope efficiency, optimum concentration of erbium ions, as well as the influence of resonator size and the Q-factors were derived and the calculations are in good agreement with the experimentally obtained results.

Chapter 6

Parametric/Raman Toroidal Microcavity Lasers

Toroidal microcavity resonators have extended the performance of well-known spherical resonators (including liquid microdroplets) by providing both a simplified resonator spectrum and ultrahigh-Q performance on a silicon micro-electronic chip. Like microspheres they provide a combination of effectively-long-interaction length (high quality factor) and microscale mode volume so that even weak nonlinear mechanisms, such as stimulated Raman scattering, are observable at only tens of microwatts of input power, which is orders of magnitude lower than corresponding threshold powers for fiber-based Raman lasers [93]. However, in contrast to microsphere resonators, microtoroids have proven to be more versatile by recently enabling the first demonstration of a Kerr-nonlinearity optical parametric micro-oscillator (micro-OPO) [17]. Micro-OPOs are more challenging to realize than their stimulated counterparts as they require both ultrahigh-Q performance and phase-matching of the underlying nonlinear process. The following two conditions should be met by interacting waves inside the toroidal microcavity:

$$\Delta f = 2f_p - f_s - f_i \quad \text{(energy conservation)}, \tag{6.1}$$

$$\Delta \beta = 2\beta_p - \beta_s - \beta_i \quad \text{(momentum conservation)}, \tag{6.2}$$

where f_p, f_s and f_i are pump, signal and idler mode frequencies, β_p, β_s and β_i are pump, signal and idler mode propagation constants, respectively. Of the two requirements for matching (momentum and energy conservation), momentum conservation is intrinsically

satisfied in microcavities for symmetrically-located signal and idler modes with respect to the pump mode. This is a natural consequence of the rotational symmetry which yields a propagation constant $\beta_m = 2m/D_e$, where m is an azimuthal mode number and D_e is an effective diameter of the light path in the cavity.[1] Strict energy conservation, which is not satisfied automatically due to material and cavity mode dispersion, is relaxed by cross-phase modulation (and in part by self-phase modulation). The parametric gain bandwidth Ω gives the amount by which energy conservation can be relaxed in the process [17, 94]. This bandwidth which scales linearly with the pump power and nonlinear coefficient is also progressively broadened by compressing the minor diameter d (i.e., increasing the aspect ratio D_p/d where D_p is the principal diameter) of the toroidal microcavity, and thereby, in turn, the effective cross-sectional area of the mode. Empirically, $D_p/d > 15$ has proven sufficient to enable parametric oscillation. However, aspect ratio control is only a necessary condition and not a sufficient condition for parametric oscillations. In addition to this geometrical control, cavity loading provided by the waveguide used to couple power both to and from the resonator (and characterized by a coupling parameter $K = Q_0/Q_e$, where Q_0 is the intrinsic quality factor, Q_e is the external quality factor) should also be carefully adjusted. This dependence results because, as noted above, the parametric gain bandwidth scales with the circulating pump power in the cavity and this power can be controlled, in turn, by changing the coupling parameter K. Cavity loading variation should be able to induce transition between parametric and Raman oscillations in a sufficiently phase-matched silica toroidal microcavity. However, this loading-induced control of OPO and Raman oscillation has not been verified in previous experiments [17]. In this chapter, we demonstrate control of oscillation regime (Raman and parametric oscillations) by varying the cavity loading in a toroidal microcavity of fixed, but sufficiently high, aspect ratio. The theoretical explanation for the transition of oscillations will be given in conjunction with actual experiments based on an effective cavity gain theory which includes both the Raman and parametric contributions.

[1] Assuming that pump, signal and idler have azimuthal mode numbers m, $m+k$ and $m-k$, the phase-mismatch is given by $\Delta\beta = 2m/R_e - (m+k)/R_e - (m-k)/R_e \simeq 0$. Here, the same effective radius R_e was used for simplicity. In reality, there will be a slight phase-mismatch induced by the difference in R_e.

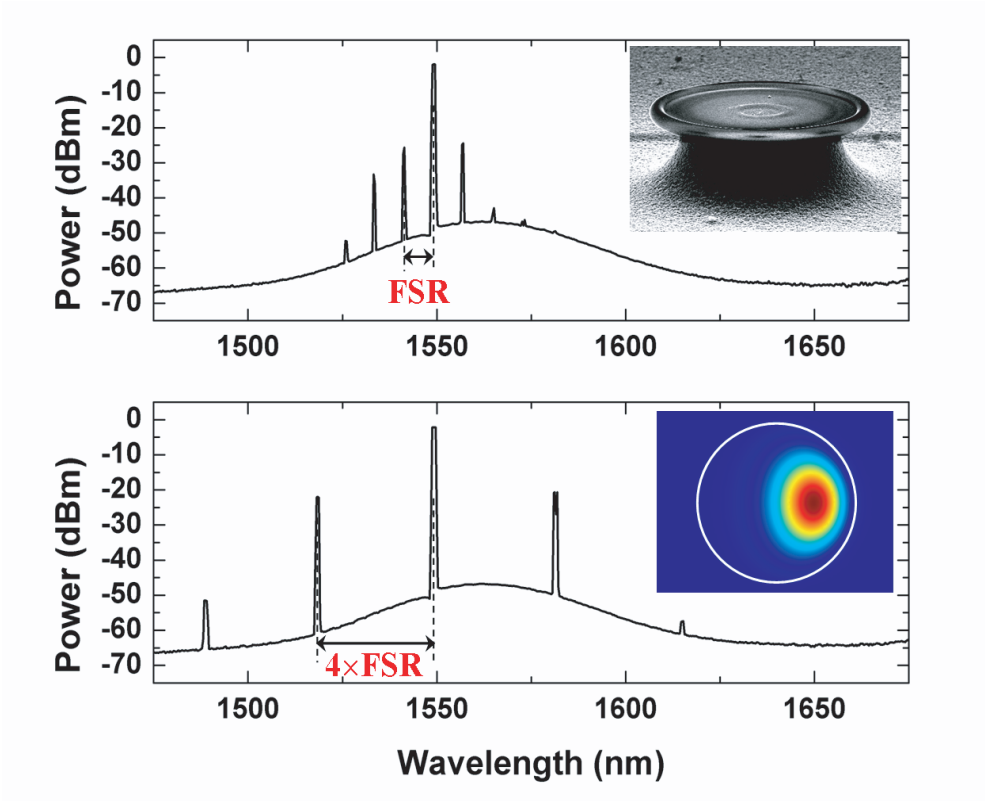

Figure 6.1: Two parametric oscillation spectra measured from the same ultrahigh-Q silica toroidal microcavity with minor (d)/principal (D_p) diameter of 3.8/67 μm ($D_p/d = 17.63 > 15$). The two spectra correspond to a different (horizontal/vertical) tapered fiber position with respect to the toroidal microcavity. Pump wavelength of 1549.2 nm is used for excitation. Insets: SEM micrograph (upper) and theoretical (fundamental mode) intensity pattern (lower) of the toroidal microcavity used for these spectra.

6.1 Parametric oscillation in large-aspect-ratio toroids

Figure 6.1 shows two typical optical spectra of parametric oscillations in an ultrahigh-Q silica toroidal microcavity with minor/principal diameter of 3.8/67 μm (aspect ratio $D_p/d = 17.63$). The insets in Figure 6.1 show scanning electron microscope (SEM) images of the actual toroidal microcavity used in the experiment and the squared electric field (fundamental TE mode) obtained by a finite element modeling (FEM). The two spectra are observed under different loading conditions.[2] Tapered optical fiber of 1-2 μm diameter is mounted on a piezo-controlled translation stage having a resolution of 20 nm and used to couple pump and emission power to/from the toroidal microcavity for the characterization of quality factors and the output spectrum. This coupling mechanism also enables precise control of cavity loading through control of the airgap between the taper and resonator. To resonantly excite the pump mode, a narrow linewidth (<300 kHz), tunable, external-cavity laser was scanned across the pump whispering-gallery mode at a repetition frequency of 100 Hz. In the upper graph, the signal and idler (including the subsidiary signal and idler modes) are shifted by one FSR (free spectral range) from the pump mode. However, as can be seen in the lower spectrum, the lowest threshold signal and idler modes need not be the most adjacent modes to the pump. In certain cases, signal and idler waves offset by $9 \times$ FSR with respect to the pump mode have been observed within the same toroidal microcavity of Figure 6.1. All the signal and idler oscillation wavelengths (including the pump mode) correspond to the fundamental TE modes (which have smaller nonlinear effective mode area than TM modes: $A_{eff}^{TE} < A_{eff}^{TM}$) of the toroidal microcavity and the corresponding FSR for these modes is $\sim$7.8 nm near 1550 nm. The minimum intrinsic Q-factor throughout the experiments was 0.7×10^8.

6.2 Cavity loading induced transitions

Figure 6.2 illustrates two distinct regimes of operation with respect to frequency detuning, defined by $\Delta f = 2f_p - f_s - f_i$. These regimes are observable within the same microcavity by selection of pump wavelength. Frequency detuning, which results from both material

[2]These two spectra are obtained at different tapered fiber positions relative to the equatorial plane of the toroidal microcavity.

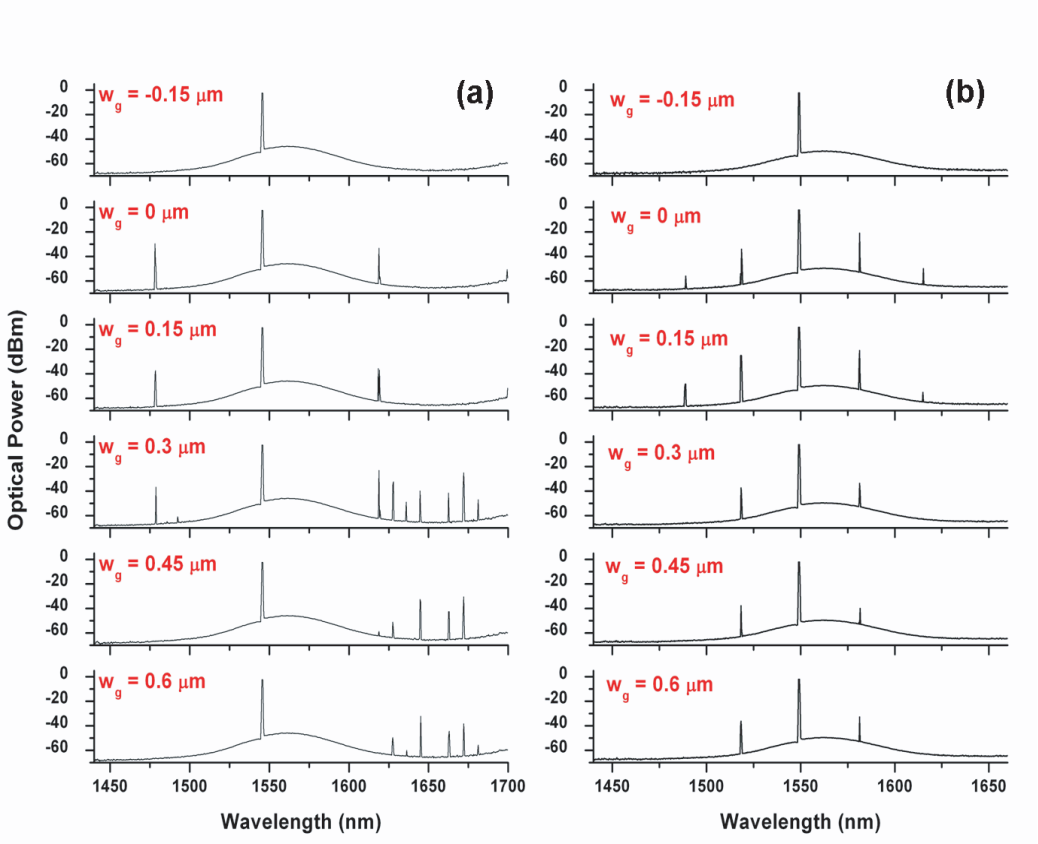

Figure 6.2: (a) Transition between Raman oscillation and parametric oscillation in a toroidal microcavity with larger frequency detuning $\Delta f \sim 13$ MHz. Cavity loading is different in each panel and is varied by adjustment of the airgap (w_g). Airgap values are referenced to the critical coupling point (zero). (b) Toroidal microcavity with smaller frequency detuning $\Delta f \sim 6$ MHz showing parametric-only regimes over a range of loading conditions. As in (a) cavity loading is controlled by adjustment of the taper-cavity gap distance shown in each plot and gap values are given relative to the critical-coupling gap distance. Loading increases in the vertical direction.

dispersion (in this case, thermally-grown silica) as well as cavity mode dispersion (intrinsic FSR changes as a function of wavelength), will vary with wavelength and hence with the pump wavelength. In each graph, input pump power was always fixed below ∼1 mW and only the cavity loading has been changed by varying the tapered fiber position. In Figure 6.2 (a), the transition from Raman oscillation to parametric oscillation (as the cavity loading was varied gradually from undercoupled to overcoupled regimes) is clearly demonstrated for a toroidal microcavity with an estimated frequency detuning of 13 MHz (gap width w_g is plotted relative to the critically-coupled condition: negative and positive values correspond to over- and undercoupled regimes respectively). This kind of transition from Raman to parametric oscillation is a clear signature of intermediate to large detuning frequency values as previously predicted by the minimum threshold selection rule [17]. In contrast to the large detuning case, we observe only parametric oscillation for another detuning condition ($\Delta f = 6$ MHz) shown in Figure 6.2 (b). These data are consistent with a smaller detuning frequency [17]. Although not shown explicitly in Figure 6.2, a Raman-only regime can be observed within the limit of an available pump power from the same toroidal microcavity using a different pump wavelength (and, presumably, large detuning frequency).

6.3 Quantitative analysis on nonlinear effects in microcavities

For a semi-quantitative description of the transition between these two oscillation regimes, the theory of $\chi^{(3)}$-parametric amplification including the competing Raman-effect is adapted to the toroidal micro-resonator geometry [95]. The undepleted pump-power approximation is used and relevant parameters for silica are taken from [95]. For simplicity, the imaginary part of the nonlinear coefficient was assumed to be an odd function of frequency. Figure 6.3 shows the theoretical threshold powers as a function of cavity loading for an ultrahigh-Q silica toroidal microcavity with minor/principal diameter of 3.8/67 μm. Two different frequency detuning values, $\Delta f = 6, 13$ MHz, are assumed for the calculation of parametric oscillation threshold powers. As can be seen in the graph, for small frequency detuning ($\Delta f = 6$ MHz, corresponding to Figure 6.2(a)), the parametric oscillation threshold power is always lower than the Raman threshold. However, for an intermediate frequency detuning

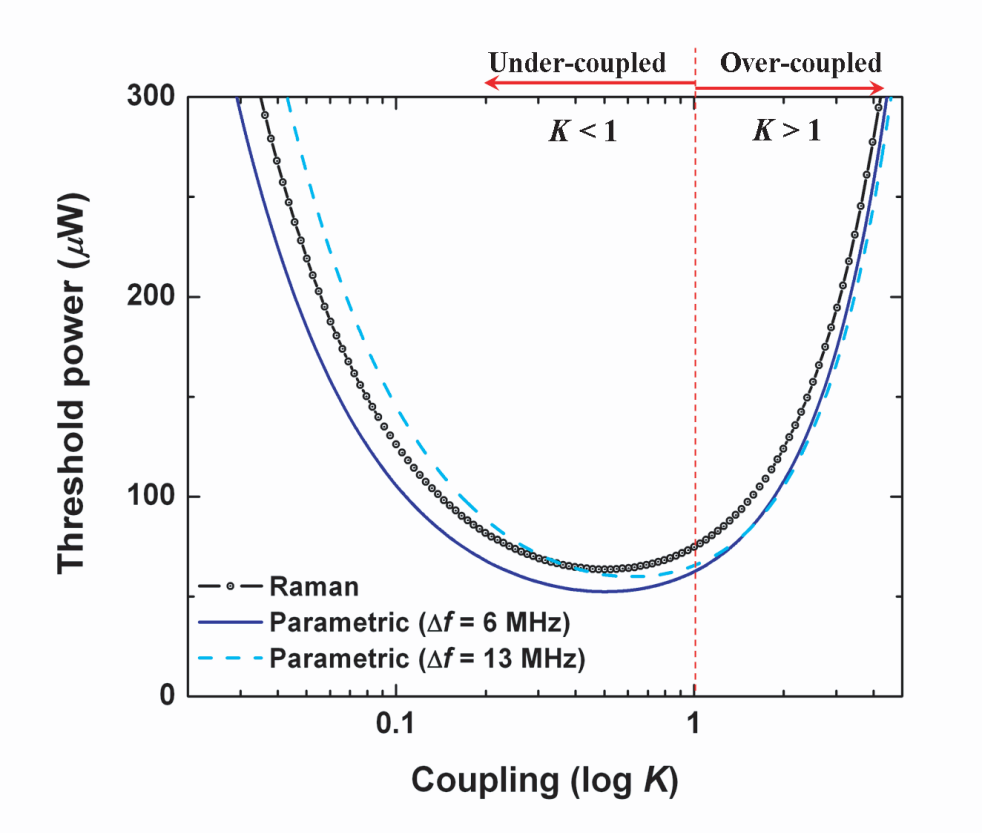

Figure 6.3: Theoretical threshold powers as a function of cavity loading ($K < 1$: under-coupled regime, $K = 1$: critical coupling, $K > 1$: overcoupled regime). Raman oscillation threshold along with parametric thresholds for two different frequency detuning values ($\Delta f = 6, 13$ MHz) are plotted for a toroidal microcavity with principal/minor diameter of 67/3.8 μm. Intrinsic Q-factor of 10^8 is assumed for the analysis.

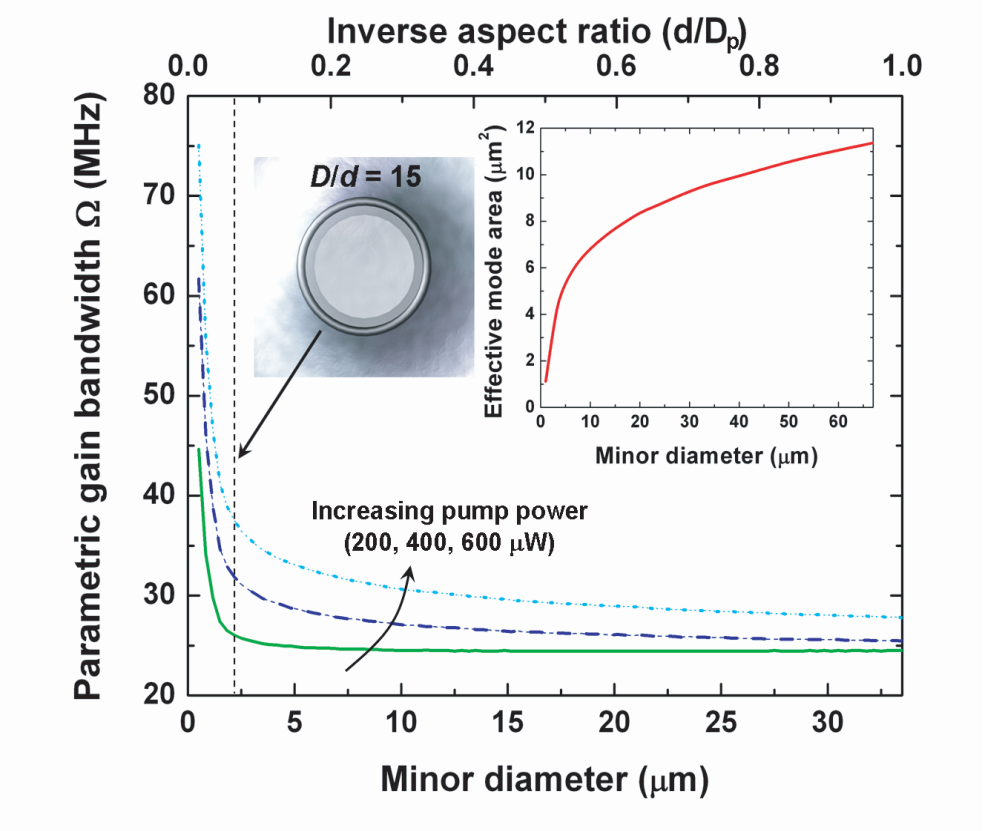

Figure 6.4: Theoretical plot of a parametric bandwidth (defined as a 3 dB effective gain bandwidth) as a function of minor diameter for three different input pump powers. Note a sharp increase in the bandwidth for a larger aspect ratio over ∼15. The inset is a nonlinear effective mode area for a toroidal microcavity with a principal diameter of 67 μm.

($\Delta f = 13$ MHz corresponding to Figure 6.2(b)), the Raman threshold power is lower than the parametric threshold in the undercoupled regime ($K < 0.37$) and becomes higher in the rest of the coupling condition resulting in a transition to the parametric oscillation. The empirical condition $D_p/d > 15$ has also been tested with the effective cavity gain theory. In Figure 6.4, the parametric gain bandwidth is plotted as a function of minor diameter for three different input pump powers. As can be seen in this plot, parametric gain bandwidth increases sharply for a larger aspect ratio exceeding ∼15 thereby confirming the feasibility of the empirical number given in [17].

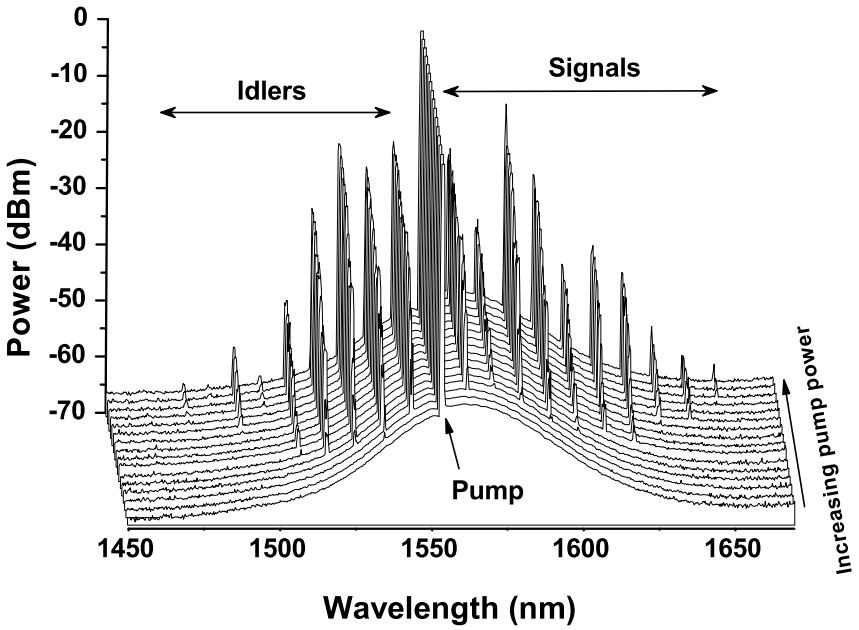

Figure 6.5: Frequency comb generation plotted as a function of input pump power. As the input pump power increases, higher order signal and idler modes are generated.

6.4 Frequency comb generation

For a high-Q toroidal microcavity with very small inverse aspect ratio, regularly spaced frequency comb has been routinely observed due to increased parametric gain bandwidth (Figure 6.4). Figure 6.5 and 6.6 show such a frequency comb generation in the toroidal microcavity and the corresponding LL curves. As input pump power increases ($P < 1$ mW), higher order signal and idler modes are generated. Since the frequency detuning is generally larger for the signal and idler modes far apart, the higher order signal and idlers have higher threshold powers than the lower order signal and idlers.

6.5 Conclusions

In conclusion, a cavity-loading-induced transition between Raman and parametric oscillation in ultrahigh-Q silica toroidal microcavities is demonstrated experimentally and theoretically analyzed using a model that incorporates both Raman and parametric effects. Frequency detuning and cavity loading are shown to play significant roles in the operation of the microcavity nonlinear oscillator in addition to the previously proven method of aspect ratio control. For a toroidal microcavity with large-enough aspect ratio ($D_p/d > 15$), it is possible to observe various oscillation regimes ranging from parametric to Raman in the same toroidal microcavity by direct change of cavity loading conditions or by indirect change of frequency detuning through adjustment of the pump wavelength.

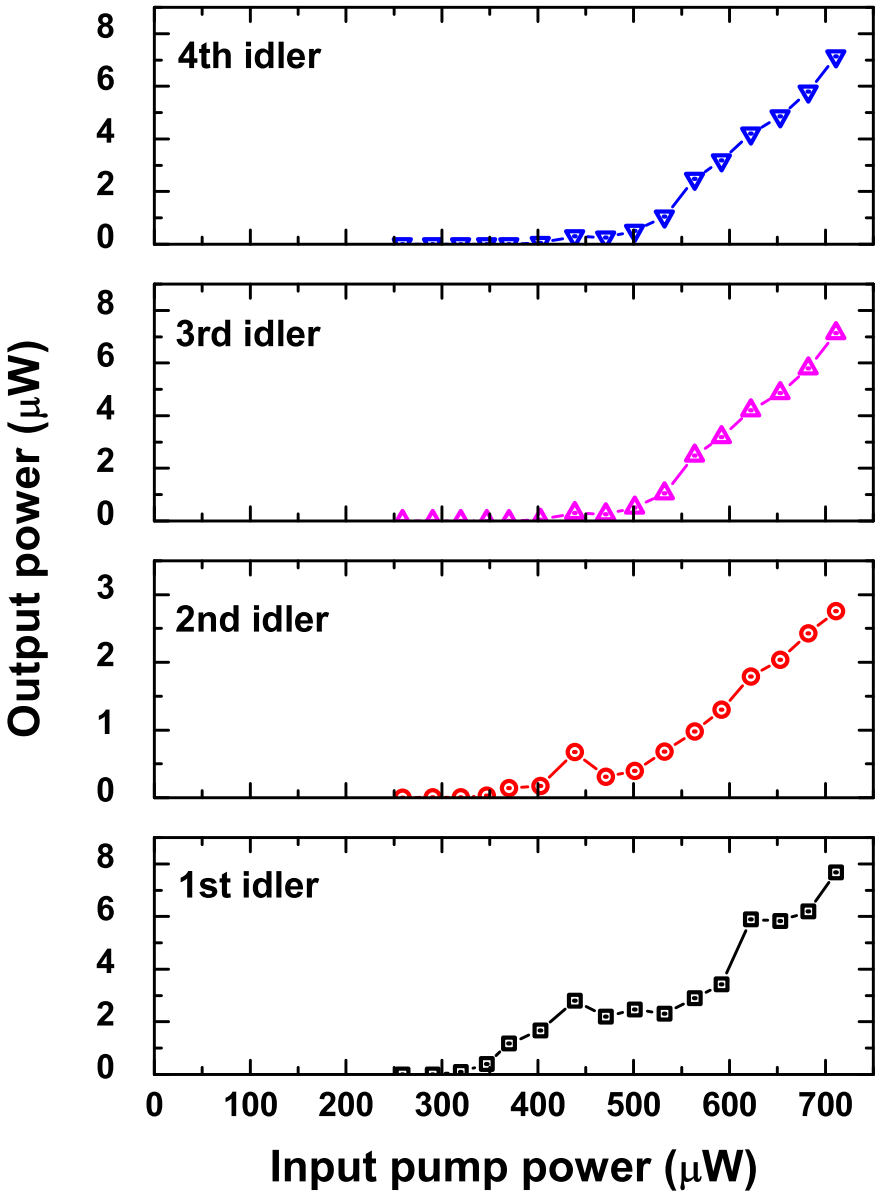

Figure 6.6: Frequency comb generation plotted as a function of input pump power. As the input pump power increases, higher order signal and idler modes are generated.

Chapter 7

Summary

In this thesis, ultrahigh-Q microtoroid on-chip resonators were investigated as low-loss laser cavities. First, to gain a better understanding of the cavity itself, basic properties of the ultrahigh-Q toroidal microcavity were studied. By solving scalar wave equation with a perturbation expansion, the cavity mode field was expressed in closed form with iteratively-obtained cavity parameters. The resonance wavelengths of the toroidal microcavity, which were the solutions of the characteristic equation, were found to be very close to the values obtained by numerical simulations. Cavity mode volume, phase-matching condition, external-Q-factor, and radiative Q-factor were all calculated based on the cavity mode field for a toroidal microcavity with small inverse aspect ratio. The results of the iterative perturbation method were in good agreement with those of numerical prediction performed by finite element method.

In the following chapter, chemically-synthesized nanocrystal, CdSe/ZnS (core/shell), quantum dots were incorporated onto the surface of ultrahigh-Q toroidal microcavities. By pulsed-excitation of quantum dots, either through tapered fiber or free-space, pulsed lasing was observed at room and liquid nitrogen temperature. Use of a tapered fiber coupling substantially lowered the threshold energy when compared with the case of free-space excitation. The reason for this was attributed to the efficient delivery of pump pulses to the active gain region of the toroidal microcavity. Further threshold reduction was possible by quantum-dot surface coverage control. By decreasing the quantum-dot numbers on the surface of the cavity, two benefits were achieved. The transparency-related component of the threshold energy decreases and the cavity Q-factor increases thus lowering threshold energy further down to 9.9 fJ.

Lasing from an erbium-doped high-Q silica toroidal microcavity coupled to a tapered optical fiber is demonstrated and analyzed in chaper 5. Average erbium ion concentrations were in the range 0.009-0.09 at. % and a minimum threshold power as low as 4.5 μW and a maximum output lasing power as high as 39.4 μW are obtained from cavities with diameters in the range 25-80 μm. Controlling lasing wavelength in a discrete way at each whispering-gallery modes was possible by changing the cavity loading, i.e., the distance between the tapered optical fiber and the microcavity. Analytic formulas predicting threshold power, differential slope efficiency are derived and their dependence on cavity loading, erbium ion concentration and Q-factor is analyzed. It is shown that the experimental results are in good agreement with the derived formulas.

The nonlinear oscillation in the toroidal microcavity is investigated in the next chapter. Especially, a controllable and reversible transition between parametric and Raman oscillation in an ultrahigh-Q silica toroidal microcavity is experimentally demonstrated and theoretically analyzed. By direct change of cavity loading and indirect adjustment of frequency detuning, parametric and/or Raman oscillation can be accessed selectively without modification of cavity geometry in a toroidal microcavity with large enough aspect ratio. Based on an effective cavity gain theory, this transition is analyzed in terms of cavity loading and frequency detuning leading to a better understanding of the combined effects of parametric and Raman processes in silica microcavities.

Appendix A

Tuning of High-Q Toroidal Microcavities

Ultrahigh-Q optical microresonators represent a distinct class of microcavities [14] with applications ranging from optical communications and biosensing [19] to fundamental studies of nonlinear optical effects [15, 16, 96, 97] and cavity quantum electrodynamics (cQED) [12]. Although wafer-scale tuning control has been available for devices operating in the Q regime below 10^5, such methods have not been available in the ultrahigh-Q regime, where Q can exceed 100 million. Nonetheless, there remains keen interest in finding more practical ways to implement tuning control in this regime [98,99]. In this Appendix, we introduce electrical control of resonant frequency in an ultrahigh-Q microtroroid by themooptic tuning. The significance of this result is that this represents the first example of an ultrahigh-Q microresonator with "integrated" electrical tuning. By including only two additional processing steps (lithography and metalization) into the prior fabrication process for the ultrahigh-Q microtoroids, electrical control is implemented. The end result is a highly reproducible process through which chip-based electrically tunable microtoroids with Q-factors in excess of 100 million are fabricated. Furthermore, since the devices themselves are fabricated on a silicon substrate and significant tuning range at subvolt levels is demonstrated, the integration of complementary metal-oxide-semiconductor (CMOS) control circuitry with the devices is also possible. In addition to characterizing the static tuning characteristics of these devices, we also investigate their dynamic response including the use of a helium ambient atmosphere to isolate the specific source of the tuning time constant.

The fabrication process with the exception of metalization steps is described in detail elsewhere [23]. Briefly, it proceeds as follows (see Figure A.1). First, photolithography is

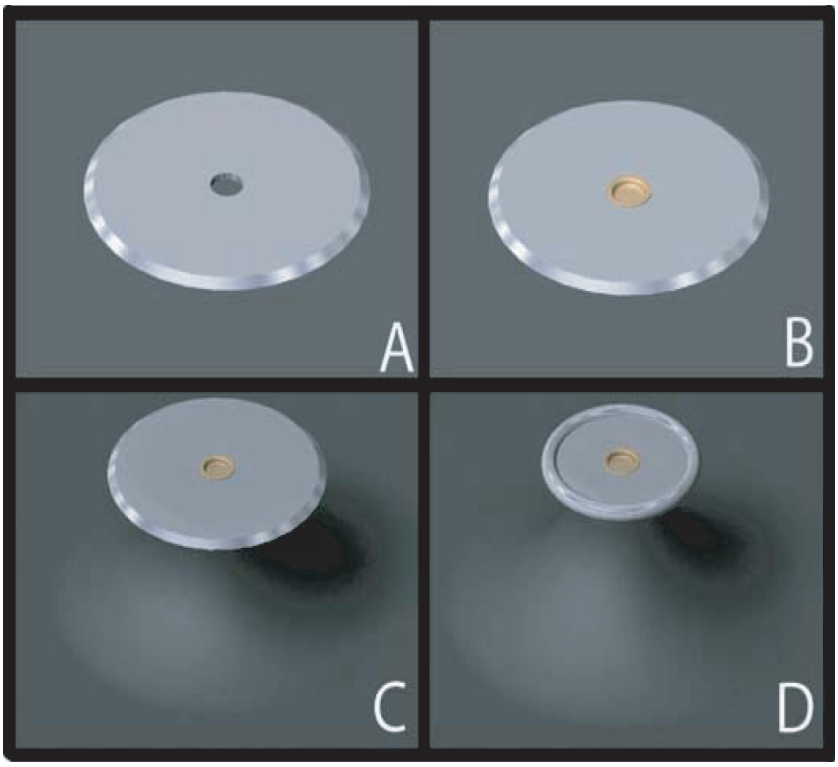

Figure A.1: Fabrication process flow outline for the tunable microtoroid resonators. (a) Oxide is lithographically defined and etched leaving oxide disks. (b) Metalization via evaporation on both sides of the wafer in order to create the electrical contacts. Ohmic contacts are formed by annealing in a nitrogen ambient at 500°C in a tube furnace. (c) The wafer is isotropically etched using XeF_2. (d) The oxide disks are exposed to a CO_2 laser in order to reflow the disks, creating the tunable UHQ microtoroids.

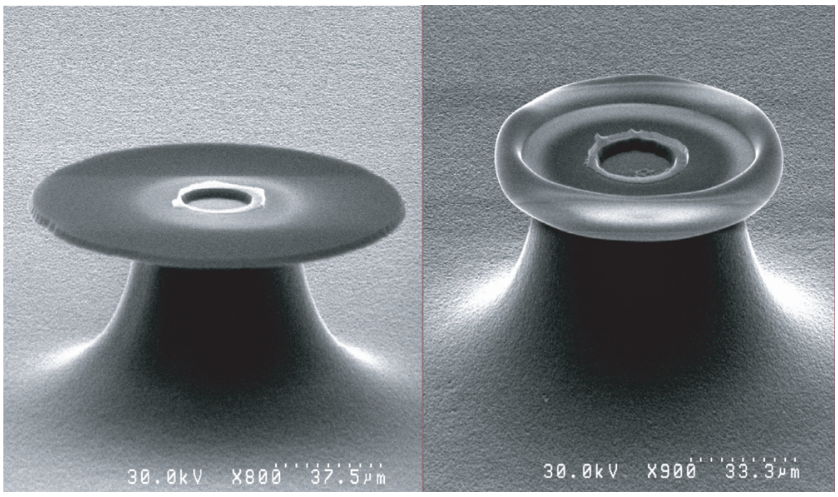

Figure A.2: Scanning electron micrographs of tunable disk and toroidal microresonators.

performed on a highly p-doped (0.001-0.006 Ω·cm) silicon wafer with a 2 μm thick thermal oxide. The unexposed photoresist is used as an etch mask during immersion in buffered HF. These two steps define oxide disks of 100 μm diameter with a 25 μm wide contact hole concentrically located on the disk. All oxide on the backside of the wafer is also removed. A second photolithography step is performed in order to define a metal lift-off mask. 1000 $\mathring{A}$ of aluminum are thermally evaporated on both sides of the wafer in sequential deposition steps. The wafer is then immersed in acetone overnight releasing the excess aluminum and leaving aluminum contacts in the center of the oxide disks as well as the backside of the wafer. Ohmic contacts are formed by annealing the wafer in a tube furnace at 500°C in a nitrogen ambient. The remaining oxide disks act as etch masks during exposure to xenon difluoride (XeF_2) gas at 3 torr. Xenon difluoride isotropically etches the silicon substrate leaving the perimeter of the silica disk isolated from the higher index silicon. To eliminate lithographic blemishes along the perimeter of the oxide, each microdisk is orthogonally exposed to a CO_2 laser beam resulting in surface tension induced reflow and formation of the microtoroid [23]. During this process the central region of the pillar is unaffected and therefore the aluminum contact remains pristine. The resulting device possesses a surface finish with near atomic roughness in addition to integrated metal contacts (Figure A.2).

The tuning range and frequency response of the tunable microtroid resonators were measured in the optical telecommunication band (1550 nm). To create a low resistivity electrical path, the substrate (now containing an array of microtoroids on one side) was placed on a metal, electrically-grounded platform mounted to a three-axis stage with a 100 nm step resolution. The stage allowed the substrate to move freely so that the taper waveguide could couple to a single microtoroid. Two microscopes were used to simultaneously image the microtoroid from both the top and side. Optical power was coupled to the disk using a tapered fiber waveguide [91]. The tapered fiber was formed by stretching a standard optical fiber (SMF-125) while heating it with a hydrogen flame. As the adiabatic condition is maintained during the stretching process, the resulting tapered fiber exhibits losses typically less than 5%. Further details regarding tapered fiber fabrication and properties are provided elsewhere [25, 26]. It should be noted that during characterization of both tuning range and frequency response the microtoroid and fiber taper waveguide were in contact to prevent any thermally-induced loading variations. With the taper and microtoroid in

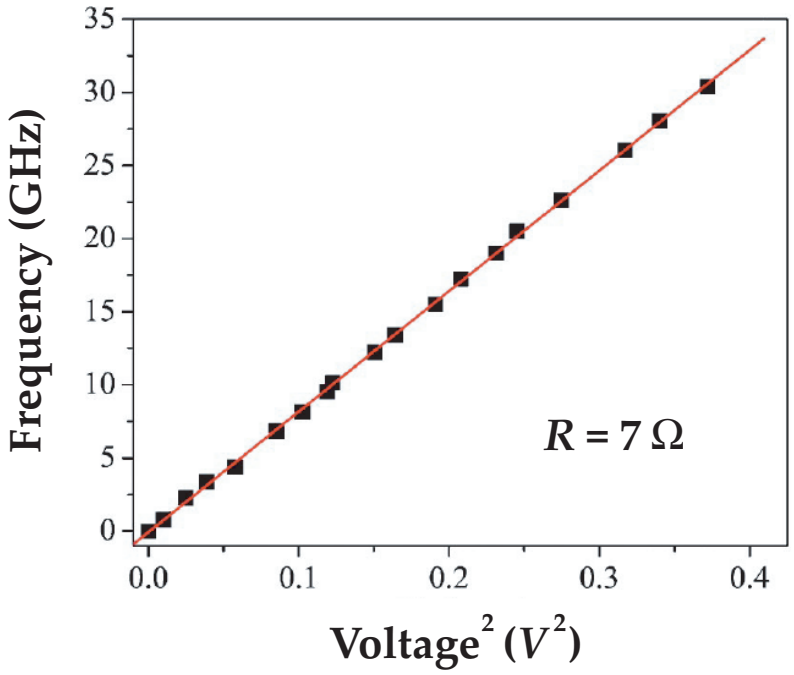

Figure A.3: Resonance frequency shift versus voltage. The quadratic coefficient is 85.56 GHz/V^2.

contact, the aluminum pad on top of the microtoroid is electrically contacted and voltage is applied while the silicon substrate is grounded. Typical electrical resistance of the devices were consistently less than 10 Ω. The induced ohmic heating and rise in temperature that occured in the silicon pillar was thermally conducted to the silica microtoroid, subsequently increased the temperature of the silica in the path of the optical whispering-gallery mode. This temperature increase resulted in a frequency shift of the resonant frequencies.

The tuning rate and tuning range were determined by scanning a single-frequency, external-cavity laser (coupled to the tapered fiber waveguide) across a frequency span of approximately 50 GHz and in the spectral vicinity of a high-Q resonance. Transmitted power through the taper was monitored on an oscilloscope during scanning to measure tuning. With the laser continuously scanning, voltage was incrementally applied to the microtoroid resonator. Figure A.3 shows an example of a typical tuning curve for a microtoroid resonator with a resistance of 7 Ω and tuning rate of 85 GHz/V^2. The tuning is plotted against V^2 in order to stress the dependence of tuning on applied electrical power (V^2/R).

The frequency response characteristics were measured by first tuning the laser near

a resonance, and simultaneously a function generator was used to apply a small-signal sinusoidal modulation voltage. A lock-in analyzer was set up to detect the modulation induced in the optical power transmission and was referenced to the modulation frequency of the function generator. The frequency response of the tunable microtoroid resonators in both air and helium was measured and is plotted in Figure A.4. The measured frequency response contains features consistent with the existence of a single, low-frequency pole. There are several possible cooling mechanisms which could account for this single, low frequency pole. The authors postulate that the primary cooling mechanism should exhibit a dependence on the coefficient of thermal conduction of ambient atmosphere around the resonator. To confirm this hypothesis, the frequency response was measured while helium gas was introduced into the testing chamber. As can be seen in Figure A.4, the corner frequency doubled in the presence of helium, a result of helium being five times more thermally conductive than air.

In summary we have demonstrated the ability to electrically tune ultrahigh-Q microresonators on a chip. Furthermore, tuning ranges as large as 300 GHz have been observed. The corner frequency of the tuning process was measured to be 330 Hz in air and is attributed to thermal dissipation to the ambient. Moreover, an understanding of the cooling processes associated with the corner frequency was demonstrated by introducing helium into the air ambient and observing the resulting increase in corner frequency. While not suitable for high-speed applications, such a device has several important applications. The ability to tune nearly one full free spectral range makes the tunable microtoroids ideal for use as an tunable optical filter or as a tunable laser source [36, 78, 100–102] based on the ultrahigh-Q properties. Tuning is also an essential feature in application of ultrahigh-Q devices to cQED [12]. Additionally, the ability to detect small change in its ambient surroundings can lead to applications in both biosensing and gas detection. Finally, tunable microtoroid resonators would be well suited for the realization of CROW devices [102].

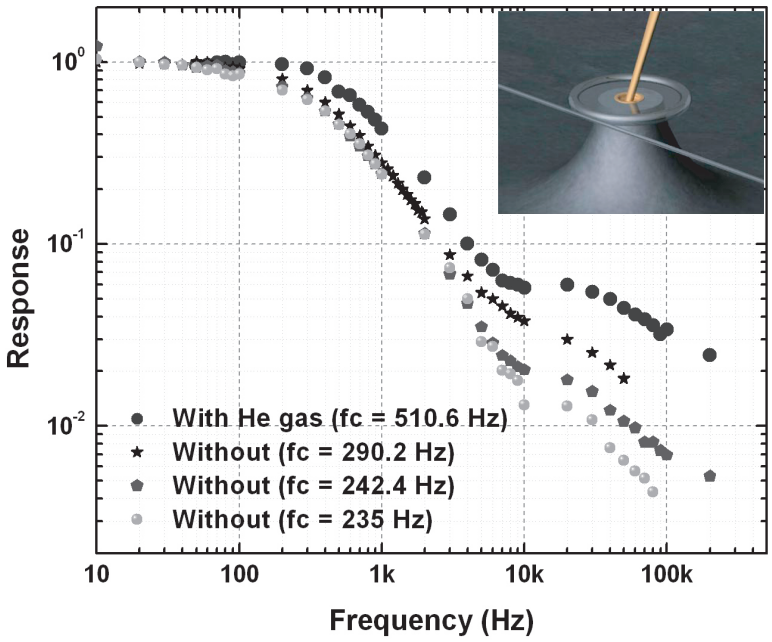

Figure A.4: The frequency response of the tunable microtoroid resonators in both air and helium ambient atmospheres. Inset: a rendered depiction of the tunable microtoroid device coupled to a tapered optical fiber while being contacted by a metal probe.

Appendix B

Cascaded Raman Spherical Microcavity Lasers

Cascaded Raman lasers have been of considerable interest as a means of extending the wavelength range of existing laser sources. Demonstrations of cascaded Raman (Stokes) lasing in both fiber-based Bragg grating resonator [93] media and bulk-crystal active media [103] have been realized. Recently, a microcavity-based Raman laser with an ultrahigh-Q silica microsphere was demonstrated [15]. In addition to being both compact and efficient, this device features pump and signal coupling directly to optical fiber, a significant advantage in practical applications. In this Appendix, we report the first observation to our knowledge, which can achieve as high as fifth-order Raman lasing with submilliwatt pump powers. To our knowledge these devices are both the smallest fiber-compatible cascade devices ever reported and the most efficient in terms of their threshold, exhibiting threshold powers that are more than 2 orders of magnitude lower than those of cascaded operation of Raman lasers based on fiber Bragg gratings [93]. The whispering-gallery modes (WGMs) of microspheres fabricated from fused-silica have achieved one of the highest Q-factors (8×10^9) to date [82]. Ultrahigh-Q combined with the small mode volume ($\sim$1000 μm^3 in this work) allow resonant buildup of very high circulating intensities, thereby significantly reducing the threshold for stimulated nonlinear processes. These properties of high-Q WGMs were first demonstrated in the pioneering work of Qian [104] and Lin [105] concerning nonlinearities in micro-droplets, including the observation of Raman cascading up to 14th order [104]. However, the required pump power in these experiments was large (typically several watts) owing to inefficient modal excitation provided by free-space illumination. Modal excitation with fiber tapers, on the other hand, allows excitation of a single WGM with ultralow

coupling loss [25], thereby drastically improving the overall efficiency while providing convenient access to the technologically important fiber-transport medium. As demonstrated here, the use of tapered optical fibers also allows precise measurements on the higher-order Stokes waves.

The microsphere resonator modes are modeled as coupled harmonic oscillators with external input field and nonlinear Raman terms [30, 37, 80, 106]:

$$\frac{da_0}{dt} = -\frac{1}{2\tau_0}a_0 + i\kappa_0 s - \frac{\omega_0}{\omega_1}g_1 a_0|a_1|^2, \tag{B.1}$$

$$\frac{da_j}{dt} = -\frac{1}{2\tau_j}a_j + g_j a_j|a_{j-1}|^2 - \frac{\omega_j}{\omega_{j+1}}g_{j+1}a_j|a_{j+1}|^2, \quad (j = 1, 2, \ldots, N-1) \tag{B.2}$$

$$\frac{da_N}{dt} = -\frac{1}{2\tau_N}a_0 + g_N a_N|a_{N-1}|^2, \tag{B.3}$$

where a_j is the slowly-varying cavity field amplitude of the jth Stokes wave, τ_j and g_j are the corresponding photon lifetime [30, 37] and Raman gain coefficient (proportional to the bulk Raman gain coefficient g_R^B) [15],[1] s is the input pump field amplitude ($|s|^2 = P_{in}$: input pump power), and κ_j is the coupling coefficient [37]. In a steady-state, recursion relations are obtained where the initial starting term is taken as the $(N-1)$th clamped intracavity Stokes energy. With these recursion relations the intracavity Stokes energies of all orders in the microsphere can be solved iteratively. Then, even- and odd-order (highest) Stokes output powers are given by the following expressions where the parameter α_j is introduced for simplicity (defined by $\alpha_j \equiv 1/(2\tau_j)$):

$$\begin{aligned} P_N &= |\kappa_N|^2|a_N|^2 \\ &= \frac{|\kappa_0|^2|\kappa_N|^2}{g_0^2\left(\sum_{k=0}^{N/2}\frac{\alpha_{N-2k}}{g_{N-2k}}\right)}P_{in} - |\kappa_N|^2\sum_{k=0}^{N/2}\frac{\alpha_{N-(2k-1)}}{g_{N-(2k-1)}} \quad (N \text{ even}), \end{aligned} \tag{B.4}$$

$$\begin{aligned} P_N &= |\kappa_N|^2|a_N|^2 \\ &= \frac{|\kappa_0|^2|\kappa_N|^2}{g_0^2\left(\sum_{k=0}^{(N-1)/2}\frac{\alpha_{N-2k}}{g_{N-2k}}\right)^{1/2}}\sqrt{P_{in}} - |\kappa_N|^2\sum_{k=1}^{(N+1)/2}\frac{\alpha_{N-(2k-1)}}{g_{N-(2k-1)}} \quad (N \text{ odd}). \end{aligned} \tag{B.5}$$

These equations show that even-numbered, highest-order, Stokes lasing power increases

[1] The relation between g_j and g_R^B is given by $g_j = (\lambda_1/\lambda_j)[c^2/(2n^2V_{eff})]g_R^B$. For simplicity the mode volume V_{eff} is assumed to be independent of wavelength.

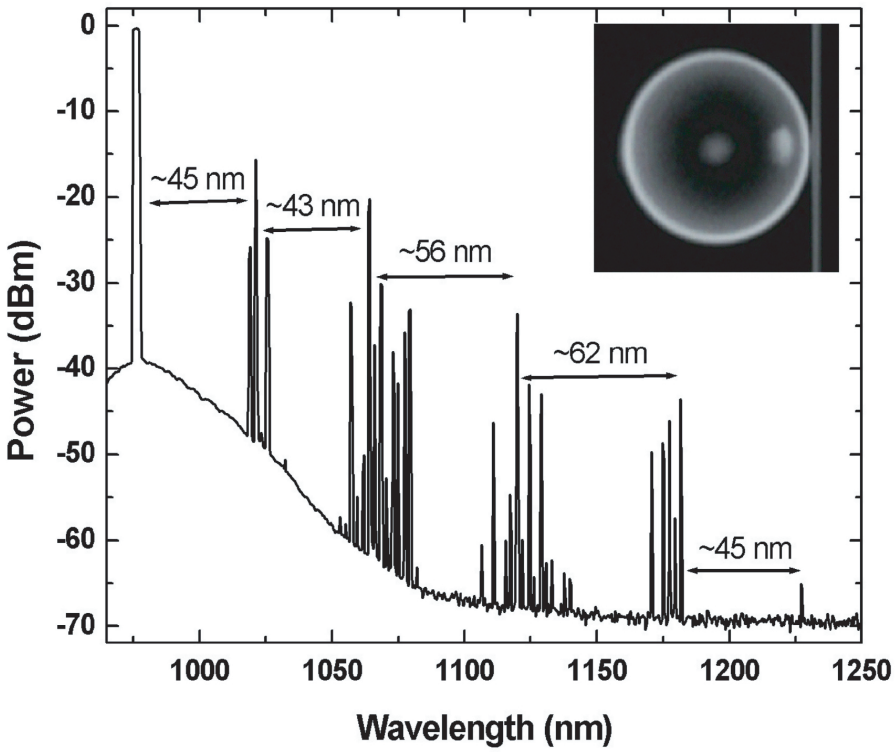

Figure B.1: Typical emission spectrum of the microsphere cascaded Raman laser. The pump wavelength is at 976.08 nm. Inset: optical micrograph of a microsphere taper system used in the experiment.

linearly with input pump power whereas for the odd-numbered case power increases in proportion to the square root of input pump power. Analysis also shows that for an odd number of Stokes lasing lines, all of the even-numbered Stokes lines are clamped and vice versa. From the relation between g_j and g_R^B, the threshold pump powers for the highest-order Stokes lasing lines can be derived as follows:

$$P_{th} = \frac{\pi^2 n^2}{\lambda_0 \lambda_1} \frac{V_{eff}}{g_R^B} \left(\sum_{k=0}^{N/2} \frac{1}{Q_{T,N-2k}} \right)^2 \sum_{k=1}^{N/2} \frac{Q_{ext,0}}{Q_{T,N-(2k-1)}} \quad (N \text{ even}), \tag{B.6}$$

$$P_{th} = \frac{\pi^2 n^2}{\lambda_0 \lambda_1} \frac{V_{eff}}{g_R^B} \left(\sum_{k=1}^{(N+1)/2} \frac{1}{Q_{T,N-(2k-1)}} \right)^2 \sum_{k=0}^{(N-1)/2} \frac{Q_{ext,0}}{Q_{T,N-2k}} \quad (N \text{ odd}), \tag{B.7}$$

where n is the refractive index of the microsphere, $Q_{ext,0}$ is the external quality factor at the pump wavelength and $Q_{T,j}$ is the loaded quality factor at the jth Stokes wavelength.

Figure B.1 shows a typical spectrum of a microsphere cascaded Raman Stokes laser ex-

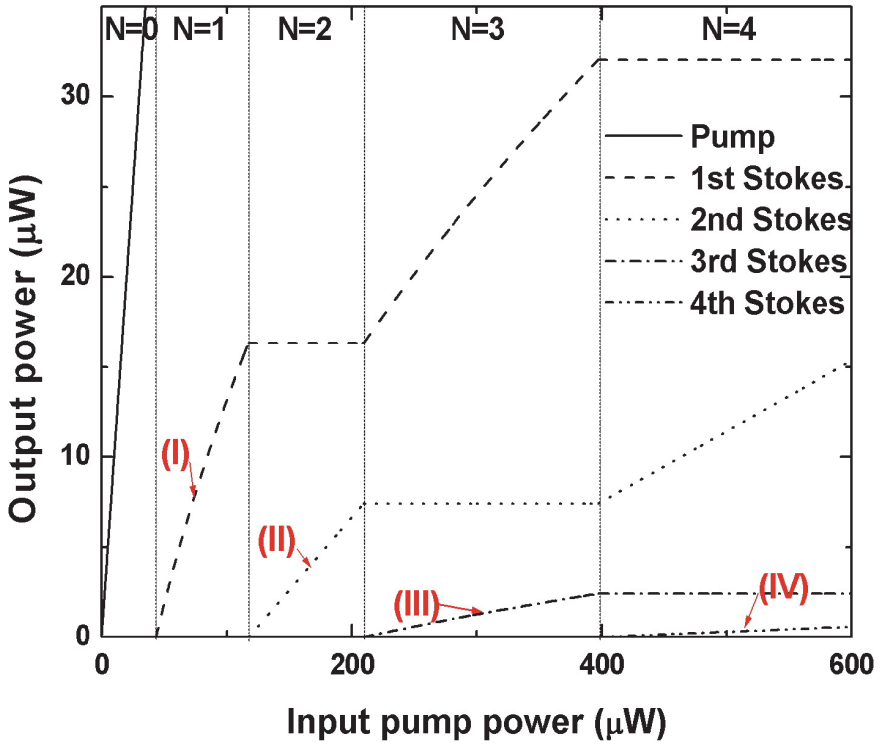

Figure B.2: Theoretical plot of output Raman Stokes power as high as fourth order.

cited by a tunable, narrow linewidth (<300 kHz), external-cavity laser near the wavelength of 980 nm. The output Stokes lasing was highly multimode because of the large Raman gain bandwidth and the small free spectral range (FSR) of the microspheres involved in this study. To characterize the conversion of power from the pump mode to the higher-order Stokes lines, the peak output Stokes power was measured while the high-Q resonance at the pump wavelength was repeatedly scanned with a function generator. The microspheres tested ranged in diameter from 50 to 60 μm and a fiber taper with a waist diameter of 1-2 μm was used for excitation of the fundamental $l = m$ and near-fundamental whispering-gallery modes. The loaded Q-factor at the pump wavelength was estimated to be in the range of 10^7-10^8 as determined by linewidth measurement. The inset in Figure B.1 is a micrograph showing the microsphere tapered-fiber system.

Figure B.2 is a theoretical plot of cascade output powers versus pump power based on Eqs. (B.4) and (B.5). Here the pump wavelength is 980 nm; the intrinsic Q-factors for each Stokes wavelength is assumed to be 1.5×10^8; the microsphere and the fiber taper

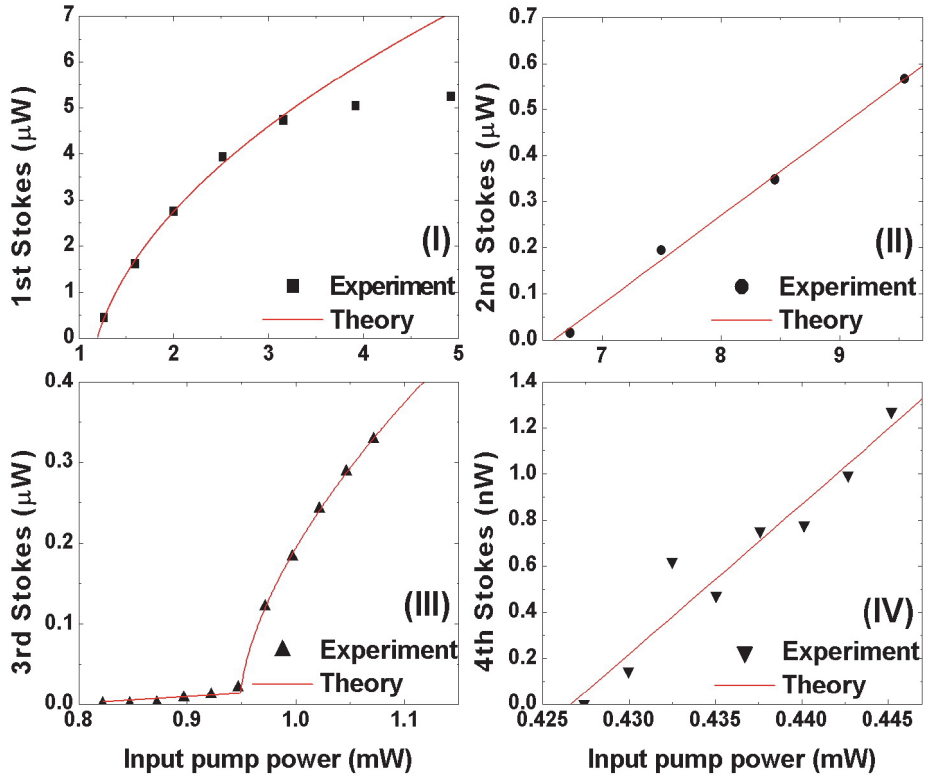

Figure B.3: Stokes lasing powers (first, second, 1550 nm pumping; third, fourth, 980 nm pumping) versus input pump power. Each data set corresponds to measurements taken with a different sphere.

diameters are 60 μm and 1 μm, respectively; and the gap distance between the microsphere and the fiber taper is set to the critical coupling point (0.253 μm) at the pump wavelength. The external Q-factors are calculated according to the formula given in [80]. Figure B.3 shows the measured output versus input power relations as high as fourth order. Each data set is taken when the order presented is the highest order in the spectrum. The data exhibit the theoretically predicted behavior that odd-numbered lines increase proportional to the square root of input pump power, whereas even-numbered lines vary linearly with input pump power (corresponding regions in Figure B.2 are indicated for comparison). Figure B.3 (upper left panel) also shows the clamped response for onset of a next-order Stokes laser line. As a general comment, quantum efficiencies in these data sets were made intentionally low (and thresholds high) by operation in the undercoupled regime. This enabled more consistent data collection because small changes in the taper-sphere gap induce a less abrupt power variation in the undercoupled regime than in the overcoupled regime. In addition, multimode operation of the microsphere laser, particularly at the shorter pump wavelength, reduced single-line quantum efficiency further. A differential quantum efficiency (unidirectional) of 6.48% was observed for the first order Stokes lasing using 980 nm band pumping.

Figure B.4 shows the measured threshold pump power versus taper-sphere gap distance for several Stokes lines. A single sphere was used for all measurements and the gap distance was controlled using a piezo motor having a step size of 20 nm. The observed dependence of the minimum-threshold gap on Stokes order is attributed to a dependence of Q_{ext} and Q_0 on wavelength. The external quality factor Q_{ext} is dependent on the wavelength through the phase matching condition (in the experiment, the fiber diameter was controlled to achieve effective phase match at the pump wavelength). The theoretical fit is made by assuming the external Q-factor is in the form of an exponential function of the gap distance [80].

The two plots in Figure B.5 show the measured threshold dependence on the Stokes order for two different microspheres (each plot taken using a single sphere). In this measurement the loading conditions were optimized for each data point by adjusting the taper-sphere gap. The asymptotic threshold pump power dependence on the Stokes order (as the Stokes order increases) can be inferred from Eq. (B.6) and (B.7) to be a cubic function of the Stokes order, assuming all the loaded Q-factors are the same at each wavelength. The

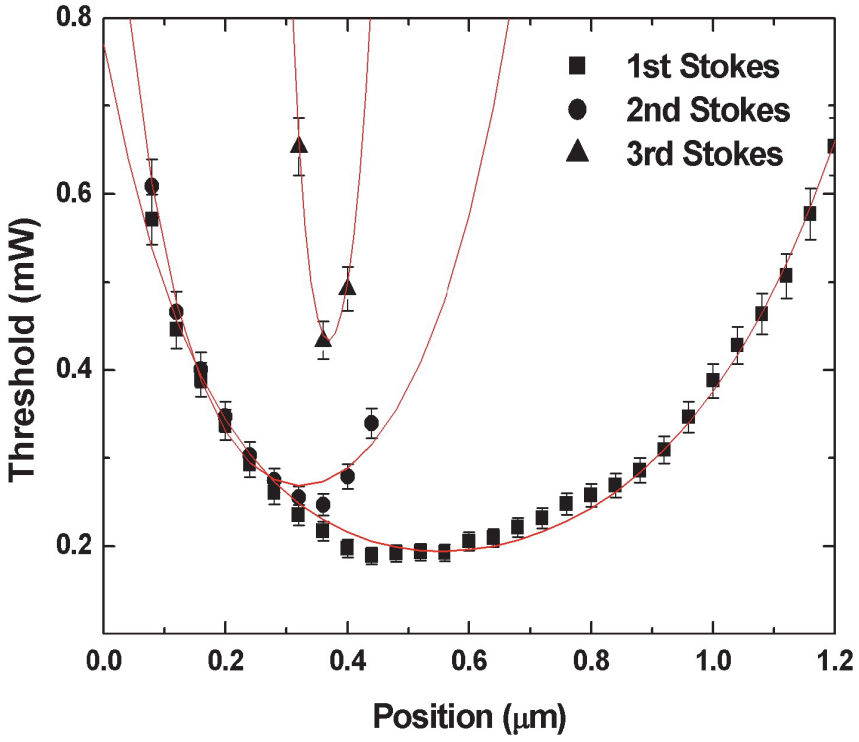

Figure B.4: Threshold pump power versus the gap distance for various Stokes orders (sphere-taper contact location was set at 0 μm).

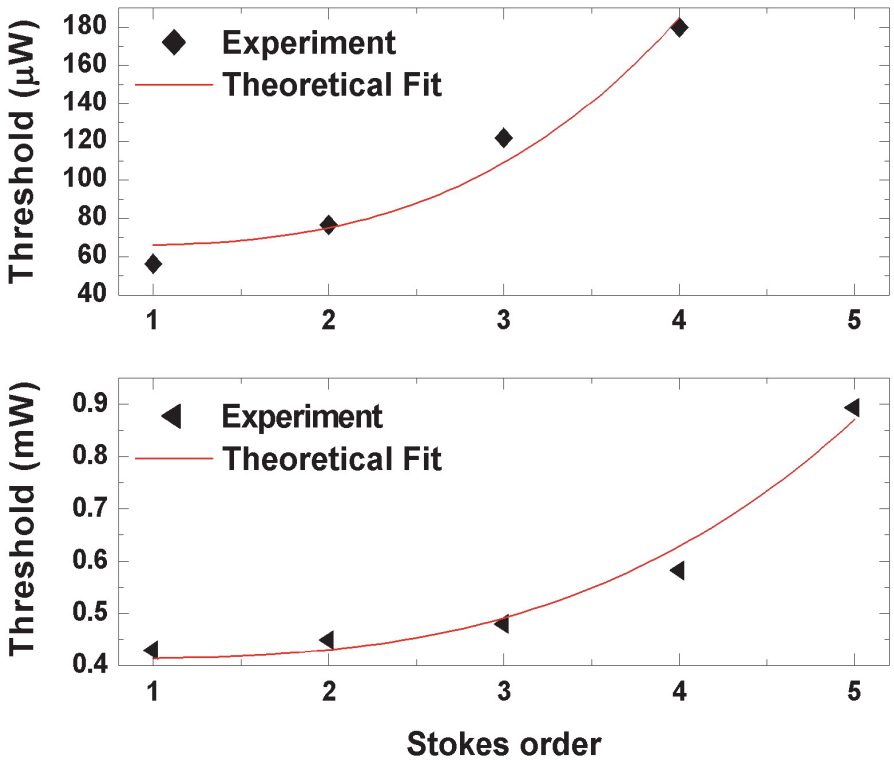

Figure B.5: Threshold pump power versus Stokes order and theoretical curve (solid curve) for two different spheres.

experimental results in Figure B.5 confirm this cubic dependence; in addition, one point in this data exhibited a record-low threshold pump power of 56.4 μW for onset of first-order Stokes lasing (upper panel in Figure B.5). Furthermore, the data show a record threshold for cascaded operation more than 2 orders of magnitude lower than for fiber Raman cascaded lasers [93].

In conclusion, we have demonstrated cascaded Raman lasing in an ultrahigh-Q microsphere coupled to a tapered optical fiber. Raman Stokes lasing as high as fifth order was observed with submilliwatt pump power. The threshold power for the first Stokes line lasing was as low as 56.4 μW. Even- and odd-numbered Stokes lasing lines exhibited different output power versus input pump power relations in agreement with theory. The threshold power was observed to follow an approximate cubic dependence on the order, as predicted by theory.

Appendix C

Fabrication of $LiNbO_3$ Disk Structures by Layer Transfer Method

Recently, ferroelectric materials have found extensive application in microelectronics, microeletromechanical system (MEMS) and electro-optics device applications [107]. Ferroelectric oxides have been used as modulator, resonator, piezoelectric components, infrared-detector elements, and as memory elements, as well as in acoustic delay lines, data processing, and microwave tunable devices. In these applications, the integration of ferroelectric thin films onto planar structures and Si substrate is an important technological issue. Use of thin film ferroelectric oxide layers can reduce device operating voltages and allow monolithically integrated devices. $LiNbO_3$ is a well known nonlinear optical crystal and has an extraordinary spontaneous polarization (71 $\mu C/cm^2$). $LiNbO_3$ optical waveguides also exhibit unusual physical properties and are of great importance for electro-optic applications [108, 109]. Direct wafer bonding and layer transfer techniques are promising methods to fabricate high quality single crystal thin films without the need for heteroepitaxial growth and problems associated with lattice mismatch between silicon substrate and ferroelectric thin film. Implantation-induced layer transfer processes have been reported for the layer transfer of Si, InP, Ge and diamond [110, 111]. Recently, layer splitting and transfer of the ferroelectric materials such as $LiNbO_3$, $LiTaO_3$, $KTaO_3$, $SrTiO_3$ and $BaTiO_3$ also have been reported by sacrificing wet etching and anodic bonding methods combined with crystal ion slicing (CIS) method [112–117]. However, because of large mismatch of coefficient thermal expansion (CTE) between $LiNbO_3$ (7.5-14.4$\times 10^{-6}$ m/°C depending on cutting

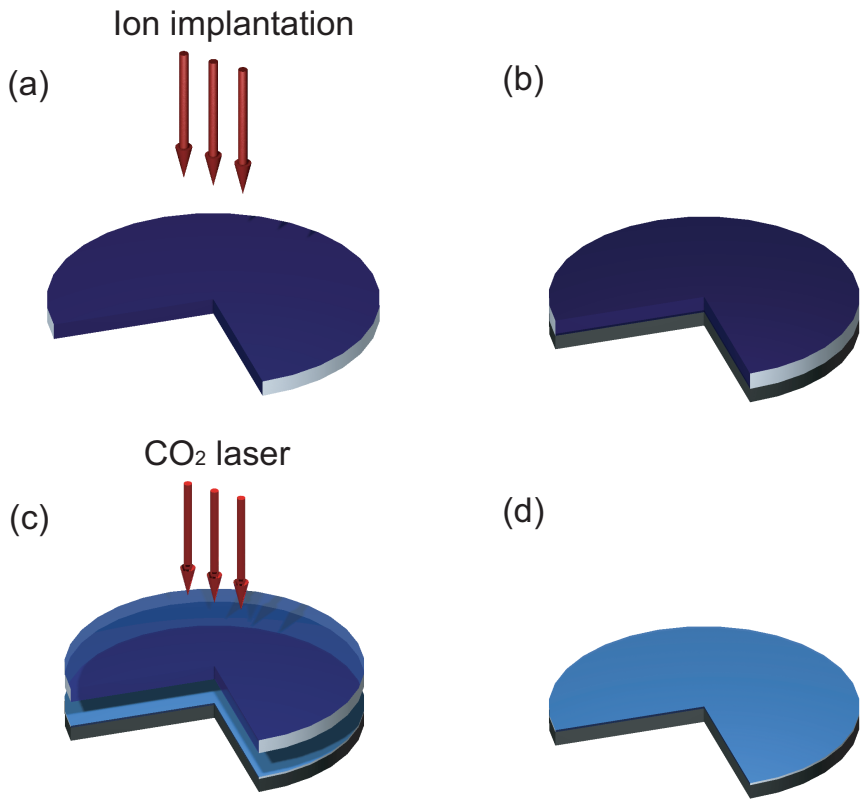

Figure C.1: Layer transfer process; (a) Ion implantation thorough donor bulk crystal, (b) wafer bonding process, (c) laser irradiation using $\lambda = 10.6$ μm CO_2 laser and (d) transferred layer on Si substrate.

orientations) and Si (2.6×10^{-6} m/°C) at high temperature (>400 °C), thermal mismatch-induced stress at the interface of the $LiNbO_3$/Si during the heating and cooling processes even in direct bonding/layer transfer processes is quite large compared with other material systems and this complicates layer transfer and bonding processes for the device integration of the $LiNbO_3$ on the Si. Laser-lift off (LLO) and laser-induced forward transfer methods have been widely investigated to yield PZT, GaN and Si thin films using an excimer laser irradiation with inter-metallic bonding layer (PdIn) as the metallic adhesive layer [118–120]. However, for the microphotonic device applications anticipated in this study, $LiNbO_3$ thin film needs to be directly formed on the Si without any metallic adhesive layer. In this Appendix, we introduce a novel method, laser-induced layer transfer in conjunction with ion implantation to integrate single crystal $LiNbO_3$ thin film with silicon.

Figure C.1 represents overall processes. Light ions such as hydrogen and helium are im-

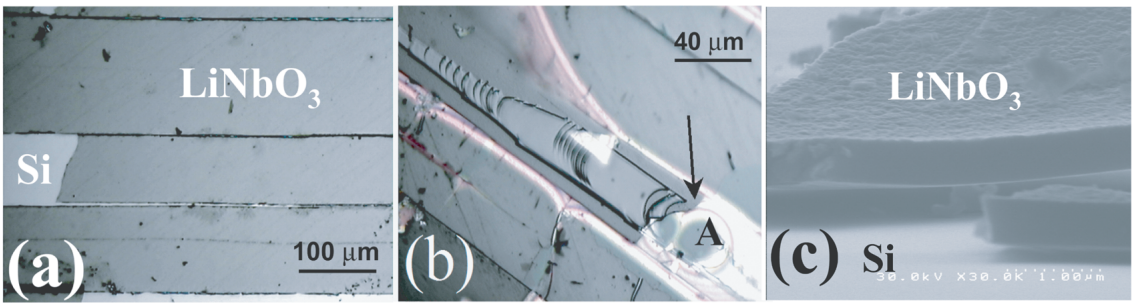

Figure C.2: (a) Plan-view optical microscope image of transferred $LiNbO_3$ layer on Si, (b) bulk $LiNbO_3$ crystal with an short laser duration on the bulk crystal point as marked with A, and (c) layer exfoliate with 500 °C annealing of implanted $LiNbO_3$ crystal. Implanted energy was H^+ dose (80 keV) with 5×10^{16} ions/cm^2 and He^+ dose (115 keV) with 1×10^{17} ions/cm^2, respectively.

planted into the single crystal $LiNbO_3$ wafer (donor) as shown in Figure C.1(a). The peak concentration location of ion species can be controlled by the implant energy. An implant energy of 30 or 80 keV is chosen to achieve an expected H^+ peak concentration of approximately 0.2 or 0.8 μm below the donor wafer top surface. The implanted hydrogen and helium ions introduce micro-cavities along the peak concentration during the post-annealing or laser irradiation. The straggle range of ions is approximately 160 nm for hydrogen, which roughly means a rms roughness of the transferred layer can be approximately 80 nm. After the implantation, donor wafer and receptor substrates are cleaned to remove organic contamination and particles and also to obtained hydrophilic surface and bonded at room temperature (Figure C.1(b)). The continuous wave CO_2 laser was irradiated and scanned from $LiNbO_3$ side, as shown in Figure C.1(c), to transfer layer from thermo-mechanical shock-induced lateral crack and forward layer transfer as in the LLO processes [118–120]. The transferred thickness is consistent with the value we predicted using SRIM (Figure C.1(d)). This means that high dose implantation ($\sim1\times10^{17}$ ions/cm^2) introduces a lot of damage in the peak concentration region and most of laser power was absorbed in the implant damaged region. The transferred $LiNbO_3$ thin films have been characterized by optical microscope, micro-Raman spectroscopy and atomic force microscopy/piezoresponse force microscopy (PFM) and micro-disk structure was fabricated using conventional Si-based CMOS processes.

Figure C.2(a) shows plan-view polarized optical microscope (OM) images of the transferred layer after laser-induced transfer. In the transferred $LiNbO_3$ thin film, one can see

cracks along the same orientation. This kind of crack generation is observed in ion implanted $LiNbO_3$ bulk crystal and also CO_2 laser-irradiated bulk $LiNbO_3$ (Figure C.2(b)) revealed cracks along the domain with a density of 1.3×10^2/cm. It is frequently observed that the intersection between lamellar twin defects act as preferred sites for crack nucleation in bulk $LiNbO_3$ [121, 122]. It could be considered that the polarization vectors are arranged as head-to-tail on the twin boundaries. We speculate that these mechanically cleaved lines are induced by thermal shock-induced rapid heating/quenching processes during the laser irradiation and transfer process [118]. Figure C.2(c) shows the exfoliate result at 500 °C with Si wafer bonding. With lower bond strength after room temperature bonding, transferred thin film was wrinkled and showed discontinuous layer bonding during the subsequent annealing step. In Figure C.2 (c), the thickness of the blister is approximately 800 nm and it is well consistent with Monte Carlo ion trajectory simulation (SRIM-2003) result. Regarding transferred film and morphology, it is believed that the fundamental mechanism of our layer transfer process is the explosive effusion of implanted species at the ion projected range that occurs as the $LiNbO_3$ is thermo-mechanically delaminated from the donor $LiNbO_3$ wafer toward a receptor substrate (Si) during the high power laser irradiation.

Figure C.3 shows AFM and PFM images for the transferred $LiNbO_3$ layers on highly doped Si(100) substrate obtained from the middle of the transferred area (34 μm$\times$34 μm). The rms surface roughness of the $LiNbO_3$ crystal was increased from 2.0 nm to 11.0 nm after high dose implantation. The rms roughness of the transferred $LiNbO_3$ layer is 30.8 nm due to the implantation-induced damage at the top layer. The increase of rms roughness is mainly due to the existence of many cavities on the transferred surface or Li-evaporation at high temperature rapid heating from the laser [110, 111]. In addition, domain wall was observed due to the twin formation from thermal stress during the cooling-down process after layer transfer as seen in Figure C.2(a). In order to use this transferred $LiNbO_3$ layer for optoelectronic device application, surface roughness and crystallographic damage will be a critical issue. Therefore, after layer transfer process, damage removal process is required to reduce damage and surface roughness using chemical mechanical polishing (CMP) process. In the piezoresponse image (Figure C.3(b)), bright and dark areas originate from the downward (positive) and upward (negative) oriented domains, respectively [123]. Strong dark contrast in domain regions suggests the existence of highly polarized area even without pol-

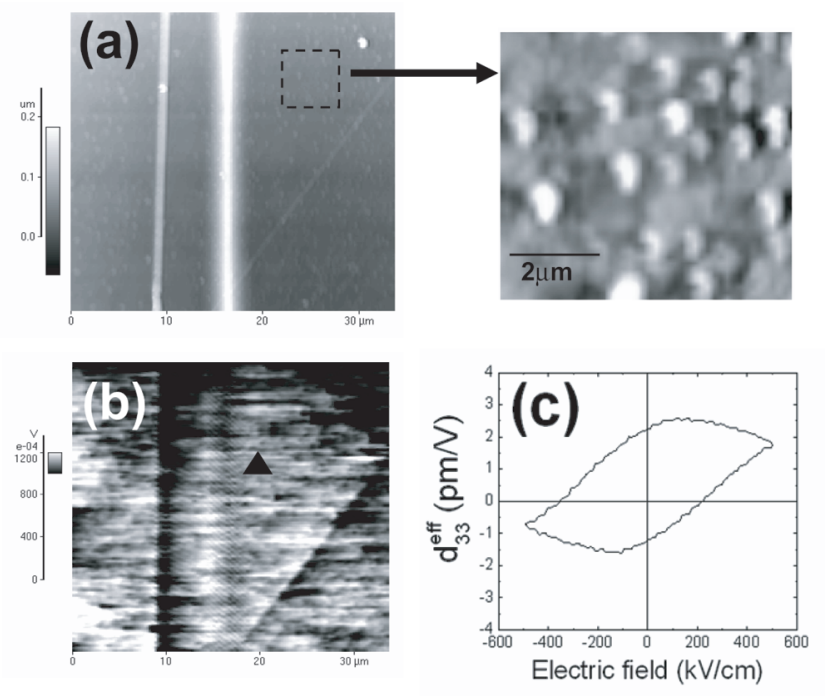

Figure C.3: Simultaneously obtained (a) AFM topographic with small scan area image and (b) piezoresponse (PFM mode) images of the transferred $LiNbO_3$ layer (200 nm) on the Si and (c) piezoresponse-hysteresis (P-E) curve obtained by piezoresponse signal at the point ▲ from domain image in (b). The modulation voltage of the tip, V_{ac}, is 1.3 V and modulation frequency is 18 kHz. PFM and AFM images are scanned by 34 μm $\times$ 34 μm area.

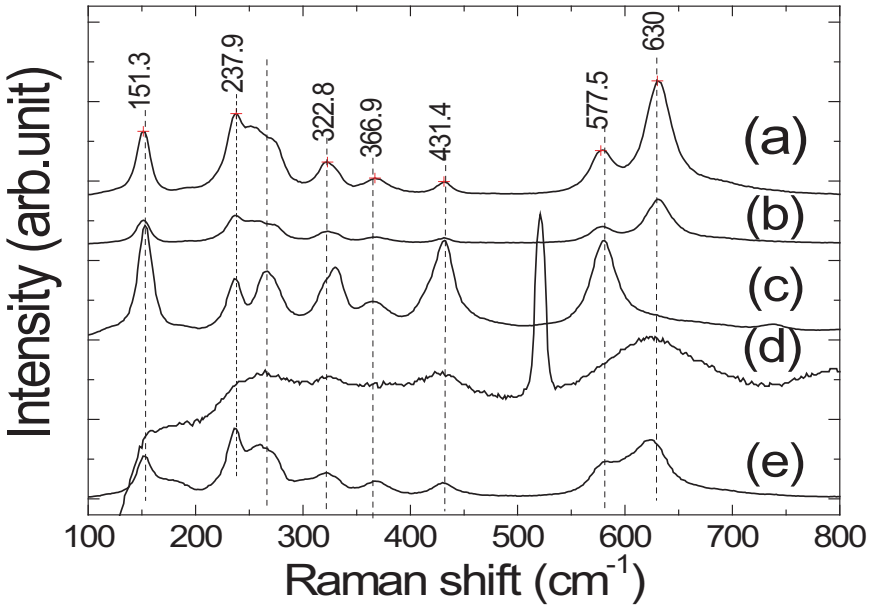

Figure C.4: Micro-Raman spectra for (a) fresh $LiNbO_3$ bulk crystal as a reference, (b) ion implanted $LiNbO_3$. H^+ dose (80 keV) is 5×10^{16} ions/cm^2 and He^+ dose (115 keV) is 1×10^{17} ions/cm^2, (c) after CW-CO_2 laser irradiation of bulk $LiNbO_3$, (d) the transferred $LiNbO_3$ on Si (200 nm) and (e) transferred $LiNbO_3$ on Si (800 nm). Strong peak at 520 cm^{-1} is due to the Si(TO) mode from Si substrate.

ing bias. Figure C.3(c) shows P-E hysteresis curves obtained from the piezoresponse signal (tip amplitude) as a function of DC bias. From the DC-bias applied between conducting AFM tip and substrate, piezoelectric strain coefficient, d_{33}, value ($\Delta Z = d_{33}V_{ac}\sin(\omega t)$, where Z is the longitudinal displacement, V_{ac} is the amplitude of the AC voltage and ω is the angular frequency) was obtained to be 2.0-2.5 pm/V which is smaller than bulk $LiNbO_3$ as reported by 6.0 pm/V. This small d_{33} value is mainly due to the clamping effect of the thick Si substrate in the case of thin film and since the measurement was performed without a domain poling process.

$LiNbO_3$ belongs to the C_{3V} point group (R3c-3m) and has four A_1 and nine E Raman active transitions ($4A_1 + 9E$) [124]. In the unprocessed $LiNbO_3$ (Figure C.4(a)), the bands between 250 and 450 cm^{-1} are related Nb-O octahedral bending modes and the bands from 450 to 800 cm^{-1} are associated with Nb-O octahedral stretching modes. After the H^+/He^+ ions implantation (Figure C.4(b)), the local modes decreased due to the local damage from

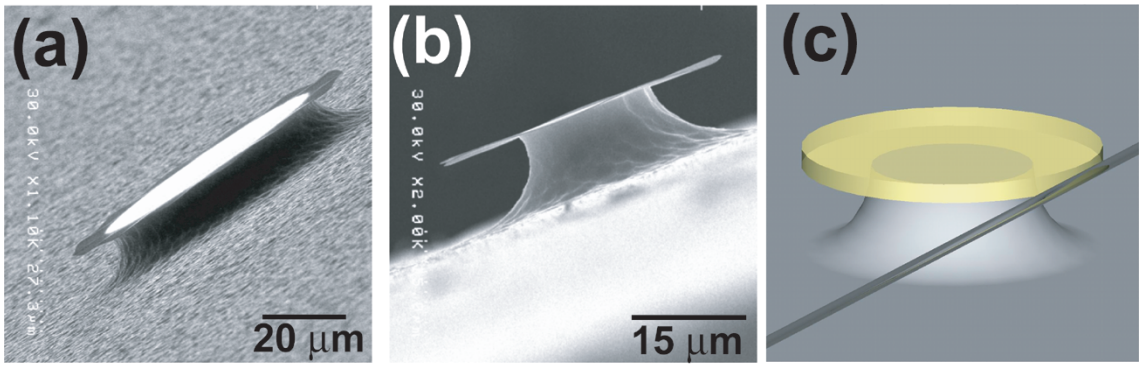

Figure C.5: (a) and (b) SEM images of micro-disk structures using transferred $LiNbO_3$ thin film on Si substrate and (c) schematic diagram of micro-disk in micro-resonator application.

high dose and energy implantation. The most notable local mode intensity change is in the 250-450 cm^{-1} for laser irradiated $LiNbO_3$ samples as shown in Figure C.4(c). This band suggests that the niobium octahedron have been distorted or Li element is partially released from the $LiNbO_3$ structure by laser irradiation. Similar phenomena have been reported in proton exchanged $LiNbO_3$ and high energy He^+ implantation of $LiNbO_3$ [112,125]. However, the transferred-$LiNbO_3$ thin films (Figure C.4(d) and (e)) have the same local mode with the original bulk $LiNbO_3$. These results suggest that the laser-induced thermal energy is primarily confined in the implanted region.

Using the transferred $LiNbO_3$ thin film (800 nm) on Si, we fabricated the micro-disk structure as shown in Figure C.5. The detail fabrication process of the micro-disk is described in [126]. After the isotropic dry etch of the Si substrate under the bonded $LiNbO_3$ using XeF_2, thin $LiNbO_3$ layer shrank a little bit due to the strain relaxation during the dry etching. For communication applications with λ= 1.55 μm resonator, we need to increase the transferred layer thickness in the future. However, considering thicker $LiNbO_3$ single crystal film with several micrometer thick reported by Radojevic et al., it is possible to obtain thicker film using high energy (several MeV range) implantation [112, 113]. The layer transferred $LiNbO_3$ thickness can be increased by enhancing the implant energy but is ultimately limited by the equipment capability and processing time as Izuhara et al. reported for several micron thickness freestanding $LiNbO_3$. However, conventional medium-current implant equipment employed for achieving the required dose range is typically limited to a maximum implant energy of around 400 keV (this energy corresponds to approximately 4.5 μm thick $LiNbO_3$ thin film). Low-current implant equipment can offer

higher implant energy but make the processing time and cost unpractical. Therefore, future goal of our study will be an epitaxial film growth on the transferred single crystal $LiNbO_3$ as a template because most of researchers have found difficulties in growing highly oriented $LiNbO_3$ thin film directly on the Si surface due to huge lattice mismatch and coefficient of thermal expansion (CTE) problem between Si and $LiNbO_3$ [127]. Considering this future application, thickness used in this study is enough for template and also damage removal of the top layer in the transferred thin film has to be performed. In conclusion, a novel fabrication process for the integration of single crystal $LiNbO_3$ thin film on silicon has been investigated with wafer bonding and layer transfer using laser-irradiation in conjunction with ion implantation. High dose and high energy H^+ and He^+ co-implantation is used to synthesize a buried damage layer in the $LiNbO_3$ bulk crystal, which is bonded with the Si at room temperature. After room temperature bonding, high power CO_2 laser-irradiation is used for lateral propagation of gas microcavities at the buried damage layer from rapid absorption of radiation heat, leading to localized layer exfoliation from the $LiNbO_3$ donor substrate. Large area single crystal $LiNbO_3$ thin films (6 mm^2, 200-800 nm thick) have been transferred on the Si(100) substrates and exhibit typical piezoelectric characteristics and suspended micro-disk structure has been successfully fabricated. In this study, we transfer thin $LiNbO_3$ layer onto Si wafer and it acts as masking layer of patterning and template for subsequent thick $LiNbO_3$ growth $\sim$1.3 μm in order to obtain thicker $LiNbO_3$ layer for micro-resonator fabrication. This process will give more feasible mass production-type consideration of ion implantation-induced layer splitting and wafer bonding applications.

Bibliography

[1] A. B. Matsko and V. S. Ilchenko, "Optical resonators with whispering-gallery modes - Part I: Basics," *IEEE Journal of Selected Topics in Quantum Electronics*, vol. 12, no. 1, pp. 3–14, 2006.

[2] D. W. Vernooy, V. S. Ilchenko, H. Mabuchi, E. W. Streed, and H. J. Kimble, "High-Q measurements of fused-silica microspheres in the near infrared," *Optics Letters*, vol. 23, no. 4, pp. 247–249, 1998.

[3] L. Rayleigh, "The problem of the whispering gallery," *Philosophical Magazine*, vol. 20, pp. 1001–1004, 1910.

[4] ——, "Further applications of Bessel's functions of high order to the whispering gallery and allied problems," *Philosophical Magazine*, vol. 27, pp. 100–109, 1914.

[5] G. Mie, "Articles on the optical characteristics of turbid tubes, especially colloidal metal solutions." *Annalen Der Physik*, vol. 25, pp. 377–445, 1908.

[6] P. Debye, "The heliograph of spheres of any material," *Annalen Der Physik*, vol. 30, pp. 57–136, 1909.

[7] R. D. Richtmyer, "Dielectric resonators," *Journal of Applied Physics*, vol. 10, pp. 391–398, 1939.

[8] A. Ashkin and J. M. Dziedzic, "Observation of resonances in radiation pressure on dielectric spheres," *Physical Review Letters*, vol. 38, pp. 1351–1354, 1977.

[9] P. Chylek, J. T. Kiehl, and M. K. W. Ko, "Optical levitation and partial-wave resonances," *Physical Review A*, vol. 18, pp. 2229–2233, 1978.

[10] V. B. Braginsky, M. L. Gorodetsky, and V. S. Ilchenko, "Quality-factor and nonlinear properties of optical whispering-gallery modes," *Physics Letters A*, vol. 137, pp. 393–397, 1989.

[11] A. A. Savchenkov, V. S. Ilchenko, A. B. Matsko, and L. Maleki, "Kilohertz optical resonances in dielectric crystal cavities," *Physical Review A*, vol. 70, p. 051804, 2004.

[12] D. W. Vernooy, A. Furusawa, N. P. Georgiades, V. S. Ilchenko, and H. J. Kimble, "Cavity QED with high-Q whispering gallery modes," *Physical Review A*, vol. 57, pp. R2293–R2296 APR 1998, 1998.

[13] S. M. Spillane, T. J. Kippenberg, K. J. Vahala, K. W. Goh, E. Wilcut, and H. J. Kimble, "Ultrahigh-Q toroidal microresonators for cavity quantum electrodynamics," *Physical Review A*, vol. 71, no. 1, 2005, 013817.

[14] K. J. Vahala, "Optical microcavities," *Nature*, vol. 424, no. 6950, pp. 839–846, 2003.

[15] S. M. Spillane, T. J. Kippenberg, and K. J. Vahala, "Ultralow-threshold Raman laser using a spherical dielectric microcavity," *Nature*, vol. 415, no. 6872, pp. 621–623, 2002.

[16] B. Min, T. J. Kippenberg, and K. J. Vahala, "Compact, fiber-compatible, cascaded Raman laser," *Optics Letters*, vol. 28, no. 17, pp. 1507–1509, 2003.

[17] T. J. Kippenberg, S. M. Spillane, and K. J. Vahala, "Kerr-nonlinearity optical parametric oscillation in an ultrahigh-Q toroid microcavity," *Physical Review Letters*, vol. 93, no. 8, 2004, 083904.

[18] S. Arnold, M. Khoshsima, I. Teraoka, S. Holler, and F. Vollmer, "Shift of whispering-gallery modes in microspheres by protein adsorption," *Optics Letters*, vol. 28, no. 4, pp. 272–274, 2003.

[19] F. Vollmer, D. Braun, A. Libchaber, M. Khoshsima, I. Teraoka, and S. Arnold, "Protein detection by optical shift of a resonant microcavity," *Applied Physics Letters*, vol. 80, pp. 4057–4059, 2002.

[20] V. Sandoghdar, F. Treussart, J. Hare, V. LefevreSeguin, J. M. Raimond, and S. Haroche, "Very low threshold whispering-gallery-mode microsphere laser," *Physical Review A*, vol. 54, no. 3, pp. R1777–R1780, 1996.

[21] M. Cai and K. Vahala, "Highly efficient hybrid fiber taper coupled microsphere laser," *Optics Letters*, vol. 26, no. 12, pp. 884–886, 2001.

[22] M. Cai, O. Painter, K. J. Vahala, and P. C. Sercel, "Fiber-coupled microsphere laser," *Optics Letters*, vol. 25, no. 19, pp. 1430–1432, 2000.

[23] D. K. Armani, T. J. Kippenberg, S. M. Spillane, and K. J. Vahala, "Ultra-high-Q toroid microcavity on a chip," *Nature*, vol. 421, no. 6926, pp. 925–928, 2003.

[24] K. Srinivasan, P. E. Barclay, M. Borselli, and O. Painter, "Optical-fiber-based measurement of an ultrasmall volume high-Q photonic crystal microcavity," *Physical Review B*, vol. 70, p. 081306, 2004.

[25] M. Cai, O. Painter, and K. J. Vahala, "Observation of critical coupling in a fiber taper to a silica-microsphere whispering-gallery mode system," *Physical Review Letters*, vol. 85, no. 1, pp. 74–77, 2000.

[26] S. M. Spillane, T. J. Kippenberg, O. J. Painter, and K. J. Vahala, "Ideality in a fiber-taper-coupled microresonator system for application to cavity quantum electrodynamics," *Physical Review Letters*, vol. 91, no. 4, 2003, 043902.

[27] V. S. Ilchenko and A. B. Matsko, "Optical resonators with whispering-gallery modes - Part II: Applications," *IEEE Journal of Selected Topics in Quantum Electronics*, vol. 12, no. 1, pp. 15–32, 2006.

[28] K. Vahala, Ed., *Optical Microcavities.* Singapore: World Scientific, 2004.

[29] R. K. Chang and A. J. Campillo, Eds., *Optical Processes in Microcavities.* Singapore: World Scientific, 1996.

[30] H. Haus, *Waves and Fields in Optoelectronics.* Englewood Cliffs, N. J.: Prentice-Hall, 1984.

[31] J. A. Stratton, *Electromagnetic Theory.* New York: McGraw-Hill, 1941.

[32] L. A. Weinstein, *Open Resonators and Open Waveguides.* Boulder, Colorado: The Golem Press, 1969.

[33] S. M. Spillane, "Fiber-coupled ultra-high-Q microresonators for nonlinear and quantum optics," Ph.D. dissertation, Caltech, 2004.

[34] B. E. Little, J. P. Laine, and H. A. Haus, "Analytic theory of coupling from tapered fibers and half-blocks into microsphere resonators," *Journal of Lightwave Technology*, vol. 17, no. 4, pp. 704–715, 1999.

[35] A. N. Oraevsky, "Whispering-gallery waves," *Quantum Electronics*, vol. 32, pp. 377–400, 2002.

[36] B. Min, T. J. Kippenberg, L. Yang, K. J. Vahala, J. Kalkman, and A. Polman, "Erbium-implanted high-Q silica toroidal microcavity laser on a silicon chip," *Physical Review A*, vol. 70, no. 3, 2004, 033803.

[37] T. J. Kippenberg, S. M. Spillane, and K. J. Vahala, "Modal coupling in traveling-wave resonators," *Optics Letters*, vol. 27, no. 19, pp. 1669–1671, 2002.

[38] A. Yariv, "Universal relations for coupling of optical power between microresonators and dielectric waveguides," *Electronics Letters*, vol. 36, no. 4, pp. 321–322, 2000.

[39] C. C. Lam, P. T. Leung, and K. Young, "Explicit asymptotic formulas for the positions, widths, and strengths of resonances in mie scattering," *Journal of the Optical Society of America B-optical Physics*, vol. 9, pp. 1585–1592, 1992.

[40] S. Schiller, "Asymptotic-expansion of morphological resonance frequencies in Mie scattering," *Applied Optics*, vol. 32, pp. 2181–2185, 1993.

[41] J. R. Buck and H. J. Kimble, "Optimal sizes of dielectric microspheres for cavity QED with strong coupling," *Physical Review A*, vol. 67, p. 033806, 2003.

[42] M. Kuznetsov and H. A. Haus, "Radiation loss in dielectric waveguide structures by the volume current method," *IEEE Journal of Quantum Electronics*, vol. 19, pp. 1505–1514, 1983.

[43] A. W. Snyder, I. White, and D. J. Mitchell, "Radiation from bent optical-waveguides," *Electronics Letters*, vol. 11, pp. 332–333, 1975.

[44] S. J. Garth, "Modes on a bent optical wave-guide," *IEE Proceedings-J Optoelectronics*, vol. 134, pp. 221–229, 1987.

[45] B. Lamouroux, B. Prade, and J. Y. Vinet, "Field deformation on a bent step index fiber," *Journal of Modern Optics*, vol. 38, pp. 761–775, 1991.

[46] D. R. Rowland and J. D. Love, "Evanescent-wave coupling of whispering-gallery modes of a dielectric cylinder," *IEE Proceedings-J Optoelectronics*, vol. 140, pp. 177–188, 1993.

[47] A. Yariv, *Optical Electronics in Modern Communications*. New York: Oxford University Press, 1997.

[48] I. A. White, "Radiation from bends in optical-waveguides - volume-current method," *IEE Journal on Microwaves Optics and Acoustics*, vol. 3, pp. 186–188, 1979.

[49] P. Alivisatos, "The use of nanocrystals in biological detection," *Nature Biotechnology*, vol. 22, no. 1, pp. 47–52, 2004.

[50] W. U. Huynh, J. J. Dittmer, and A. P. Alivisatos, "Hybrid nanorod-polymer solar cells," *Science*, vol. 295, no. 5564, pp. 2425–2427, 2002.

[51] D. V. Talapin and C. B. Murray, "PbSe nanocrystal solids for n- and p-channel thin film field-effect transistors," *Science*, vol. 310, no. 5745, pp. 86–89, 2005.

[52] N. Tessler, V. Medvedev, M. Kazes, S. H. Kan, and U. Banin, "Efficient near-infrared polymer nanocrystat light-emitting diodes," *Science*, vol. 295, no. 5559, pp. 1506–1508, 2002.

[53] V. L. Colvin, M. C. Schlamp, and A. P. Alivisatos, "Light-emitting-diodes made from cadmium selenide nanocrystals and a semiconducting polymer," *Nature*, vol. 370, no. 6488, pp. 354–357, 1994.

[54] M. Kazes, D. Y. Lewis, Y. Ebenstein, T. Mokari, and U. Banin, "Lasing from semiconductor quantum rods in a cylindrical microcavity," *Advanced Materials*, vol. 14, no. 4, pp. 317–+, 2002.

[55] H. J. Eisler, V. C. Sundar, M. G. Bawendi, M. Walsh, H. I. Smith, and V. Klimov, "Color-selective semiconductor nanocrystal laser," *Applied Physics Letters*, vol. 80, no. 24, pp. 4614–4616, 2002.

[56] A. V. Malko, A. A. Mikhailovsky, M. A. Petruska, J. A. Hollingsworth, H. Htoon, M. G. Bawendi, and V. I. Klimov, "From amplified spontaneous emission to microring lasing using nanocrystal quantum dot solids," *Applied Physics Letters*, vol. 81, no. 7, pp. 1303–1305, 2002.

[57] M. Kazes, D. Y. Lewis, and U. Banin, "Method for preparation of semiconductor quantum-rod lasers in a cylindrical microcavity," *Advanced Functional Materials*, vol. 14, no. 10, pp. 957–962, 2004.

[58] P. T. Snee, Y. H. Chan, D. G. Nocera, and M. G. Bawendi, "Whispering-gallery-mode lasing from a semiconductor nanocrystal/microsphere resonator composite," *Advanced Materials*, vol. 17, no. 9, pp. 1131–+, 2005.

[59] A. L. Efros and M. Rosen, "The electronic structure of semiconductor nanocrystals," *Annual Review of Materials Science*, vol. 30, pp. 475–521, 2000.

[60] M. Asada, Y. Miyamoto, and Y. Suematsu, "Gain and the threshold of 3-dimensional quantum-box lasers," *IEEE Journal of Quantum Electronics*, vol. 22, no. 9, pp. 1915–1921, 1986.

[61] T. Yoshie, O. B. Shchekin, H. Chen, D. G. Deppe, and A. Scherer, "Quantum dot photonic crystal lasers," *Electronics Letters*, vol. 38, no. 17, pp. 967–968, 2002.

[62] S. Strauf, K. Hennessy, M. T. Rakher, A. Badolato, P. M. Petroff, E. L. Hu, and D. Bouwmeester, "Photonic crystal quantum-dot laser with ultra-low threshold," in *2005 Quantum Electronics and Laser Science Conference (QELS)*, 2005.

[63] M. A. Hines and P. Guyot-Sionnest, "Synthesis and characterization of strongly luminescing ZnS-capped CdSe nanocrystals," *Journal of Physical Chemistry*, vol. 100, no. 2, pp. 468–471, 1996.

[64] B. O. Dabbousi, J. RodriguezViejo, F. V. Mikulec, J. R. Heine, H. Mattoussi, R. Ober, K. F. Jensen, and M. G. Bawendi, "(CdSe)ZnS core-shell quantum dots: Synthesis

and characterization of a size series of highly luminescent nanocrystallites," *Journal of Physical Chemistry B*, vol. 101, pp. 9463–9475, 1997.

[65] C. A. Leatherdale, W. K. Woo, F. V. Mikulec, and M. G. Bawendi, "On the absorption cross section of CdSe nanocrystal quantum dots," *Journal of Physical Chemistry B*, vol. 106, no. 31, pp. 7619–7622, 2002.

[66] W. G. J. H. M. van Sark, P. L. T. M. Frederix, D. J. Van den Heuvel, H. C. Gerritsen, A. A. Bol, J. N. J. van Lingen, C. D. Donega, and A. Meijerink, "Photooxidation and photobleaching of single CdSe/ZnS quantum dots probed by room-temperature time-resolved spectroscopy," *Journal of Physical Chemistry B*, vol. 105, pp. 8281–8284, 2001.

[67] W. G. J. H. M. van Sark, P. L. T. M. Frederix, A. A. Bol, H. C. Gerritsen, and A. Meijerink, "Blueing, bleaching, and blinking of single CdSe/ZnS quantum dots," *Chemphyschem*, vol. 3, pp. 871–879, 2002.

[68] M. Kuno, D. P. Fromm, S. T. Johnson, A. Gallagher, and D. J. Nesbitt, "Modeling distributed kinetics in isolated semiconductor quantum dots," *Physical Review B*, vol. 67, p. 125304, 2003.

[69] A. L. Efros and M. Rosen, "Random telegraph signal in the photoluminescence intensity of a single quantum dot," *Physical Review Letters*, vol. 78, no. 6, pp. 1110–1113, 1997.

[70] V. I. Klimov, A. A. Mikhailovsky, S. Xu, A. Malko, J. A. Hollingsworth, C. A. Leatherdale, H. J. Eisler, and M. G. Bawendi, "Optical gain and stimulated emission in nanocrystal quantum dots," *Science*, vol. 290, no. 5490, pp. 314–317, 2000.

[71] M. Shim and P. Guyot-Sionnest, "Intraband hole burning of colloidal quantum dots," *Physical Review B*, vol. 64, no. 24, 2001, 245342.

[72] V. I. Klimov, A. A. Mikhailovsky, D. W. McBranch, C. A. Leatherdale, and M. G. Bawendi, "Quantization of multiparticle auger rates in semiconductor quantum dots," *Science*, vol. 287, no. 5455, pp. 1011–1013, 2000.

[73] K. Sasagawa, K. Kusawake, J. Ohta, and M. Nunoshita, "Nd-doped tellurite glass microsphere laser," *Electronics Letters*, vol. 38, no. 22, pp. 1355–1357, 2002.

[74] W. von Klitzing, E. Jahier, R. Long, F. Lissillour, V. Lefevre-Seguin, J. Hare, J. M. Raimond, and S. Haroche, "Very low threshold lasing in Er^{3+} doped ZBLAN microsphere," *Electronics Letters*, vol. 35, no. 20, pp. 1745–1746, 1999.

[75] L. Yang and K. J. Vahala, "Gain functionalization of silica microresonators," *Optics Letters*, vol. 28, pp. 592–594, 2003.

[76] X. Peng, F. Song, S. B. Jiang, N. Peyghambarian, M. Kuwata-Gonokami, and L. Xu, "Fiber-taper-coupled L-band Er^{3+}-doped tellurite glass microsphere laser," *Applied Physics Letters*, vol. 82, no. 10, pp. 1497–1499, 2003.

[77] F. Lissillour, D. Messager, G. Stephan, and P. Feron, "Whispering-gallery-mode laser at 1.56 μm excited by a fiber taper," *Optics Letters*, vol. 26, no. 14, pp. 1051–1053, 2001.

[78] L. Yang, D. K. Armani, and K. J. Vahala, "Fiber-coupled erbium microlasers on a chip," *Applied Physics Letters*, vol. 83, no. 5, pp. 825–826, 2003.

[79] A. Polman, B. Min, J. Kalkman, T. J. Kippenberg, and K. J. Vahala, "Ultralow-threshold erbium-implanted toroidal microlaser on silicon," *Applied Physics Letters*, vol. 84, no. 7, pp. 1037–1039, 2004.

[80] M. L. Gorodetsky and V. S. Ilchenko, "Optical microsphere resonators: optimal coupling to high-Q whispering-gallery modes," *Journal of the Optical Society of America B-Optical Physics*, vol. 16, no. 1, pp. 147–154, 1999.

[81] M. L. Gorodetsky, A. D. Pryamikov, and V. S. Ilchenko, "Rayleigh scattering in high-Q microspheres," *Journal of the Optical Society of America B-Optical Physics*, vol. 17, no. 6, pp. 1051–1057, 2000.

[82] M. L. Gorodetsky, A. A. Savchenkov, and V. S. Ilchenko, "Ultimate Q of optical microsphere resonators," *Optics Letters*, vol. 21, no. 7, pp. 453–455, 1996.

[83] E. Desurvire, *Erbium-Doped Fiber Amplifiers: Principles and Applications.* New York: Wiley, 1994.

[84] P. C. Becker, N. A. Olsson, and J. R. Simpson, *Erbium-Doped Fiber Amplifiers: Fundamentals and Technology.* San Diego: Academic Press, 1997.

[85] P. F. Wysocki, J. L. Wagener, M. J. Digonnet, and H. J. Shaw, "Evidence and modeling of paired ions and other loss mechanisms in erbium-doped silica fibers," in *SPIE on Fiber Laser Sources and Amplifiers IV*, 1993.

[86] G. Bjork, A. Karlsson, and Y. Yamamoto, "Definition of a laser threshold," *Physical Review A*, vol. 50, pp. 1675–1680, 1994.

[87] C. R. Giles and E. Desurvire, "Modeling erbium-doped fiber amplifiers," *Journal of Lightwave Technology*, vol. 9, no. 2, pp. 271–283, 1991.

[88] Y. Sun, J. L. Zyskind, and A. K. Srivastava, "Average inversion level, modeling, and physics of erbium-doped fiber amplifiers," *IEEE Journal of Selected Topics in Quantum Electronics*, vol. 3, no. 4, pp. 991–1007, 1997.

[89] M. L. Brongersma, E. Snoeks, T. van Dillen, and A. Polman, "Origin of MeV ion irradiation-induced stress changes in SiO_2," *Journal of Applied Physics*, vol. 88, no. 1, pp. 59–64, 2000.

[90] W. J. Miniscalco, "Erbium-doped glasses for fiber amplifiers at 1500-nm," *Journal of Lightwave Technology*, vol. 9, no. 2, pp. 234–250, 1991.

[91] J. C. Knight, G. Cheung, F. Jacques, and T. A. Birks, "Phase-matched excitation of whispering-gallery-mode resonances by a fiber taper," *Optics Letters*, vol. 22, no. 15, pp. 1129–1131, 1997.

[92] V. S. Ilchenko and M. L. Gorodetskii, "Thermal nonlinear effects in optical whispering gallery microresonators," *Laser Phys*, vol. 2, pp. 1004–1009, 1992.

[93] E. M. Dianov and A. M. Prokhorov, "Medium-power CW Raman fiber lasers," *IEEE Journal of Selected Topics in Quantum Electronics*, vol. 6, pp. 1022–1028, 2000.

[94] R. H. Stolen and J. E. Bjorkholm, "Parametric amplification and frequency-conversion in optical fibers," *IEEE Journal of Quantum Electronics*, vol. 18, pp. 1062–1072, 1982.

[95] P. L. Voss and P. Kumar, "Raman-effect induced noise limits on $\chi^{(3)}$ parametric amplifiers and wavelength converters," *Journal of Optics B-Quantum And Semiclassical Optics*, vol. 6, no. 8, pp. S762–S770, 2004, sp. Iss. SI.

[96] B. Min, L. Yang, and K. Vahala, "Controlled transition between parametric and Raman oscillations in ultrahigh-Q silica toroidal microcavities," *Applied Physics Letters*, vol. 87, no. 18, 2005, 181109.

[97] T. J. Kippenberg, S. A. Spillane, B. Min, and K. J. Vahala, "Theoretical and experimental study of stimulated and cascaded raman scattering in ultrahigh-Q optical microcavities," *IEEE Journal of Selected Topics in Quantum Electronics*, vol. 10, no. 5, pp. 1219–1228, 2004.

[98] V. S. Ilchenko, P. S. Volikov, V. L. Velichansky, F. Treussart, V. Lefevre-Seguin, J. M. Raimond, and S. Haroche, "Strain-tunable high-Q optical microsphere resonator," *Optics Communications*, vol. 145, pp. 86–90, 1998.

[99] A. Chiba, H. Fujiwara, J. I. Hotta, S. Takeuchi, and K. Sasaki, "Resonant frequency control of a microspherical cavity by temperature," *Japanese Journal of Applied Physics, Part 1*, vol. 43, pp. 6138–6141, 2004.

[100] T. J. Kippenberg, S. M. Spillane, D. K. Armani, and K. J. Vahala, "Ultralow-threshold microcavity raman laser on a microelectronic chip," *Optics Letters*, vol. 29, no. 11, pp. 1224–1226, 2004.

[101] H. Rokhsari and K. J. Vahala, "Ultralow loss, high Q, four port resonant couplers for quantum optics and photonics," *Physical Review Letters*, vol. 92, p. 253905, 2004.

[102] J. K. S. Poon, J. Scheuer, S. Mookherjea, G. T. Paloczi, Y. Y. Huang, and A. Yariv, "Matrix analysis of microring coupled-resonator optical waveguides," *Optics Express*, vol. 12, pp. 90–103, 2004.

[103] G. M. A. Gad, H. J. Eichler, and A. A. Kaminskii, "Highly efficient 1.3-μ m second-Stokes PbWO4 Raman laser," *Optics Letters*, vol. 28, pp. 426–428, 2003.

[104] S. X. Qian and R. K. Chang, "Multiorder Stokes emission from micrometer-size droplets," *Physical Review Letters*, vol. 56, no. 9, pp. 926–929, 1986.

[105] H. B. Lin and A. J. Campillo, "CW nonlinear optics in droplet microcavities displaying enhanced gain," *Physical Review Letters*, vol. 73, pp. 2440–2443, 1994.

[106] D. Braunstein, A. M. Khazanov, G. A. Koganov, and R. Shuker, "Lowering of threshold conditions for nonlinear effects in a microsphere," *Physical Review A*, vol. 53, pp. 3565–3572, 1996.

[107] A. I. Kingon, J. P. Maria, and S. K. Streiffer, "Alternative dielectrics to silicon dioxide for memory and logic devices," *Nature*, vol. 406, pp. 1032–1038, 2000.

[108] R. S. Weis and T. K. Gaylord, "Lithium-niobate - summary of physical-properties and crystal-structure," *Applied Physics A*, vol. 37, pp. 191–203, 1985.

[109] A. M. Radojevic, R. M. Osgood, M. Levy, A. Kumar, and H. Bakhru, "Zeroth-order half-wave plates of $LiNbO_3$ for integrated optics applications at 1.55 μm," *IEEE Photonics Technology Letters*, vol. 12, pp. 1653–1655, 2000.

[110] M. Bruel, "Silicon-on-insulator material technology," *Electronics Letters*, vol. 31, pp. 1201–1202, 1995.

[111] Q. Y. Tong, K. Gutjahr, S. Hopfe, U. Gosele, and T. H. Lee, "Layer splitting process in hydrogen-implanted Si, Ge, SiC, and diamond substrates," *Applied Physics Letters*, vol. 70, pp. 1390–1392, 1997.

[112] A. M. Radojevic, M. Levy, R. M. Osgood, A. Kumar, H. Bakhru, C. Tian, and C. Evans, "Large etch-selectivity enhancement in the epitaxial liftoff of single-crystal $LiNbO_3$ films," *Applied Physics Letters*, vol. 74, pp. 3197–3199, 1999.

[113] T. Izuhara, R. M. Osgood, M. Levy, M. E. Reeves, Y. G. Wang, A. N. Roy, and H. Bakhru, "Low-loss crystal-ion-sliced single-crystal potassium tantalate films," *Applied Physics Letters*, vol. 80, pp. 1046–1048, 2002.

[114] A. Namba, M. Sugimoto, T. Ogura, Y. Tomita, and K. Eda, "Direct bonding of piezoelectric crystal onto silicon," *Applied Physics Letters*, vol. 67, pp. 3275–3276, 1995.

[115] I. Szafraniak, I. Radu, R. Scholz, M. Alexe, and U. Gosele, "Single-crystalline ferroelectric thin films by ion implantation and direct wafer bonding," *Integrated Ferroelectrics*, vol. 55, pp. 983–990, 2003.

[116] T. Izuhara, I. L. Gheorma, R. M. Osgood, A. N. Roy, H. Bakhru, Y. M. Tesfu, and M. E. Reeves, "Single-crystal barium titanate thin films by ion slicing," *Applied Physics Letters*, vol. 82, pp. 616–618, 2003.

[117] Y. B. Park, J. L. Ruglovsky, and H. A. Atwater, "Microstructure and properties of single crystal $BaTiO_3$ thin films synthesized by ion implantation-induced layer transfer," *Applied Physics Letters*, vol. 85, pp. 455–457, 2004.

[118] L. Tsakalakos and T. Sands, "Epitaxial ferroelectric (Pb, La)(Zr, Ti)O_3 thin films on stainless steel by excimer laser liftoff," *Applied Physics Letters*, vol. 76, pp. 227–229, 2000.

[119] P. R. Tavernier and D. R. Clarke, "Mechanics of laser-assisted debonding of films," *Journal of Applied Physics*, vol. 89, pp. 1527–1536, 2001.

[120] D. Toet, M. O. Thompson, P. M. Smith, and T. W. Sigmon, "Laser-assisted transfer of silicon by explosive hydrogen release," *Applied Physics Letters*, vol. 74, pp. 2170–2172, 1999.

[121] B. M. Park, K. Kitamura, Y. Furukawa, and Y. Y. Ji, "Relation between mechanical twinning and cracking in stoichiometric lithium niobate single crystals," *Journal of the American Ceramic Society*, vol. 80, pp. 2689–2692, 1997.

[122] A. W. Vere, "Mechanical twinning and crack nucleation in lithium niobate," *Journal of Materials Science*, vol. 3, pp. 617–621, 1968.

[123] A. Gruverman, O. Auciello, and H. Tokumoto, "Imaging and control of domain structures in ferroelectric thin films via scanning force microscopy," *Annual Review of Materials Science*, vol. 28, pp. 101–123, 1998.

[124] J. M. Jehng and I. E. Wachs, "Structural chemistry and Raman-spectra of niobium oxides," *Chemistry of Materials*, vol. 3, pp. 100–107, 1991.

[125] G. R. Pazpujalt and D. D. Tuschel, "Depth profiling of proton-exchanged $LiNbO_3$ wave-guides by micro-Raman spectroscopy," *Applied Physics Letters*, vol. 62, pp. 3411–3413, 1993.

[126] D. Armani, B. Min, A. Martin, and K. J. Vahala, "Electrical thermo-optic tuning of ultrahigh-Q microtoroid resonators," *Applied Physics Letters*, vol. 85, no. 22, pp. 5439–5441, 2004.

[127] V. A. Joshkin, P. Moran, D. Saulys, T. T. Kuech, L. McCaughan, and S. R. Oktyabrsky, "Growth of oriented lithium niobate on silicon by alternating gas flow chemical beam epitaxy with metalorganic precursors," *Applied Physics Letters*, vol. 76, pp. 2125–2127, 2000.